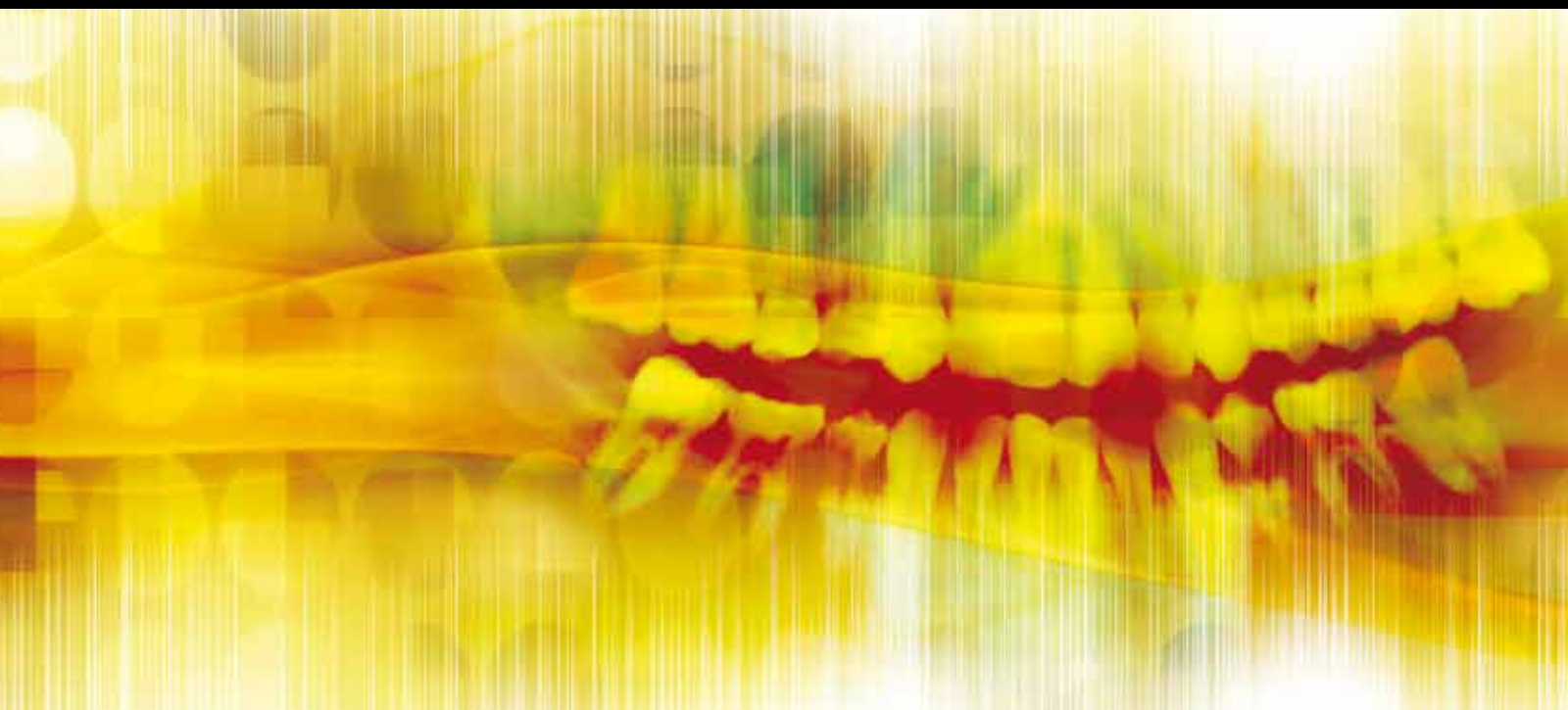


INTERNATIONAL JOURNAL of DENTISTRY

# NANO in IMPLANT DENTISTRY

GUEST EDITORS: RYO JIMBO, MARTIN ANDERSSON, AND STEFAN VANDEWEGHE





---

# **Nano in Implant Dentistry**

International Journal of Dentistry

---

## **Nano in Implant Dentistry**

Guest Editors: Ryo Jimbo, Martin Andersson,  
and Stefan Vandeweghe



---

Copyright © 2014 Hindawi Publishing Corporation. All rights reserved.

This is a special issue published in “International Journal of Dentistry.” All articles are open access articles distributed under the Creative Commons Attribution License, which permits unrestricted use, distribution, and reproduction in any medium, provided the original work is properly cited.



## Editorial Board

Ali I. Abdalla, Egypt  
Yahya Açil, Germany  
Jasim M. Albandar, USA  
M. Awad, United Arab Emirates  
Ashraf F. Ayoub, UK  
Silvana Barros, USA  
Sema Belli, Turkey  
Marilia Buzalaf, Brazil  
Giuseppina Campisi, Italy  
Francesco Carinci, Italy  
Lim K. Cheung, Hong Kong  
Brian W. Darvell, Kuwait  
Hugo De Bruyn, Belgium  
Dong Mei Deng, The Netherlands  
Shinn-Jyh Ding, Taiwan  
J. D. Eick, USA  
Annika Ekestubbe, Sweden  
Carla Evans, USA  
Vincent Everts, The Netherlands  
Stefano Fedele, UK  
G. Nogueira Filho, Canada  
R. Frankenberger, Germany  
Gerald Glickman, USA  
Valeria V. Gordan, USA  
Rosa H. Grande, Brazil

Yoshitaka Hara, Japan  
James K. Hartsfield, USA  
Yumiko Hosoya, Japan  
Saso Ivanovski, Australia  
Chia-Tze Kao, Taiwan  
Elizabeth Kay, UK  
Kristin Klock, Norway  
K.-Y. Kum, Republic of Korea  
Manuel Lagravere, Canada  
Daniel M. Laskin, USA  
Claudio R. Leles, Brazil  
Louis M. Lin, USA  
A. D. Loguercio, Brazil  
T. Lombardi, Switzerland  
Martin Lorenzoni, Austria  
Adriano Loyola, Brazil  
M. Machado, Brazil  
Jukka H. Meurman, Finland  
H. Meyer-Luckel, Germany  
Konstantinos Michalakis, Greece  
Masashi Miyazaki, Japan  
Yasuhiro Morimoto, Japan  
Carlos A. Munoz-Viveros, USA  
Hiroshi Murata, Japan  
Toru Nikaido, Japan

Joseph Nissan, Israel  
Athena Papas, USA  
Patricia Pereira, USA  
Roberta Pileggi, USA  
Michael E. Razzoog, USA  
André Reis, Brazil  
Georgios E. Romanos, USA  
Kamran Safavi, USA  
G. Sammartino, Italy  
Robin Seymour, UK  
Timo Sorsa, Finland  
Gianrico Spagnuolo, Italy  
A. Stavropoulos, Sweden  
Dimitris N. Tatakis, USA  
Shigeru Uno, Japan  
Jacques Vanobbergen, Belgium  
Marcos Vargas, USA  
Ahmad Waseem, UK  
Izzet Yavuz, Turkey  
Cynthia Yiu, Hong Kong  
Li Wu Zheng, Hong Kong  
Qiang Zhu, USA  
Spiros Zinelis, Greece

## Contents

**Nano in Implant Dentistry**, Ryo Jimbo, Martin Andersson, and Stefan Vandeweghe  
Volume 2014, Article ID 314819, 2 pages

**Evaluation of Bone Healing on Sandblasted and Acid Etched Implants Coated with Nanocrystalline Hydroxyapatite: An *In Vivo* Study in Rabbit Femur**, Lory Melin Svanborg, Luiz Meirelles, Victoria Franke Stenport, Per Kjellin, Fredrik Currie, Martin Andersson, and Ann Wennerberg  
Volume 2014, Article ID 197581, 7 pages

**The Effect of Hydroxyapatite Nanocrystals on Osseointegration of Titanium Implants: An *In Vivo* Rabbit Study**, Karin Breiding, Ryo Jimbo, Mariko Hayashi, Ying Xue, Kamal Mustafa, and Martin Andersson  
Volume 2014, Article ID 171305, 9 pages

**Bone-Forming Capabilities of a Newly Developed NanoHA Composite Alloplast Infused with Collagen: A Pilot Study in the Sheep Mandible**, Charles Marin, Ryo Jimbo, Fabio Cesar Lorenzoni, Lukasz Witek, Hellen Teixeira, Estevam Bonfante, Jose Gil, Rodrigo Granato, Nick Tovar, and Paulo G. Coelho  
Volume 2013, Article ID 296391, 7 pages

**Characteristics of 2 Different Commercially Available Implants with or without Nanotopography**, Ali Alenezi, Yoshihito Naito, Martin Andersson, Bruno R. Chrcanovic, Ann Wennerberg, and Ryo Jimbo  
Volume 2013, Article ID 769768, 8 pages

**Silver Nanoparticles and Mitochondrial Interaction**, Eriberto Bressan, Letizia Ferroni, Chiara Gardin, Chiara Rigo, Michele Stocchero, Vincenzo Vindigni, Warren Cairns, and Barbara Zavan  
Volume 2013, Article ID 312747, 8 pages

**Electronic Properties of TiO<sub>2</sub> Nanoparticles Films and the Effect on Apatite-Forming Ability**, Johanna Löberg, Jenny Perez Holmberg, Ingela Mattisson, Anna Arvidsson, and Elisabet Ahlberg  
Volume 2013, Article ID 139615, 14 pages

## Editorial

# Nano in Implant Dentistry

**Ryo Jimbo,<sup>1</sup> Martin Andersson,<sup>2</sup> and Stefan Vandeweghe<sup>3</sup>**

<sup>1</sup> Department of Prosthodontics, Faculty of Odontology, Malmö University, 205 06 Malmö, Sweden

<sup>2</sup> Department of Chemical and Biological Engineering, Applied Surface Chemistry, Chalmers University of Technology, 412 96 Gothenburg, Sweden

<sup>3</sup> Department of Periodontology and Oral Implantology, Dental School, Faculty of Medicine and Health Sciences, University of Ghent, 9000 Ghent, Belgium

Correspondence should be addressed to Ryo Jimbo; [ryo.jimbo@mah.se](mailto:ryo.jimbo@mah.se)

Received 3 November 2013; Accepted 3 November 2013; Published 6 March 2014

Copyright © 2014 Ryo Jimbo et al. This is an open access article distributed under the Creative Commons Attribution License, which permits unrestricted use, distribution, and reproduction in any medium, provided the original work is properly cited.

Nanolevel modification of biomaterials has significantly improved their properties. With regard to implant dentistry, the application of “nano” to implants, abutments, and bone substitutes drastically changed the biologic response to them. Numerous in vitro, in vivo, and clinical studies proved that the submicron modification, normally impossible to detect with our eyes, has enhanced osteogenesis to the biomaterial. An interesting fact is that one of the authors in this special issue L. M. Svanborg has suggested in her thesis work that nanotopography in fact exists on most of the commercially available implant surfaces. However, these structures are most of the time the result of native titanium oxides formed due to the exposure to air; thus, these structures are regarded as nonintended nanomodification.

An important aspect for the application of “nano” to biomaterial surfaces is that the modification is “intended” or “strategically” performed. Cell responses differ depending on the topography and chemistry, and controlling these parameters could target specific biologic phenomena. Thus, studies show that not only the successful enhancement of osseointegration but also the enhancement of soft tissue responses to abutment surfaces.

This special issue is a comprehensive compendium of the state of the art research directed towards implants dentistry. A. Alenezi et al. compared two different commercially available implant surfaces, one with and one without nanostructures. It was suggested that the two different surfaces present distinct bone healing kinetics, and the surfaces possessing nanostructures seemed to be effective in osteoconduction at

early healing periods. J. Löberg et al. have suggested that the nanostructure acts as a nucleation center for the early formation of hydroxyapatites, which supports the in vivo reports. Contradictory to these studies, the in vivo animal study performed by L. M. Svanborg et al. has shown no effects in their histological and biomechanical study. They have speculated that “nano” may not exert significant effects in sites with excellent bone quality. Furthermore, the presence of microtopography, different implant macrogeometry, and coarse evaluation techniques could be one of the causes, which could be disguising the effect of “nano.” K. Breeding et al. have shown in their study that the effect of the nano-level modification could not be detected when removal torque tests were performed; however, gene expression analysis of the removed implants clearly pointed out that osteogenic gene expression had been upregulated for some genes. Based on these studies, the destructive removal torque method may not be suitable to evaluate the effect of nano-level modification and advanced techniques may be necessary for evaluation.

Nano in implant dentistry restricts itself not only to implant surface modifications but also to other biomaterials used in this field. C. Marin et al. have shown that nanostructured synthetic alloplasts fused with collagen promoted bone ingrowth compared to other materials, which could be a promising material to regenerate bone in severe bone defects due to atrophy after tooth/teeth loss. E. Bressan et al. have shown that the antibacterial properties of silver nanoparticles are effective towards targeted pathogens, whereas no cytotoxic effects were observed on human cells. This noble

nanocoating could be an effective method to apply antibacterial properties to biomaterials, such as abutment surfaces to lower the risk of biofilm formation.

We sincerely hope that the readers will find the special issue interesting and informative, which could deepen the knowledge of the current trend in implant dentistry.

*Ryo Jimbo*  
*Martin Andersson*  
*Stefan Vandeweghe*

## Research Article

# Evaluation of Bone Healing on Sandblasted and Acid Etched Implants Coated with Nanocrystalline Hydroxyapatite: An *In Vivo* Study in Rabbit Femur

Lory Melin Svanborg,<sup>1,2</sup> Luiz Meirelles,<sup>2</sup> Victoria Franke Stenport,<sup>3</sup> Per Kjellin,<sup>4</sup> Fredrik Currie,<sup>4</sup> Martin Andersson,<sup>5</sup> and Ann Wennerberg<sup>1,2</sup>

<sup>1</sup> Department of Prosthodontics, Faculty of Odontology, Malmö University, 205 06 Malmö, Sweden

<sup>2</sup> Department of Biomaterials/Handicap Research, Institute of Clinical Sciences, Sahlgrenska Academy, Gothenburg University, 405 30 Göteborg, Sweden

<sup>3</sup> Department of Prosthodontics/Dental Material Science, Institute of Odontology, Sahlgrenska Academy, Gothenburg University, 405 30 Göteborg, Sweden

<sup>4</sup> Promimic AB, 412 92 Göteborg, Sweden

<sup>5</sup> Department of Chemical and Biological Engineering, Applied Surface Chemistry, Chalmers University of Technology, 412 96 Göteborg, Sweden

Correspondence should be addressed to Lory Melin Svanborg; lory.svanborg@mah.se

Received 30 July 2013; Revised 24 September 2013; Accepted 17 October 2013; Published 2 March 2014

Academic Editor: Ryo Jimbo

Copyright © 2014 Lory Melin Svanborg et al. This is an open access article distributed under the Creative Commons Attribution License, which permits unrestricted use, distribution, and reproduction in any medium, provided the original work is properly cited.

This study aimed at investigating if a coating of hydroxyapatite nanocrystals would enhance bone healing over time in trabecular bone. Sandblasted and acid etched titanium implants with and without a submicron thick coat of hydroxyapatite nanocrystals (nano-HA) were implanted in rabbit femur with healing times of 2, 4, and 9 weeks. Removal torque analyses and histological evaluations were performed. The torque analysis did not show any significant differences between the implants at any healing time. The control implant showed a tendency of more newly formed bone after 4 weeks of healing and significantly higher bone area values after 9 weeks of healing. According to the results from this present study, both control and nano-HA surfaces were biocompatible and osteoconductive. A submicron thick coating of hydroxyapatite nanocrystals deposited onto blasted and acid etched screw shaped titanium implants did not enhance bone healing, as compared to blasted and etched control implants when placed in trabecular bone.

## 1. Introduction

Dental implant treatment is today a very reliable method that provides good clinical results with success rates over 90%. Generally, lower implant survival rates have been reported in the maxilla than in the mandible, due to the difference in bone structure [1–4]. However, the optimal implant surface is yet to be developed. The current aim is to develop surfaces resulting in improved success rates in implant sites with poor bone quality and quantity. Several factors have previously been identified to be of particular importance to achieve successful osseointegration. Such factors include the surface

topography, at least on a micrometer level of resolution [5]. A surface with an average surface roughness ( $S_a$ ) of approximately  $1.5\ \mu\text{m}$  has been shown to give a stronger bone response compared to smoother ( $S_a < 1.0\ \mu\text{m}$ ) and rougher surfaces ( $S_a > 2\ \mu\text{m}$ ) [6]. However, research is today often aimed at evaluating the importance of nanometer-sized structures, especially in the early bone healing phase. Several *in vitro* studies have shown an increased cell response to surfaces with applied nanostructures compared to surfaces without such structures [7–15]. During the last few years *in vivo* studies have also shown promising results on bone healing to different nanostructured titanium (Ti) implant

surfaces [16–18]. Further, some human studies have provided evidence of improved bone healing to Ti implants with applied nanostructures [19]. Despite this, the knowledge of the importance of nanostructures in bone healing is still limited and the significance of nanoirregularities in the clinical treatment of patients is currently unknown. According to earlier experimental and clinical studies of implants with micrometer level irregularities, plasma-sprayed hydroxyapatite (HA) coated implants have a stronger initial bone response compared to conventional titanium implants. However, long-term clinical results of the same implants have been poor. This may be explained by the plasma spraying method resulting in coats of a thickness of 50–200  $\mu\text{m}$  and with poor adhesion to the underlying metal [20, 21]. However, it was never investigated whether the initially positive bone response to the plasma-sprayed HA coats was due to an alleged superior biocompatibility of HA, to possible alterations in surface topography, or to a greater press fit of the thicker HA-coated implants when placed in the same sized sites as the controls. To improve the coating and minimize potential problems of coat loosening, thinner HA coats have been developed. A previous study by Svanborg et al. [22] did not support the importance of a nanocrystalline HA coat deposited on sandblasted and acid etched dental implants when placed in cortical bone. Rabbit tibia is suggested to simulate the bone of the human mandible and rabbit femur that of the human maxilla [6]. It may be that nanostructures are of benefit in trabecular bone, which do not provide satisfactory initial stability in contrast to the cortical bone site investigated in our previous study [22]. The use of blasted and acid etched dental implants has shown good clinical results [23] and it would be of interest to investigate if an added coat of nanocrystalline HA further improves the early bone healing in trabecular bone. The aim of this study was to investigate if a submicron thick coating of hydroxyapatite nanocrystals would enhance the bone healing over time, when deposited on sandblasted and acid etched screw shaped implants and placed in trabecular bone.

## 2. Material and Methods

**2.1. Implants.** The implants used in this study were threaded, sandblasted and acid etched titanium screws (grade 4) having a diameter of 3.5 mm and a length of 8.5 mm (custom made). A HA coating was applied on the test implants using a modification of the technique previously described by Kjellin and Andersson, 2006 [24]. This method creates an aqueous dispersion of nanosized HA crystals, sized  $\sim 5$  nm, which are coated with amino acids. The coating of amino acids presents a positive crystal charge, which makes the crystals adhere to negatively charged surfaces, such as a titanium surface. The dispersion was applied onto the implant, and the implant was rotated in a spin-coating apparatus at 3000 rpm. The coated implant was dried in air, and a heat treatment at 550°C for 5 minutes in an oxygen rich atmosphere was done in order to sinter the HA particles onto the titanium surface and to remove the amino acids. With this method, the thickness of the resulting HA layer could be varied depending on the

rotating speed. The rotating speed was set in such a way that the resulting HA layer was less than a micrometer thick, which was estimated using a Leo Ultra 55 FEG high resolution scanning electron microscope (SEM) (Carl Zeiss SMT Inc., North America). Powder X-ray diffraction (XRD) was used to determine the presence of crystalline HA structures. XRD was performed using a Bruker XRD D8 Advance (Bruker AXS, Karlsruhe, Germany) and monochromatic Cu radiation. Sandblasted and acid etched titanium implants were used as control.

**2.2. Implant Surface Analysis.** The implants were examined using SEM, operating at an acceleration voltage of 10 kV (Leo Ultra 55 FEG high resolution SEM, Carl Zeiss SMT Inc.). The magnification used was  $\times 40\,000$  and the micrographs were recorded at randomly chosen areas of the implants. The surface roughness was examined using a white light interferometer (MicroXAM, Phaseshift, Arizona, USA) which is as a highly suitable technique to evaluate threaded implant surfaces [25]. An  $\times 50$  objective and a zoom factor of 0.62 were used in this study. The measured area had a size of  $264 \times 200 \mu\text{m}$  and the vertical measuring range was 100  $\mu\text{m}$ . The maximal resolution of the technique is 0.3  $\mu\text{m}$  horizontally and 0.05 nm vertically. To be able to describe the surface topography, the roughness, the waviness and shape must be taken into consideration. The standard filter used to separate micrometer roughness from waviness, and shape is a high-pass Gaussian filter. A filter size of  $50 \times 50 \mu\text{m}$  has been used for threaded implants. To evaluate the height deviation at the nanometer level a filter size of  $1 \times 1 \mu\text{m}$  was used in this study, as suggested by Svanborg et al. [26]. Surfscan software (Somicronic Instrument, Lyon, France) was used to do the filtration and evaluation. This equipment provides images and numerical descriptions of the surface topography. SPIP (Image Metrology, Denmark) was used to do 3D-illustrations of the surfaces. Three implants from each group were examined. Three valleys on each implant were measured and evaluated.

For numerical description of the surface topography, four parameters were used:

$S_a$  = the arithmetic mean of the roughness area from the mean plane;

$S_{ds}$  = density of summits, that is, number of peaks per area unit;

$S_{dr}$  = the ratio between the developed surface area and a flat reference area;

$S_{ci}$  = core fluid retention index.

The parameters used represent one amplitude ( $S_a$ ), one spatial ( $S_{ds}$ ), one hybrid ( $S_{dr}$ ), and one functional ( $S_{ci}$ ) value. The functional parameter, core fluid retention index ( $S_{ci}$ ), is related to the bone biological ranking based on earlier studies on micrometer level. A low value may be related to a positive biological outcome of bone anchored implants [27]. Mathematical formulas for the parameters can be found in the literature [28].

X-ray photoelectron spectroscopy (XPS) was used for characterisation of the surface chemical compositions. XPS



TABLE 1: Results from the interferometer characterization. The numbers represent the mean value of each parameter (the standard deviation is presented within parenthesis).

	Gauss filter $50 \times 50 \mu\text{m}$				Gauss filter $1 \times 1 \mu\text{m}$			
	$S_a (\mu\text{m})$	$S_{ds} (/mm^2)$	$S_{dr} (\%)$	$S_{ci}$	$S_a (\text{nm})$	$S_{ds} (/mm^2)$	$S_{dr} (\%)$	$S_{ci}$
Control	1.08 (0.41)	1184807 (244569)	142.5 (73.0)	1.21 (0.18)	114 (11.1)	2 055650 (106081)	74.9 (13.4)	0.95 (0.12)
Nano-HA	0.93 (0.25)	1 259841 (143100)	146.5 (46.0)	1.12 (0.25)	119 (6.9)	2 132025 (78489)	83.9 (8.9)	0.84 (0.04)

$S_a$ : the arithmetic mean of the roughness area from the mean plane;  $S_{ds}$ : density of summits, that is, number of peaks per area unit;  $S_{dr}$ : the ratio between the developed surface area and a flat reference area;  $S_{ci}$ : core fluid retention index.

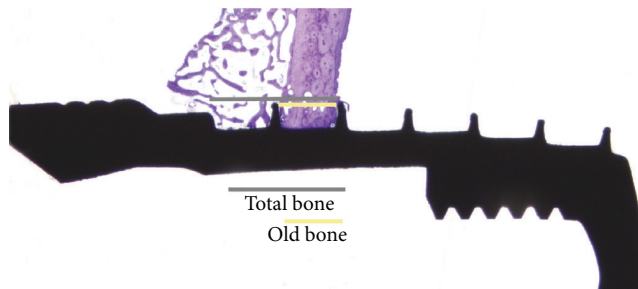


FIGURE 1: Method of measuring total bone and old bone for the new bone calculation. The new bone was calculated from the total amount of bone on each side of the implant on each histological sample minus the amount of old bone; then the percentage was calculated.

survey spectra were obtained using a PHI 5000C ESCA System (Perkin-Elmer Wellesley, USA). An  $\alpha$  excitation source was used at 250 W with an operating angle of  $45^\circ$ .

**2.3. Animals and Surgical Technique.** 27 adult New Zealand rabbits were divided into 3 groups (9 animals in each) with a healing time after implant insertion of 2, 4, and 9 weeks. Before surgery the animals were anaesthetized with an intramuscular injection of fentanyl 0.3 mg/mL and fluanisone 10 mg/mL (Hypnorm Vet, Janssen, Pharmaceutica, Beerse, Belgium) at a dose of 0.5 mL per kg body weight and an intraperitoneal injection of diazepam (Stesolid Novum, Alpharma, Denmark) at a dose of 2.5 mg per animal. One mL of lidocaine (Xylocain, Astra, Sweden) was administered subcutaneously in the surgical site as analgesics and the operation was performed under aseptic conditions. One HA coated implant and one control implant was inserted into the left and right femur, respectively, therefore each animal served as its own control. The implant sites were prepared under irrigation with saline using increasing diameter of drills. Thereafter, the implant was inserted in the bone under saline irrigation. A single dose of prophylactic antibiotic sulfadoxin 200 mg/mL and trimethoprim 40 mg/mL (Borgal, Intervet, Boxtmeer, Netherlands) at a dose of 0.5 mL/kg and 0.5 mL buprenorphine 0.3 mg/mL (Temgesic, Schering-Plough, Belgium) were administrated immediately after the surgery. Right after surgery the rabbits were kept in separate cages to control the wound healing. They had free access to tap water and were fed with pellets and hay. After

initial healing the rabbits were allowed to run freely in a specially designed room. The three groups of animals were sacrificed after 2, 4, and 9 weeks of healing with 10 mL overdose of pentobarbital 60 mg/mL (Pentobarbital-natrium, Apoteksbolaget, Sweden).

**2.4. Removal Torque Analysis.** A removal torque analysis was performed on each implant with an electrically controlled removal torque unit. The implants were subjected only to the necessary torque (Ncm), to interrupt osseointegration, but were then not screwed out from the bone any further. This was done to enable histological evaluations of the bone complex.

**2.5. Specimen Preparation and Histological Evaluation.** After the torque analysis, each implant was removed in a block with the surrounding bone and fixed in 4% neutral buffered formaldehyde. Then the samples were dehydrated in alcohol solutions and embedded in light curing resin (Technovit 7200 VLC, Kultzer & co, Germany). The cutting and grinding was performed as described by Donath [29]. The final sections were approximately  $20 \mu\text{m}$  thick and stained with toluidine-blue. Histological evaluations were performed using a light microscope together with an image analysis software (Image analysis 2000, Sweden). The evaluations included measurements of the amount of new bone (NB) and bone area (BA) along the entire implant. The amount of NB was calculated from the total amount of bone minus the amount of old bone (Figure 1) with a  $\times 4$  objective and a  $\times 10$  lens when needed for visualization. The bone area (BA) was evaluated in each thread on each implant and on the upper threadless part of the implant. The evaluations were made using a  $\times 10$  objective and were presented as the mean value of all threads on the entire implant and as a mean of the three best threads on each side of the implant on histological sample. All measurements were made using a  $\times 10$  eye-pice and in a blinded manner.

**2.6. Statistics.** The statistical analysis was performed using SPSS (statistical package for the social studies). Mann-Whitney  $U$ -test was used and differences were considered significant at  $P \leq 0.05$ .

### 3. Results

Five animals experienced tibia fracture, two in each group with 2 and 9 weeks of healing time, and one in the group

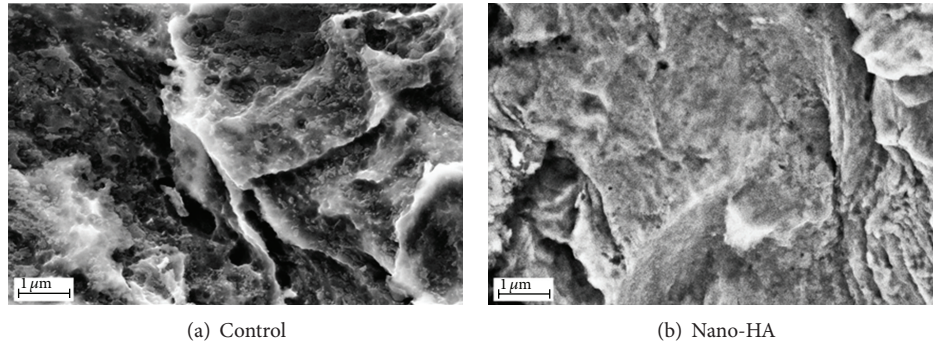


FIGURE 2: SEM images taken at  $\times 40\,000$  magnification on (a) the control surface and (b) the nano-HA surface.

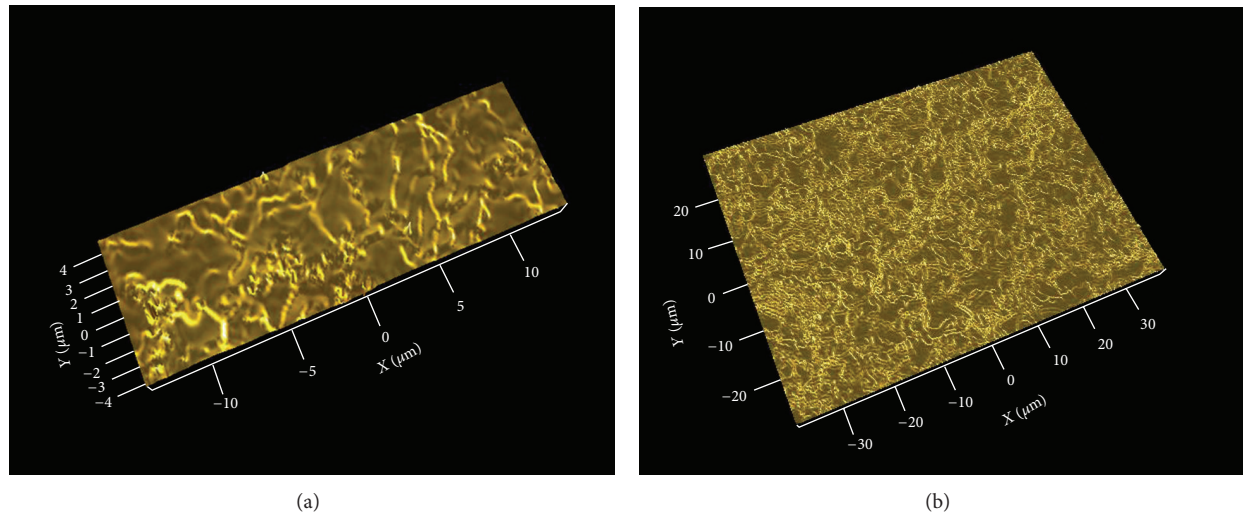


FIGURE 3: Images from the interferometer analysis of (a) the control titanium surface and (b) the test nano-HA surface.

with 4 weeks of healing time. These five rabbits had to be sacrificed in advance and were not included in the results. The postoperative period was uncomplicated for the rest of the rabbits. No signs of infection or inflammation were registered at the time of implant retrieval nor were other deviations from normal observed. All implants were stable at the time of retrieval.

**3.1. Implant Surface Characterization.** SEM images of the surfaces are shown in Figure 2.

Results from the interferometry analysis are presented in Table 1 and images of the surface topography are shown in Figure 3. Both implant types presented similar surface roughness on both micrometer and nanometer level. The mean  $S_a$  value on the micrometer level was  $1.08\,\mu\text{m}$  for the control implant and  $0.93\,\mu\text{m}$  for the nano-HA coated one. There was no significant difference ( $P > 0.05$ ) with respect to the evaluated surface parameters between test and control implants. Further, on the nanometer level, the mean  $S_a$  value was  $114\,\text{nm}$  for the control and  $119\,\text{nm}$  for the nano-HA coated test implants, no significant difference ( $P > 0.05$ ).

The XPS analysis showed presence of calcium and phosphorus on the surface of the coated test implants, while the

controls had no such elements present (Figure 4). Furthermore, the XRD demonstrated the presence of crystalline HA (Figure 5).

**3.2. Removal Torque Analysis.** Results from the torque analysis showed no significant differences between the implant groups at any healing time ( $P > 0.05$ ), see Figure 6. A slightly higher mean value for the nano-HA coated implants could be noted after 2 weeks of healing. No increase in torque value were seen after 4 weeks; however, after 9 weeks of healing the value increased for both implant types, but there were no significant differences between the implants.

**3.3. Histological Results.** Qualitative analysis of all the samples showed a normal inflammatory response in terms of few macrophages and neutrophils observed in the histological samples. After 4 weeks of healing there was a tendency for more new bone on the control implants compared with the coated nano-HA. However, there were no significant differences at any of the chosen healing times (Figure 7).

There was no difference between the implant groups when evaluating the bone area along the entire implant (Figure 8). However, when calculating the 3 best threads



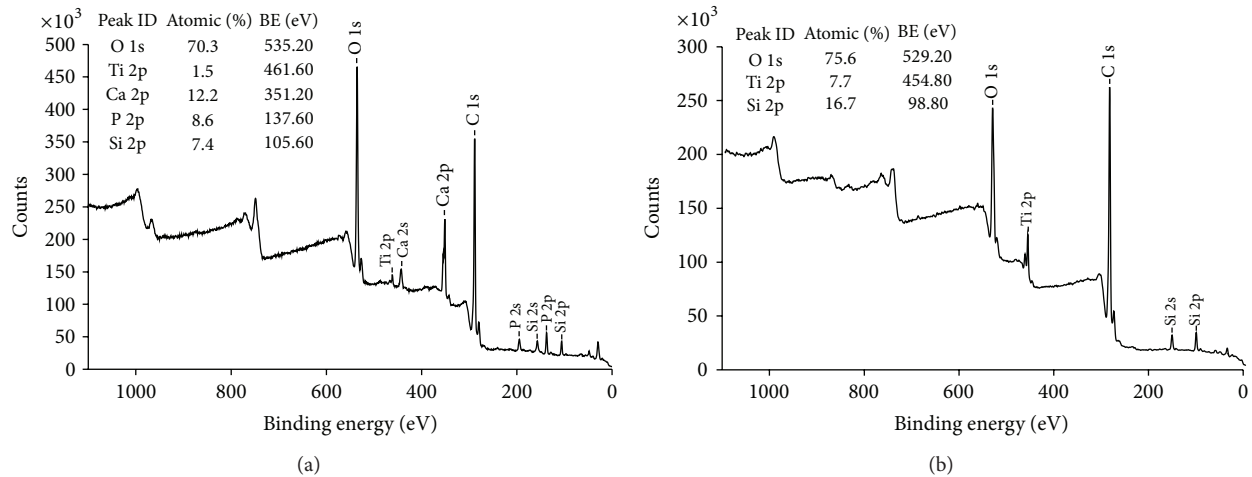


FIGURE 4: XPS survey spectra of (a) the test nano-HA surface and (b) the control titanium surface.

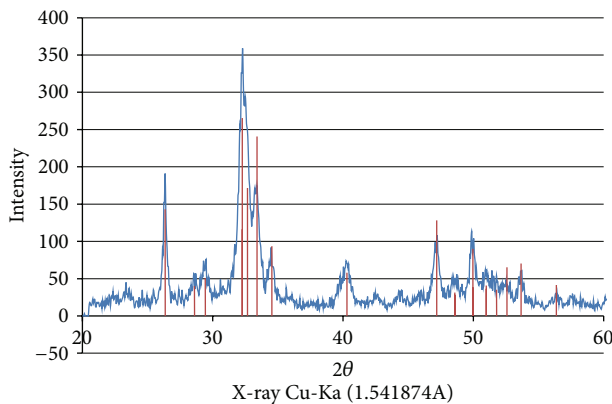


FIGURE 5: XRD demonstrating the presence of crystalline HA.

on each side of the samples, the control implant had a significantly ( $P = 0.025$ ) higher value than the nano-HA after 9 weeks of healing. When evaluating the BA on the upper nonthreaded part of the implants there was also a significantly ( $P = 0.003$ ) higher value for the control implant.

#### 4. Discussion

An error search was made after the experimental part of the study was finished, since 5 rabbits unfortunately suffered from tibia fracture. The animal operations were made according to standard protocol and after well-documented procedures with no complications and by an experienced operator. After a close and strict error analysis, the authors could not find any explanation other than chance for these fractures.

The results from this study showed that both control and nano-Ha surfaces were biocompatible and osteoconductive. However, the submicron thick nano-HA coating did not improve the early bone healing compared to the control and the results support the following studies.

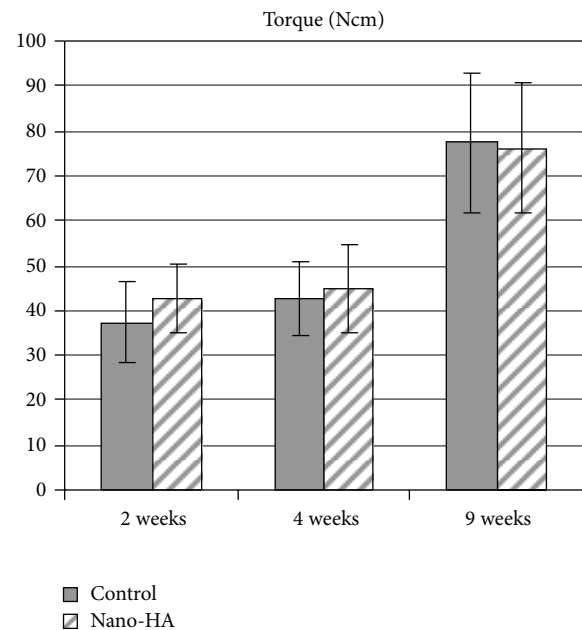


FIGURE 6: Removal torque results (mean value) after 2, 4, and 9 weeks of healing. The bar presents the standard deviation. Seven samples were evaluated in each group.

Coelho et al. (2009) showed that 20–50 nm thick CaP based coating on a blasted and etched cylindrical implants did not improve the biomechanical fixation or BIC after 2 and 4 weeks of healing in dog tibia [30]; an *in vivo* study in goat, on screw shaped grit-blasted, acid etched (GAE) and electrosprayed CaP nanoparticle-coated implants gave similar bone responses and torque values as to GAE alone [31]; Schliephake et al. (2009) did not find any significant difference in host response (foxhound) to dual acid etched (DAE) screw shaped implants coated with HA compared to DAE alone [32]. Further, Lee et al. (2009) concluded that screw shaped titanium or ceramic implants coated with HA

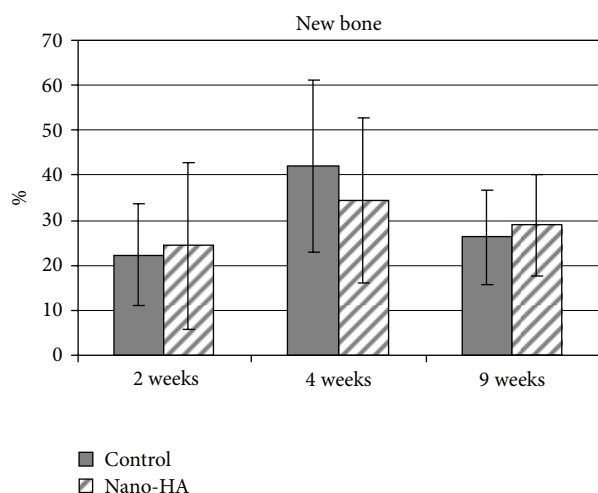


FIGURE 7: Amount of new bone after 2, 4, and 9 weeks of healing. The bar presents the standard deviation. Seven samples were evaluated in each group.

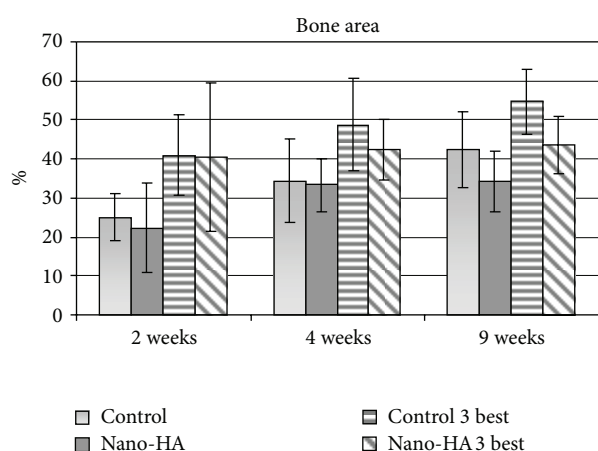


FIGURE 8: Bone area after 2, 4, and 9 weeks of healing. Presented in percentage as a mean of all threads and calculated for the three best threads on each side of each implant. The bar represents the standard deviation.

nanocrystals did not improve the early bone response in rabbit [33]; Svanborg et al. (2011) confirmed similar results [22]. However, there are other *in vivo* studies having shown positive effects on bone healing to various nanostructured Ti implants [16, 18, 19, 34].

As mentioned before, one theory behind this discrepancy in reported results has been that nanostructured Ti implants may be of benefit in bone with poor quality but of insignificant importance in the healing in sites that already provide excellent initial implant stability. However, the present study of implants placed in trabecular bone did not support this theory on trabecular bone influence on implant outcome. Several *in vivo* and some clinical studies have tried to clarify the importance of nanosized structures in early bone healing and osseointegration. Although the studies are performed in different animals, the size, shape, and chemical composition

of the nanostructures are also often different and therefore the studies are very difficult to compare. The difference in results from previous studies might be explained by differences in nanotopography; however the possible effect of the surface chemical composition cannot be excluded. Hence, further studies are needed to be able to conclude if some type of nanostructure may influence the bone healing and also if they might be of significance in the treatment of patients.

## 5. Conclusion

According to the results from this present study, both control and nano-Ha surfaces were biocompatible and osteoconductive. A coating of hydroxyapatite nanocrystals deposited onto blasted and acid etched screw shaped titanium implants did not enhance bone healing after 2, 4, or 9 weeks compared to a blasted and etched control implants.

## Conflict of Interests

The authors declare that there is no conflict of interests regarding the publication of this paper.

## Acknowledgments

This study was supported by Wilhelm and Martina Lundgren Science Foundation, Hjalmar Svensson Foundation, Sigge Perssons & Alice Nybergs Stiftelse (Gothenburg Dental Society), and the Swedish Dental Society, the Swedish Research Council, and Royal Society of Art Sciences in Göteborg. Petra Johansson and Ann Albrektsson are gratefully acknowledged for the preparation of the histological samples.

## References

- [1] P. Astrand, B. Engquist, S. Dahlgren, K. Gröndahl, E. Engquist, and H. Feldmann, "Astra Tech and Brånemark system implants: a 5-year prospective study of marginal bone reactions," *Clinical Oral Implants Research*, vol. 15, no. 4, pp. 413–420, 2004.
- [2] N. J. Attard and G. A. Zarb, "Long-term treatment outcomes in edentulous patients with implant-fixed prostheses: the Toronto study," *International Journal of Prosthodontics*, vol. 17, no. 4, pp. 417–424, 2004.
- [3] T. Jemt, "Single implants in the anterior maxilla after 15 years of follow-up: comparison with central implants in the edentulous maxilla," *International Journal of Prosthodontics*, vol. 21, no. 5, pp. 400–408, 2008.
- [4] U. Lekholm, K. Gröndahl, and T. Jemt, "Outcome of oral implant treatment in partially edentulous jaws followed 20 years in clinical function," *Clinical Implant Dentistry and Related Research*, vol. 8, no. 4, pp. 178–186, 2006.
- [5] T. Albrektsson, P. Brånemark, H. Hansson, and J. Lindström, "Osseointegrated titanium implants. Requirements for ensuring a long-lasting, direct bone-to-implant anchorage in man," *Acta Orthopaedica Scandinavica*, vol. 52, no. 2, pp. 155–170, 1981.
- [6] A. Wennerberg, *On Surface Roughness and Implant Incorporation*, Department of Biomaterials/Handicap Research, University of Gothenburg, Gothenburg, Sweden, 1996.
- [7] P. T. de Oliveira and A. Nanci, "Nanotexturing of titanium-based surfaces upregulates expression of bone sialoprotein and

- osteopontin by cultured osteogenic cells," *Biomaterials*, vol. 25, no. 3, pp. 403–413, 2004.
- [8] P. T. de Oliveira, S. F. Zalzal, M. M. Beloti, A. L. Rosa, and A. Nanci, "Enhancement of in vitro osteogenesis on titanium by chemically produced nanotopography," *Journal of Biomedical Materials Research A*, vol. 80, no. 3, pp. 554–564, 2007.
  - [9] K. L. Elias, R. L. Price, and T. J. Webster, "Enhanced functions of osteoblasts on nanometer diameter carbon fibers," *Biomaterials*, vol. 23, no. 15, pp. 3279–3287, 2002.
  - [10] R. L. Price, M. C. Waid, K. M. Haberstroh, and T. J. Webster, "Selective bone cell adhesion on formulations containing carbon nanofibers," *Biomaterials*, vol. 24, no. 11, pp. 1877–1887, 2003.
  - [11] B. C. Ward and T. J. Webster, "The effect of nanotopography on calcium and phosphorus deposition on metallic materials in vitro," *Biomaterials*, vol. 27, no. 16, pp. 3064–3074, 2006.
  - [12] T. J. Webster and J. U. Ejiófor, "Increased osteoblast adhesion on nanophase metals: Ti, Ti6Al4V, and CoCrMo," *Biomaterials*, vol. 25, no. 19, pp. 4731–4739, 2004.
  - [13] T. J. Webster, C. Ergun, R. H. Doremus, R. W. Siegel, and R. Bizios, "Enhanced functions of osteoblasts on nanophase ceramics," *Biomaterials*, vol. 21, no. 17, pp. 1803–1810, 2000.
  - [14] A. Goransson, A. Arvidsson, F. Currie et al., "An in vitro comparison of possibly bioactive titanium implant surfaces," *Journal of Biomedical Materials Research A*, vol. 88, no. 4, pp. 1037–1047, 2009.
  - [15] M. Sato, A. Aslani, M. A. Sambito, N. M. Kalkhoran, E. B. Slamovich, and T. J. Webster, "Nanocrystalline hydroxyapatite/titania coatings on titanium improves osteoblast adhesion," *Journal of Biomedical Materials Research A*, vol. 84, no. 1, pp. 265–272, 2008.
  - [16] L. M. Bjursten, L. Rasmusson, S. Oh, G. C. Smith, K. S. Brammer, and S. Jin, "Titanium dioxide nanotubes enhance bone bonding in vivo," *Journal of Biomedical Materials Research A*, vol. 92, no. 3, pp. 1218–1224, 2010.
  - [17] L. Meirelles, A. Arvidsson, M. Andersson, P. Kjellin, T. Albrektsson, and A. Wennerberg, "Nano hydroxyapatite structures influence early bone formation," *Journal of Biomedical Materials Research A*, vol. 87, no. 2, pp. 299–307, 2008.
  - [18] V. C. Mendes, R. Moineddin, and J. E. Davies, "The effect of discrete calcium phosphate nanocrystals on bone-bonding to titanium surfaces," *Biomaterials*, vol. 28, no. 32, pp. 4748–4755, 2007.
  - [19] R. J. Goené, T. Testori, and P. Trisi, "Influence of a nanometer-scale surface enhancement on de novo bone formation on titanium implants: a histomorphometric study in human maxillae," *International Journal of Periodontics and Restorative Dentistry*, vol. 27, no. 3, pp. 211–219, 2007.
  - [20] T. Albrektsson, "Hydroxyapatite-coated implants: a case against their use," *Journal of Oral and Maxillofacial Surgery*, vol. 56, no. 11, pp. 1312–1326, 1998.
  - [21] L. Le Guéhennec, A. Soueidan, P. Layrolle, and Y. Amourig, "Surface treatments of titanium dental implants for rapid osseointegration," *Dental Materials*, vol. 23, no. 7, pp. 844–854, 2007.
  - [22] L. M. Svanborg, M. Hoffman, M. Andersson, F. Currie, P. Kjellin, and A. Wennerberg, "The effect of hydroxyapatite nanocrystals on early bone formation surrounding dental implants," *International Journal of Oral and Maxillofacial Surgery*, vol. 40, no. 3, pp. 308–315, 2011.
  - [23] M. M. Bornstein, B. Schmid, U. C. Belser, A. Lussi, and D. Buser, "Early loading of non-submerged titanium implants with a sandblasted and acid-etched surface: 5-year results of a prospective study in partially edentulous patients," *Clinical Oral Implants Research*, vol. 16, no. 6, pp. 631–638, 2005.
  - [24] P. Kjellin and M. Andersson, "Synthetic nano-sized crystalline calcium phosphate and method of production patent," SE-0401524-4, 2006.
  - [25] A. Wennerberg and T. Albrektsson, "Suggested guidelines for the topographic evaluation of implant surfaces," *International Journal of Oral and Maxillofacial Implants*, vol. 15, no. 3, pp. 331–344, 2000.
  - [26] L. M. Svanborg, M. Andersson, and A. Wennerberg, "Surface characterization of commercial oral implants on the nanometer level," *Journal of Biomedical Materials Research B*, vol. 92, no. 2, pp. 462–469, 2010.
  - [27] A. Arvidsson, B. A. Sater, and A. Wennerberg, "The role of functional parameters for topographical characterization of bone-anchored implants," *Clinical Implant Dentistry and Related Research*, vol. 8, no. 2, pp. 70–76, 2006.
  - [28] K. J. Stout, P. J. Sullivan, W. P. Dong et al., *The Development of Methods For Characterisation of Roughness in Three Dimensions*, EUR, 15178 EN of Commission of the European Communities, University of Birmingham, Birmingham, UK, 1993.
  - [29] K. Donath, *Preparation of Histologic Sections by the Cutting-Grinding Technique for Hard Tissue and Other Material Not Suitable to Be Sectioned by Routine Methods*, EXAKT-Kulzer-Publication, Norderstedt, Germany, 1987.
  - [30] P. G. Coelho, G. Cardaropoli, M. Suzuki, and J. E. Lemons, "Early healing of nanothickness bioceramic coatings on dental implants. An experimental study in dogs," *Journal of Biomedical Materials Research B*, vol. 88, no. 2, pp. 387–393, 2009.
  - [31] C. Schouten, G. J. Meijer, J. J. P. van den Beucken et al., "In vivo bone response and mechanical evaluation of electrosprayed CaP nanoparticle coatings using the iliac crest of goats as an implantation model," *Acta Biomaterialia*, vol. 6, no. 6, pp. 2227–2236, 2010.
  - [32] H. Schliephake, A. Aref, D. Scharnweber, S. Rößler, and A. Sewing, "Effect of modifications of dual acid-etched implant surfaces on periimplant bone formation—part II: calcium phosphate coatings," *Clinical Oral Implants Research*, vol. 20, no. 1, pp. 38–44, 2009.
  - [33] J. Lee, J. H. Sieweke, N. A. Rodriguez et al., "Evaluation of nanotechnology-modified zirconia oral implants: a study in rabbits," *Journal of Clinical Periodontology*, vol. 36, no. 7, pp. 610–617, 2009.
  - [34] G. Orsini, M. Piattelli, A. Scarano et al., "Randomized, controlled histologic and histomorphometric evaluation of implants with nanometer-scale calcium phosphate added to the dual acid-etched surface in the human posterior maxilla," *Journal of Periodontology*, vol. 78, no. 2, pp. 209–218, 2007.

## Research Article

# The Effect of Hydroxyapatite Nanocrystals on Osseointegration of Titanium Implants: An *In Vivo* Rabbit Study

Karin Breeding,<sup>1</sup> Ryo Jimbo,<sup>2</sup> Mariko Hayashi,<sup>2</sup> Ying Xue,<sup>3</sup>  
Kamal Mustafa,<sup>3</sup> and Martin Andersson<sup>1</sup>

<sup>1</sup> Department of Chemical and Biological Engineering, Applied Surface Chemistry, Chalmers University of Technology, 41296 Gothenburg, Sweden

<sup>2</sup> Department of Prosthodontics, Faculty of Odontology, Malmö University, 21421 Malmö, Sweden

<sup>3</sup> Department of Clinical Dentistry, Center for Clinical Dental Research, University of Bergen, 5020 Bergen, Norway

Correspondence should be addressed to Martin Andersson; [martina@chalmers.se](mailto:martina@chalmers.se)

Received 28 June 2013; Revised 10 September 2013; Accepted 11 September 2013; Published 19 January 2014

Academic Editor: Stefan Vandeweghe

Copyright © 2014 Karin Breeding et al. This is an open access article distributed under the Creative Commons Attribution License, which permits unrestricted use, distribution, and reproduction in any medium, provided the original work is properly cited.

Osseointegration is dependent on implant surface characteristics, including surface chemistry and topography. The presence of nanosized calcium phosphates on the implant surface is interesting to investigate since they affect both the nanotopography and surface chemistry, forming a bone mineral resembling surface. In this work, the osseointegration of titanium implants with and without the presence of hydroxyapatite (HA) nanocrystals has been evaluated *in vivo*. The integration was examined using removal torque measurements and real-time polymerase chain reaction (RT-PCR) analysis. The study was performed using two healing time points, 3 and 12 weeks. The results showed that the torque needed to remove the implants was insignificant between the non- and HA-coated implants, both at weeks 3 and 12. The RT-PCR, however, showed significant differences for osteoblast, osteoclast, and proinflammation markers when HA nanocrystals were present.

## 1. Introduction

During the last decades, novel implants have been developed with the aim of finding optimal conditions for osseointegration. It is well known that factors, such as surface chemistry and surface topography, influence osseointegration [1]. However, the biological influence of nanorough surfaces is a relatively new area of research and highly interesting since several studies have indicated that nanotopography can enhance osseointegration [2–4]. When combining the two surface entities, nanoroughness and bone-like chemistry, for example, by using nanosized hydroxyapatite (HA), a synergistic effect can be generated [2]. HA is a widely known and frequently used material, which is often being utilized as relatively thick implant coatings. Recently, techniques have been developed which made it possible to coat implants with a monolayer of HA nanoparticles. Such thin HA layers have proven to increase the wettability and thereby increase the surface energy of the implant. Increasing the surface energy is speculated to affect the cell and protein adhesion resulting in

improved osseointegration [5, 6]. Moreover, the adsorption of plasma proteins, such as fibronectin and laminin, has been suggested to increase when implants have been surface-modified with calcium and phosphorous [7].

There are many suggested techniques to determine if osseointegration has occurred [8–13]. Commonly, the removal torque of the implant and histology of the bone-implant interface are examined, both after specific healing times. Most often these two methods are combined, even though not on the same implant, in order to reach a more complete overview of the integration. However, contradictory results have been observed between studies when these two evaluation techniques have been used. HA nanoparticles have been shown to improve the bone-to-implant contact (BIC) when deposited onto electropolished cylindrical-shaped titanium implants [14]. Also, the removal torque has been measured to increase when HA nanoparticles are present on screw-shaped titanium implants [15]. However, Svanborg et al. failed to show any significant differences when HA nano



coated titanium screws were compared to uncoated ones [16]. Discrepancies, such as these, can have many explanations, including differences in implant design, surgical techniques, and evaluation methodology. Recently, novel techniques have emerged and are utilized to evaluate osseointegration, some of which have been suggested to more accurately determine the outcome of nanostructured implants. Studies utilizing gene expression techniques and nanoindentation have shown that the effect of the nanostructured HA coating significantly enhanced the mineralization properties [17, 18]. This was evident even when the histological or biomechanical evaluation approaches did not present significant differences, indicating that the conventional evaluation approaches may be too coarse to investigate the effect of the nanostructure. None of the aforementioned methods is yet the ultimate single method to measure osseointegration, especially when it comes to the influence of nanostructures.

In the present work, we have studied the osseointegration of sand-blasted and acid-etched titanium screw-shaped implants with and without nanosized HA coating. The integration was evaluated using a rabbit study, which was performed at three and twelve weeks. The integration was examined using removal torque measurements and real-time polymerase chain reaction (RT-PCR) analysis.

## 2. Materials and Methods

**2.1. Implant Surface Preparation.** Twenty threaded implants measuring 6 mm in length and 3.3 mm in diameter were produced out of Ti6Al4V. All implants were sand blasted and acid etched according to a procedure used in a previous study [17]. Half of them were coated with nanosized hydroxyapatite (HA), and the other half was left untreated and used as control. 50  $\mu$ L of a HA-particle coating dispersion was poured onto each implant followed by spinning the implant combined with applying a flow of pressurized nitrogen gas, a procedure resulting in a thin layer of particles deposited onto the implant surface. The implants were thereafter heat treated at 450°C for 5 min in an oxygen atmosphere. Four circular discs were also produced and sand blasted and acid etched using the same protocol as for the implants. Two of the discs were also coated with the nanosized HA particles as described above.

**2.2. Scanning Electron Microscopy (SEM).** A scanning electron microscope (LEO Ultra FEG 55, Zeiss, Oberkochen, Germany) was used to investigate the surface morphology of the implants and the circular discs. The analysis was performed at an accelerating voltage of 5 kV using secondary electron detectors. Two implants were randomly selected from each group. Each implant was analyzed at nine positions (thread top, thread valley, and flanks  $\times$  3). The four circular discs were all analyzed at two randomly selected areas.

**2.3. X-Ray Photoelectron Spectroscopy (XPS).** The chemical composition of the outermost surface of the implants was analyzed using XPS (PHI 5500 XPS, PerkinElmer, Waltham, MA, USA). XPS survey spectra were obtained using

a  $\alpha$  excitation source operating at 250 W with an angle of 45°. Two implants were randomly selected from each group. Each implant was analyzed at two positions.

**2.4. Atomic Force Microscopy (AFM).** The surface roughness on the nanometer scale was analyzed using an AFM (INTEGRA Probe NanoLaboratory, NT-MDT, Zelenograd, Russia). Analyses were performed on the circular discs (two noncoated and two HA-coated). Each disc was scanned at three randomly selected areas and was recorded in two different fields of view, that is, 5  $\times$  5  $\mu$ m and 1  $\times$  1  $\mu$ m. The microscope was set to operate in tapping mode and silicon probes (Tap300Al-G, Budget Sensors, resonance freq. 300 kHz) were used. Analysis was performed using the software NOVA 1.0.26 RC1 (INTEGRA Probe NanoLaboratory, NT-MDT, Zelenograd, Russia). Errors of bow and tilt were corrected with a third order subtraction before average height deviation ( $S_a$ ) was calculated.

**2.5. Animals, Implantation, and Sample Preparation.** Twenty adult Swedish lop-eared rabbits (mean weight 4.2 kg) were used. Two implants (one HA-coated and one noncoated used as a reference) were inserted into the proximal part of the left and right tibiae, respectively. Before surgery, the surgical site was shaved and disinfected with 70% ethanol and 70% chlorhexidine. The animals were anesthetized with intramuscular injections of a mixture of 0.15 mL/kg medetomidine (1 mg/mL Dormitor; Orion Pharma, Sollentuna, Sweden) and 0.35 mL/kg ketamine hydrochloride (50 mg/mL Ketlar; Pfizer AB, Sollentuna, Sweden). Lidocaine hydrochloride (Xylocaine; AstraZeneca AB, Södertälje, Sweden) was administered as the local anesthetic at each insertion site at a dose of 1 mL. Osteotomy was prepared with a series of drills and was finalized at a diameter of 2.9 mm, and the implants were thereafter inserted. Postoperatively, buprenorphine hydrochloride (0.5 mL Temgesic; Reckitt Benckiser, Slough, UK) was given as an analgesic for 3 days.

**2.6. Removal Torque.** The rabbits were sacrificed by an anesthetic overdose at weeks 3 and 12 after surgery and the implants and surrounding tissues were removed en bloc. Subsequently, the removal torque needed to unscrew the implant was measured using an electrically controlled removal torque unit [19]. After the removal torque measurements, implants and surrounding bone tissue were placed in RNAlater solution and frozen at -80°C to preserve the mRNA for RT-PCR analysis.

**2.7. RNA Extraction and Real-Time Reverse-Transcription PCR.** RNA extraction from the bone tissue was performed using QiaZol solution (Qiagen GmbH) combined with RNA Tissue Kit SII. To reduce DNA contamination during extraction, all samples were DNase-treated with RNase-free DNase (Qiagen GmbH). RNA quantification was performed using a NanoDrop Spectrophotometer (ThermoScientific NanoDrop Technologies, Wilmington, DE, USA).

The amounts of RNA in the samples were normalized to 50 ng/ $\mu$ L and reverse-transcribed in single 50  $\mu$ L reactions

TABLE 1: The gene expressions that were analyzed.

Gene	Primer sequence	Tm	Amplicon size (bp)	Primer source
ALP	S TGGACCTCGTGGACATCTG A CAGGAGTTCAGTGC GTTC	75	80	<i>Oryctolagus cuniculus</i>
ATPase	S CCTGGCTATTGGCTGTTACG A GCTGGTAGAAGGACACTCTTG	77.7	98	<i>Oryctolagus cuniculus</i>
Calcitonin receptor	S CGTTCACCTCTGAAAAC TACA A GCAACCAAGACTAATGAAACA	72.6	128	<i>Oryctolagus cuniculus</i>
Collagen I	S GGAAACGATGGTGCTACTGG A CCGACAGCTCCAGGGAAG	80.4	83	<i>Oryctolagus cuniculus</i>
IGF-1	S CCGACATGCCCAAGACTCA A TACTTCCTTTCTCTCTCTGA	70.3	81	<i>Oryctolagus cuniculus</i>
IL-6	S GAGGAAAGAGATGTGTGACCAT A AGCATCCGTCTTCTTCTATCAG	73.5	104	<i>Oryctolagus cuniculus</i>
IL-10	S CCGACTGAGGCTTCCATTCC A CAGAGGGTAAGAGGGAGCT	73.3	75	<i>Oryctolagus cuniculus</i>
Osteocalcin	S GCTCAHCCTTCGTGTCCAAG A CCGTCGATCAGTTGGCGC	77.8	70	<i>Oryctolagus cuniculus</i>
Runx2	S GCAGTTCCCAAGCATTTTCATC A GTGTAAGTAAAGGTGGCTGGATA	72.8	81	<i>Oryctolagus cuniculus</i>
TNF- $\alpha$	S CTCACTACTCCCAGGTTCTCT A TTGATGGCAGAGAGGAGGTT	78.2	122	<i>Oryctolagus cuniculus</i>
TRAP	S GCTACCTCCGCTTCCACTA A GCAGCCTGGTCTTGAAGAG	78.5	129	<i>Oryctolagus cuniculus</i>
$\beta$ -Actin	S CACCCTGATGCTCAAGTACC A CGCAGCTCGTTGTAGAAGG	76.4	96	<i>Oryctolagus cuniculus</i>

(25  $\mu$ L RT Mix and 25  $\mu$ L sample). All reverse transcriptions were performed using a high capacity cDNA reverse transcription kit (Applied Biosystems) to generate cDNA for relative quantification on mRNA. The cDNA samples were stored in  $-20^{\circ}\text{C}$  until real-time PCR.

Real-time quantitative reverse-transcription PCR (RT-PCR) was performed in 20  $\mu$ L reaction in triplicate for each sample, with custom-designed primers (Table 1) of SYBR green detection (PrimerDesign Ltd, Southampton, UK). Each PCR reaction contained 1  $\mu$ L Primer, 10  $\mu$ L Master Mix, 4  $\mu$ L water, and 5  $\mu$ L cDNA template and was performed using a 96-well StepOnePlus system (Applied Biosystems, Foster City, CA, USA). StepOne Software v2.3 was used for analysis and the data was normalized by a comparative Ct or  $\Delta\Delta\text{Ct}$  method to get the relative mRNA expression [20, 21]. The control group was set as reference and normalized with the test group in the calculations.  $\beta$ -Actin was used as endogenous control to normalize the input difference of the samples. Both osteogenic markers; ALP, ATPase, Calcitonin receptor, Collagen I, IGF-1, Osteocalcin, Runx2 and TRAP, and Inflammation markers; IL-6, IL-10 and TNF- $\alpha$  were analyzed, Table 1.

**2.8. Statistical Analysis.** The statistical analysis for the removal torque was performed using SAS proc glm and proc mixed (SAS Institute Inc, USA). The analysis was performed

using three-way analysis of variance. The rabbit was regarded as random; time (three and twelve weeks) and treatment (reference and HA-coated) were regarded as fixed factors. The significance level was set at 0.05.

### 3. Results

#### 3.1. Material Characterization

**3.1.1. Scanning Electron Microscopy (SEM).** In Figure 1, SEM images of both noncoated pure titanium and HA-coated titanium screw-shaped implants are shown. At the higher magnification (80 kX) the nanometer-sized HA crystals are clearly seen as elongated particles deposited onto the surface of the HA-coated implants. The particles follow the underlying topography forming an evenly distributed monolayer. In Figures 1(e)–1(h), SEM micrographs of the noncoated and the HA-coated titanium discs are shown. In these images it is seen that the surface morphology of the discs differs somewhat from the surface morphology of the implants. However, the HA crystal layers of the coated discs look similar to the layer onto the coated implants.

**3.1.2. X-Ray Photoelectron Spectroscopy (XPS).** XPS survey spectra for noncoated and HA-coated implants are presented in Figure 2. The XPS-spectrum for the HA-coated implants



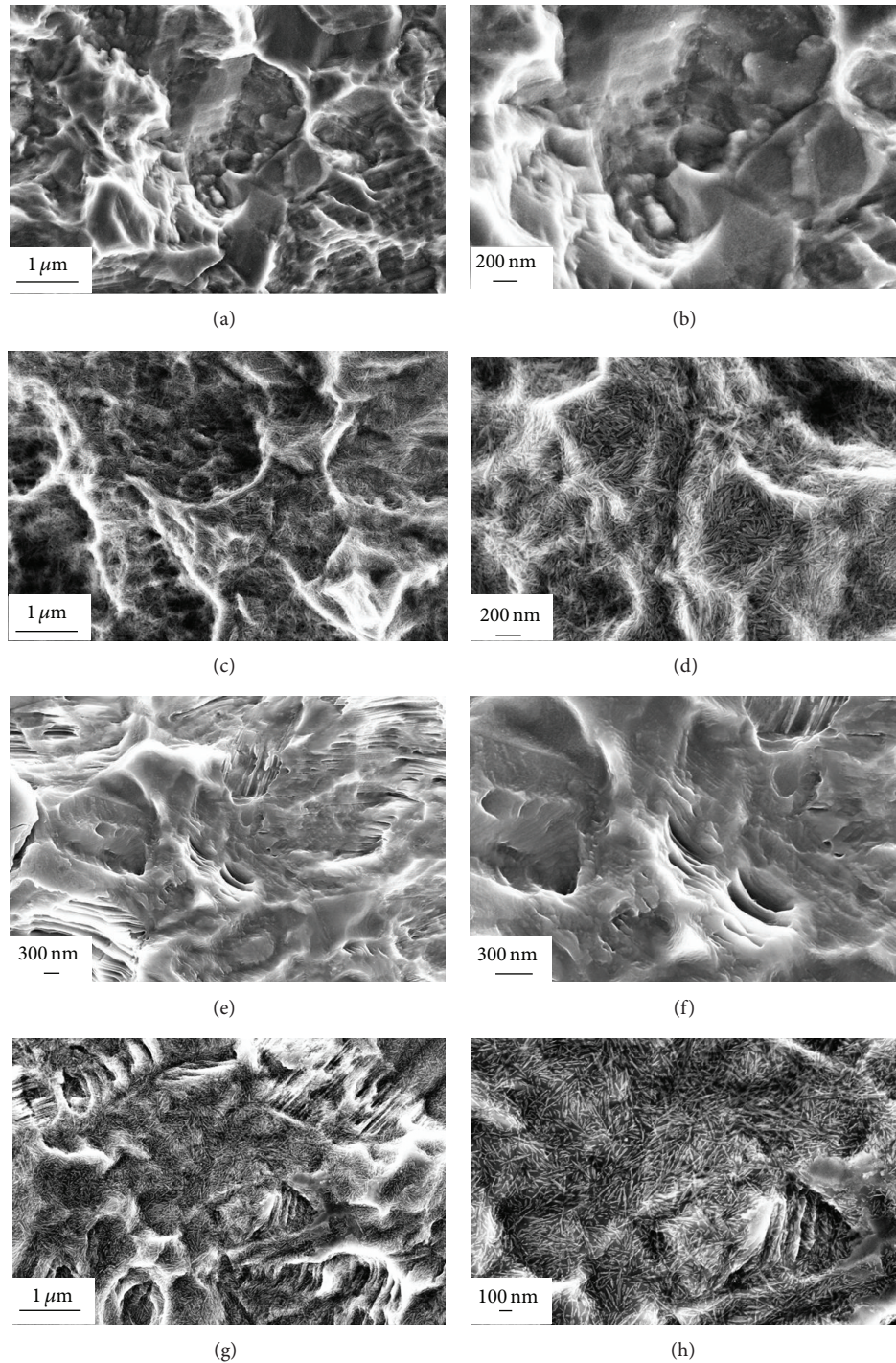


FIGURE 1: SEM micrographs of noncoated implant at magnifications 40 kX and 80 kX ((a)-(b)) and HA-coated implant at mag. 40 kX and 80 kX ((c)-(d)). SEM images of noncoated disc at mag. 40 kX and 80 kX ((e)-(f)) and HA-coated disc at mag. 40 kX and 80 kX ((g)-(h)).

revealed that the surface contained calcium and phosphorous, which were not observed on the noncoated surface. The amount of carbon on the noncoated and the HA-coated implants was similar.

**3.1.3. Atomic Force Microscopy (AFM).** In Figure 3, AFM micrographs obtained in height mode for both the noncoated

and the HA-coated discs are presented. From the topographical images, no visual differences could be seen between the two surface types. The average values from the surface roughness analysis are shown in Table 2. The HA-coated discs showed notably lower  $S_a$  values for both fields of view ( $5 \mu\text{m} \times 5 \mu\text{m}$  and  $1 \mu\text{m} \times 1 \mu\text{m}$ ) compared to the noncoated discs.

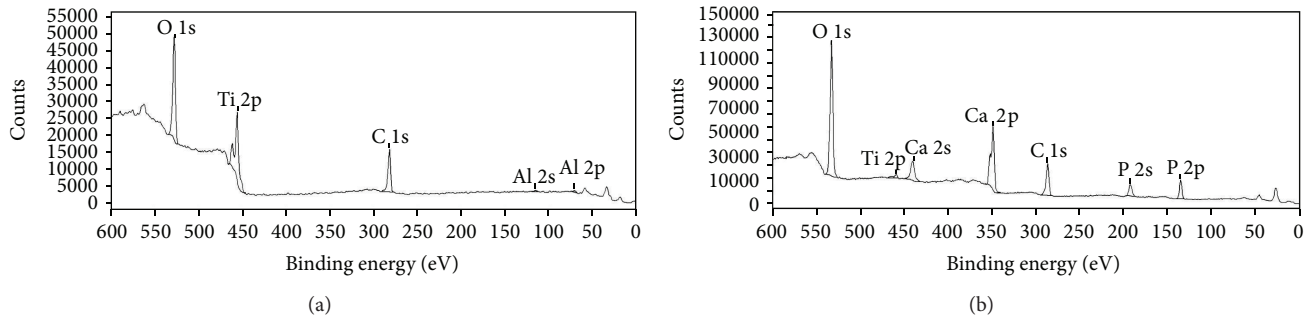


FIGURE 2: XPS-spectra for (a) noncoated implant and (b) HA-coated implant. The binding energy was monitored between 0 and 600 eV.

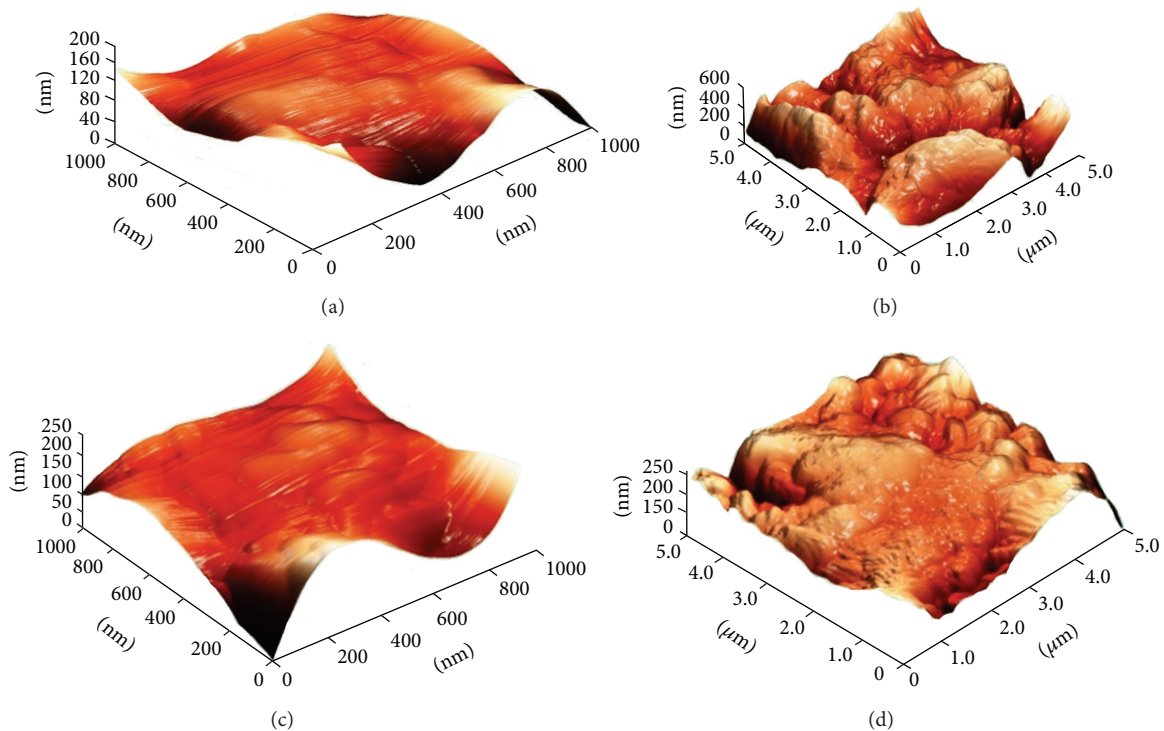


FIGURE 3: 3D AFM images of a noncoated disc ((a) and (b)) and a HA-coated disc ((c) and (d)). Measurements were performed at two different fields of view,  $1\ \mu\text{m} \times 1\ \mu\text{m}$  ((a) and (c)) and  $5\ \mu\text{m} \times 5\ \mu\text{m}$  ((b) and (d)).

TABLE 2: Average  $S_a \pm \text{SD}$  values for HA coated and noncoated discs.

	HA coated	Noncoated
Average $S_a$ , $1 \times 1\ \mu\text{m}$	$4.9 \pm 2.0\ \text{nm}$	$12.9 \pm 5.6\ \text{nm}$
Average $S_a$ , $5 \times 5\ \mu\text{m}$	$41.3 \pm 11.8\ \text{nm}$	$70.3 \pm 13.3\ \text{nm}$
Number	6	7

### 3.2. In Vivo

**3.2.1. Removal Torque.** The results from the removal torque tests after 3 and 12 weeks of healing are presented in Table 3. The 12-week removal torque measurements were performed on 9 animals; due to that one rabbit died during insertion surgery. Statistical analysis showed that no significant

difference could be detected for both weeks 3 and 12 ( $P = 0.19$ , resp.,  $0.06$ ). Comparison between the two healing times was performed using three-way analysis of variance. The animals were regarded as random and time (week three/week twelve) and treatment (noncoated/HA-coated) were regarded as fixed factors. Analysis by SAS proc glm and proc mixed. The three-way analysis showed no significant differences between the noncoated and the HA-coated implants ( $P = 0.28$ ,  $\text{DF} = 17$ ,  $t\text{-value} = -1.12$ ,  $\alpha 0.05$ ).

**3.2.2. Real-Time Polymerase Chain Reaction (RT-PCR).** Results from the osteoblast, osteoclast, and proinflammation markers in the RT-PCR analysis are presented in Figures 4(a)–4(f). At three weeks of healing, gene expression



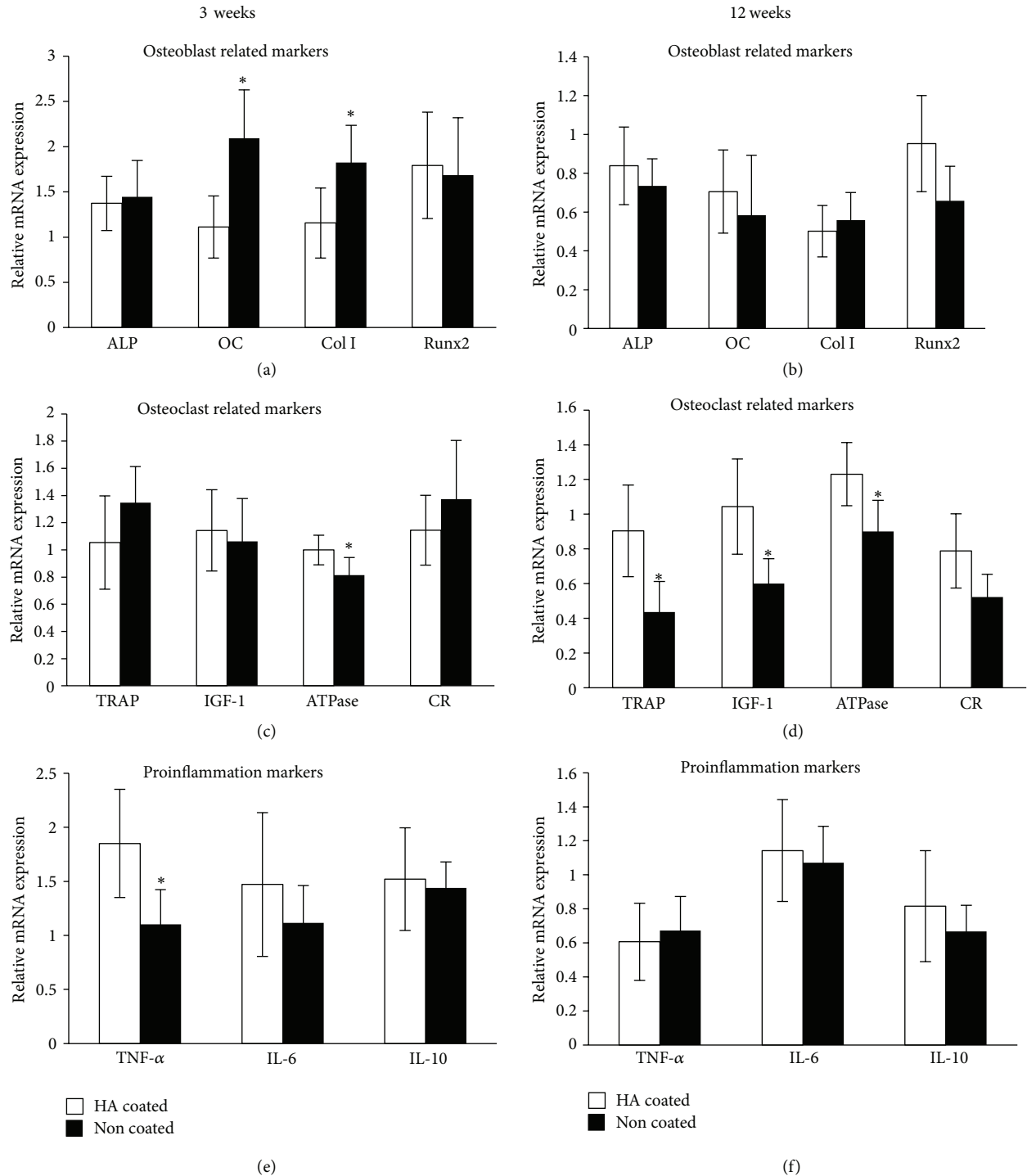


FIGURE 4: Results from RT-PCR analysis of selected genes (ALP, osteocalcin, Collagen I, Runx2, TRAP, IGF-1, ATPase, Calcitonin receptor, TNF- $\alpha$ , IL-6, and IL-10) after three weeks and twelve weeks, respectively. The genes were normalized with the housekeeping gene  $\beta$ -actin, \* $P < 0.05$ . Please note that the genes cannot be compared to each other, only between experimental groups, since the genes are normalized to actin.

of osteocalcin and Collagen I was significantly higher for the HA-coated implants compared to the noncoated implants ( $P = 0.046$ , resp.,  $P = 0.042$ ), whereas the gene expression for ATPase and TNF- $\alpha$  was significantly lower for the HA-coated implant compared to the noncoated implants ( $P = 0.008$ ,

resp.,  $P = 0.0231$ ). At 12 weeks of healing the gene expression of TRAP, IGF-1, and ATPase was significantly lower ( $P = 0.01$ ;  $P = 0.02$ , resp.,  $P = 0.007$ ) for the HA-coated implants compared to the noncoated implants. For the other markers no significant differences were detected.

TABLE 3: Mean removal torque values and statistical comparisons.

	Number	Mean (SD)-Ncm	Median (min; max)
Three weeks			
Noncoated	10	32.4 (8.1)	33.5 (16; 42)
HA coated	10	27.8 (9.1)	30.5 (10; 39)
Twelve weeks			
Noncoated	9	49.3 (11.1)	54 (32; 62)
HA coated	9	38.2 (13.4)	40 (21; 61)
Distribution of the removal torque differences between three weeks and twelve weeks.			
Rabbit	Difference (noncoated-HA coated)	Rabbit	Difference (noncoated-HA coated)
1	19	11	1
2	8	12	-3
3	7	13	2
4	13	14	-7
5	-15	15	30
6	3	16	8
7	-4	17	22
8	3	18	11
9	-3	19	—
10	15	20	36

#### 4. Discussion

In this study, we evaluated the osseointegration properties of titanium implants coated with HA nanoparticles and compared them with noncoated counterparts. The implant surfaces were characterized and it was shown that both nanotopography and surface chemistry were different between the two investigated implants. For the HA-coated implants, SEM showed that elongated particles were present on the surfaces, which most likely are HA crystals. In order to evaluate the nanotopography of the surfaces using AFM, titanium discs were prepared using the same procedure as for the implant screws. SEM revealed, however, that the surface morphology of the discs differed from the implants. Despite these differences, the HA particles seemed to be deposited in a similar fashion on the discs as on the implants. As a consequence, the differences in measured topography on the discs, which is attributed to the HA nanoparticles, are believed to be directly comparable to the ones on the implants. From the AFM results, it was observed that the surface roughness was lower when HA particles were applied onto the surface, which indicates that the particles smoothened out smaller surface features.

The removal torque was measured after 3 and 12 weeks of healing in the rabbit tibia. Statistical calculations showed no significance between the two surfaces at neither of the two time periods. Not even when all HA-coated implants were compared to the noncoated ones could significance be detected. In a previous study, which was performed using the same types of implants, it was shown that the removal torque was significantly higher for the HA-coated surface compared to a noncoated surface only after 2 weeks of healing. In the same study, no significant difference was observed after 4 weeks of healing [18]. This is an indication that the effect of the nano-HA is especially significant at

earlier healing periods and biomechanically the values seem to present no differences after bone maturation. This has been a general tendency with nanosized HA deposited onto titanium surfaces [2, 16, 20, 21]. Furthermore, removal torque is indeed a coarse evaluation technique, since the values may be influenced by different factors, such as macrogeometry or microtopography. It has been suggested that in order to detect the differences generated by nanotopography, other biological evaluation techniques, such as the modified pull out testing, may be suitable [22–24]. However, the use of a screw type model in animal studies is of great value, since this may provide valuable information for the actual clinical implant performance. Thus, in order to detect the detailed differences generated at the nanolevel, different evaluation techniques have been utilized and have provided some interesting results. For example, nanomechanical testing to evaluate the bone nanomechanical properties has shown that indeed there are differences even when no differences were detected with the conventional methods [17]. Furthermore, other state of the art techniques such as the use of micro-CT have provided the possibility to further investigate the unique bone-forming properties to both micro- and nanotopography [25–27]. Sarve et al. have further explored the possibility of obtaining improved boneimplant interfacial images with the use of  $\mu$ CT and have shown that the technique can evaluate the bone-healing properties to surfaces possessing nanotopography [28].

Another detailed evaluation that can possibly explore the genetic mechanisms of the responses to the nanostructured surface is the gene expression. After 3 weeks, significantly higher expressions of osteoblast marking genes, osteocalcin, and Collagen I were detected in the tissue surrounding the HA-coated implants. This indicates a higher osteoprogenitor activity for the modified surface [29]. This increase in the expression of osteogenic genes was not observed after

12 weeks. Interestingly, the osteoclast related marker, TNF- $\alpha$ , was significantly downregulated in the surrounding tissue of the HA-coated implants after 3 weeks. Reportedly, TNF- $\alpha$  contributes to bone loss by inhibiting the IGF-I and ALP genes [30, 31]. The expression of the transmembrane ATPase was lowered around the surrounding tissue of both the 3- and 12-week HA-coated implants. It has been known that a lowered number of ATPase could affect the cell metabolism [32], and this may have influenced the bone turnover rate of the nanostructured surface. At 12 weeks both the TRAP and the IGF-I were significantly lowered for the tissue surrounding the HA implants. Within the limitation of the current study, it is difficult to fully interpret the obtained results since the RT-PCR is still a phenomenological investigation where the researcher selects the gene of interest; however, it is evident that the differences in surface nanotopography and chemistry obviously influenced the gene expression, which was not detectable by the removal torque. In order to further investigate the detailed genetic mechanism, methodologies to detect the signaling pathway may be useful.

## 5. Conclusions

In this work, the osseointegration of screw-shaped titanium implants coated with hydroxyapatite (HA) nanocrystals was evaluated *in vivo*. The results demonstrated that the torque needed to remove the implants was insignificant between pure titanium and HA-coated implants, both at weeks 3 and 12 of healing. RT-PCR performed on osteoblast, osteoclast, and proinflammation markers, however, showed significant differences when HA nanocrystals were present. The results show that nanosized HA crystals deposited onto implants do have a biological effect; however, it is not always detectable using removal torque measurements.

## Conflict of Interests

The authors declare that there is no conflict of interests regarding the publication of this paper.

## References

- [1] A. Wennerberg and T. Albrektsson, "On implant surfaces: a review of current knowledge and opinions," *The International Journal of Oral and Maxillofacial Implants*, vol. 25, no. 1, pp. 63–74, 2010.
- [2] R. Jimbo, J. Sotres, C. Johansson, K. Breiding, F. Currie, and A. Wennerberg, "The biological response to three different nanostructures applied on smooth implant surfaces," *Clinical Oral Implants Research*, vol. 23, no. 6, pp. 706–712, 2012.
- [3] A. Göransson, A. Arvidsson, F. Currie et al., "An in vitro comparison of possibly bioactive titanium implant surfaces," *Journal of Biomedical Materials Research A*, vol. 88, no. 4, pp. 1037–1047, 2009.
- [4] T. J. Webster and E. S. Ahn, "Nanostructured biomaterials for tissue engineering bone," *Advances in Biochemical Engineering/Biotechnology*, vol. 103, pp. 275–308, 2006.
- [5] R. Jimbo, T. Sawase, Y. Shibata et al., "Enhanced osseointegration by the chemotactic activity of plasma fibronectin for cellular fibronectin positive cells," *Biomaterials*, vol. 28, no. 24, pp. 3469–3477, 2007.
- [6] T. Sawase, R. Jimbo, K. Baba, Y. Shibata, T. Ikeda, and M. Atsuta, "Photo-induced hydrophilicity enhances initial cell behavior and early bone apposition," *Clinical Oral Implants Research*, vol. 19, no. 5, pp. 491–496, 2008.
- [7] J. E. Dennis, S. E. Haynesworth, R. G. Young, and A. I. Caplan, "Osteogenesis in marrow-derived mesenchymal cell porous ceramic composites transplanted subcutaneously: effect of fibronectin and laminin on cell retention and rate of osteogenic expression," *Cell Transplantation*, vol. 1, no. 1, pp. 23–32, 1992.
- [8] W. Wang, S. Itoh, Y. Tanaka, A. Nagai, and K. Yamashita, "Comparison of enhancement of bone ingrowth into hydroxyapatite ceramics with highly and poorly interconnected pores by electrical polarization," *Acta Biomaterialia*, vol. 5, no. 8, pp. 3132–3140, 2009.
- [9] P. G. Coelho, R. Granato, C. Marin et al., "Effect of Si addition on Ca- and P-impregnated implant surfaces with nanometer-scale roughness: an experimental study in dogs," *Clinical Oral Implants Research*, vol. 23, no. 3, pp. 373–378, 2012.
- [10] R. Jimbo, M. Ivarsson, A. Koskela, Y. T. Sul, and C. B. Johansson, "Protein adsorption to surface chemistry and crystal structure modification of titanium surfaces," *Journal of Oral and Maxillofacial Research*, vol. 1, no. 3, article e3, 2010.
- [11] B. S. Kang, Y. T. Sul, C. B. Johansson, S. Oh, H. Lee, and T. Albrektsson, "The effect of calcium ion concentration on the bone response to oxidized titanium implants," *Clinical Oral Implants Research*, vol. 23, no. 6, pp. 690–697, 2012.
- [12] A. Arvidsson, F. Currie, P. Kjellin, Y. Sul, and V. Stenport, "Nucleation and growth of calcium phosphates in the presence of fibrinogen on titanium implants with four potentially bioactive surface preparations. An in vitro study," *Journal of Materials Science: Materials in Medicine*, vol. 20, no. 9, pp. 1869–1879, 2009.
- [13] Y. Ramaswamy, C. Wu, H. Zhou, and H. Zreiqat, "Biological response of human bone cells to zinc-modified Ca–Si-based ceramics," *Acta Biomaterialia*, vol. 4, no. 5, pp. 1487–1497, 2008.
- [14] L. Meirelles, A. Arvidsson, M. Andersson, P. Kjellin, T. Albrektsson, and A. Wennerberg, "Nano hydroxyapatite structures influence early bone formation," *Journal of Biomedical Materials Research A*, vol. 87, no. 2, pp. 299–307, 2008.
- [15] L. Meirelles, F. Currie, M. Jacobsson, T. Albrektsson, and A. Wennerberg, "The effect of chemical and nanotopographical modifications on the early stages of osseointegration," *International Journal of Oral and Maxillofacial Implants*, vol. 23, no. 4, pp. 641–647, 2008.
- [16] L. M. Svanborg, M. Hoffman, M. Andersson, F. Currie, P. Kjellin, and A. Wennerberg, "The effect of hydroxyapatite nanocrystals on early bone formation surrounding dental implants," *International Journal of Oral and Maxillofacial Surgery*, vol. 40, no. 3, pp. 308–315, 2011.
- [17] R. Jimbo, P. G. Coelho, M. Bryington et al., "Nano hydroxyapatite-coated implants improve bone nanomechanical properties," *Journal of Dental Research*, vol. 91, no. 12, pp. 1172–1177, 2012.
- [18] R. Jimbo, Y. Xue, M. Hayashi et al., "Genetic responses to nanostructured calcium-phosphate-coated implants," *Journal of Dental Research*, vol. 90, no. 12, pp. 1422–1427, 2011.
- [19] C. B. Johansson, R. Jimbo, and P. Stefenson, "Ex vivo and in vivo biomechanical test of implant attachment to various materials: introduction of a new user-friendly removal torque equipment,"

- Clinical Implant Dentistry and Related Research*, vol. 14, no. 4, pp. 603–611, 2012.
- [20] T. D. Schmittgen and K. J. Livak, “Analyzing real-time PCR data by the comparative CT method,” *Nature Protocols*, vol. 3, no. 6, pp. 1101–1108, 2008.
- [21] R. Jimbo, P. G. Coelho, S. Vandeweghe et al., “Histological and three-dimensional evaluation of osseointegration to nanostructured calcium phosphate-coated implants,” *Acta Biomaterialia*, vol. 7, no. 12, pp. 4229–4234, 2011.
- [22] Y. T. Sul, D. H. Kwon, B. S. Kang, S. Oh, and C. Johansson, “Experimental evidence for interfacial biochemical bonding in osseointegrated titanium implants,” *Clinical Oral Implants Research*, vol. 24, supplement 100, pp. 8–19, 2013.
- [23] A. Wennerberg, R. Jimbo, S. Stübinger, M. Obrecht, M. Dard, and S. Berner, “Nanostructures and hydrophilicity influence osseointegration: a biomechanical study in the rabbit tibia,” *Clinical Oral Implants Research*, 2013.
- [24] M. Monjo, S. F. Lamolle, S. P. Lyngstadaas, H. J. Rønold, and J. E. Ellingsen, “In vivo expression of osteogenic markers and bone mineral density at the surface of fluoride-modified titanium implants,” *Biomaterials*, vol. 29, no. 28, pp. 3771–3780, 2008.
- [25] S. Vandeweghe, C. Leconte, D. Ono, P. G. Coelho, and R. Jimbo, “Comparison of histological and three-dimensional characteristics of porous titanium granules and deproteinized bovine particulate grafts used for sinus floor augmentation in humans: a pilot study,” *Implant Dentistry*, vol. 22, no. 4, pp. 339–343, 2013.
- [26] S. Vandeweghe, P. G. Coelho, C. Vanhove, A. Wennerberg, and R. Jimbo, “Utilizing micro-computed tomography to evaluate bone structure surrounding dental implants: a comparison with histomorphometry,” *Journal of Biomedical Materials Research B*, vol. 101, no. 7, pp. 1259–1266, 2013.
- [27] M. S. Bryington, M. Hayashi, Y. Kozai et al., “The influence of nano hydroxyapatite coating on osseointegration after extended healing periods,” *Dental Materials*, vol. 29, no. 5, pp. 514–520, 2013.
- [28] H. Sarve, J. Lindblad, G. Borgefors, and C. B. Johansson, “Extracting 3D information on bone remodeling in the proximity of titanium implants in SR $\mu$ CT image volumes,” *Computer Methods and Programs in Biomedicine*, vol. 102, no. 1, pp. 25–34, 2011.
- [29] J. J. Pinzone, B. M. Hall, N. K. Thudi et al., “The role of Dickkopf-1 in bone development, homeostasis, and disease,” *Blood*, vol. 113, no. 3, pp. 517–525, 2009.
- [30] S. Cenci, M. N. Weitzmann, C. Roggia et al., “Estrogen deficiency induces bone loss by enhancing T-cell production of TNF- $\alpha$ ,” *Journal of Clinical Investigation*, vol. 106, no. 10, pp. 1229–1237, 2000.
- [31] L. Gilbert, X. He, P. Farmer et al., “Inhibition of osteoblast differentiation by tumor necrosis factor- $\alpha$ ,” *Endocrinology*, vol. 141, no. 11, pp. 3956–3964, 2000.
- [32] K. Niikura, M. Takano, and M. Sawada, “A novel inhibitor of vacuolar ATPase, FR167356, which can discriminate between osteoclast vacuolar ATPase and lysosomal vacuolar ATPase,” *The British Journal of Pharmacology*, vol. 142, no. 3, pp. 558–566, 2004.

## Research Article

# Bone-Forming Capabilities of a Newly Developed NanoHA Composite Alloplast Infused with Collagen: A Pilot Study in the Sheep Mandible

**Charles Marin,<sup>1</sup> Ryo Jimbo,<sup>2</sup> Fabio Cesar Lorenzoni,<sup>3,4</sup> Lukasz Witek,<sup>5</sup> Hellen Teixeira,<sup>3</sup> Estevam Bonfante,<sup>4</sup> Jose Gil,<sup>6</sup> Rodrigo Granato,<sup>6</sup> Nick Tovar,<sup>3</sup> and Paulo G. Coelho<sup>3,7</sup>**

<sup>1</sup> Department of Dentistry, UNIGRANRIO, 25071-202 Duque de Caxias, RJ, Brazil

<sup>2</sup> Department of Prosthodontics, Faculty of Odontology, Malmö University, 205 06 Malmö, Sweden

<sup>3</sup> Department of Biomaterials and Biomimetics, New York University, New York, NY 10010, USA

<sup>4</sup> Department of Prosthodontics, Integrated Center for Research, Bauru School of Dentistry, University of São Paulo, 17012-901 Bauru, SP, Brazil

<sup>5</sup> School of Chemical Engineering, Oklahoma State University, Stillwater, OK 74075, USA

<sup>6</sup> Postgraduate Program in Dentistry, UNIGRANRIO University-School of Health Sciences, 25071-202 Duque de Caxias, RJ, Brazil

<sup>7</sup> Department of Periodontology and Implant Dentistry, New York University College of Dentistry, NY 10010, USA

Correspondence should be addressed to Paulo G. Coelho; [pc92@nyu.edu](mailto:pc92@nyu.edu)

Received 28 July 2013; Accepted 1 September 2013

Academic Editor: Stefan Vandeweghe

Copyright © 2013 Charles Marin et al. This is an open access article distributed under the Creative Commons Attribution License, which permits unrestricted use, distribution, and reproduction in any medium, provided the original work is properly cited.

Lateral or vertical bone augmentation has always been a challenge, since the site is exposed to constant pressure from the soft tissue, and blood supply only exists from the donor site. Although, for such clinical cases, onlay grafting with autogenous bone is commonly selected, the invasiveness of the secondary surgical site and the relatively fast resorption rate have been reported as a drawback, which motivated the investigation of alternative approaches. This study evaluated the bone-forming capability of a novel nanoHA alloplast infused with collagen graft material made from biodegradable polylactic acid/polyglycolic acid versus a control graft material with the same synthesized alloplast without the nanoHA component and collagen infiltration. The status of newly formed bone and the resorption of the graft material were evaluated at 6 weeks *in vivo* histologically and three dimensionally by means of 3D microcomputed tomography. The histologic observation showed that newly formed bone ingrowth and internal resorption of the block were observed for the experimental blocks, whereas for the control blocks less bone ingrowth occurred along with lower resorption rate of the block material. The three-dimensional observation indicated that the experimental block maintained the external geometry, but at the same time successfully altered the graft material into bone. It is suggested that the combination of numerous factors contributed to the bone ingrowth and the novel development could be an alternative bone grafting choice.

## 1. Introduction

Oral implant treatment is one of the reliable treatment options in dentistry. Due to the conceptual changes in treatment planning, implants are today placed in a position so that the suprastructure can be reconstructed in both anatomically and aesthetically ideal configuration. However, in cases of severe atrophy especially in the aesthetically demanding maxillary anterior region, bone augmentation to gain volume may be necessary before an implant can be placed

to attain suitable bone architecture [1]. Since it has been suggested that bone volume (both height and width) has been considered as an important precondition to achieve long-term functional and aesthetic success [2, 3], a number of surgical techniques using various bone substitutes have been proposed to augment the bone volume [4, 5]. Conversely to particulate graft, which demands extra materials to guarantee space maintenance such as membrane barriers, the onlay graft does not require such approach since it is self-contained and has the potential to support itself by the soft tissue [6].



Additionally, onlay grafts are frequently employed to augment larger bone defects, whereas lamentably to date, the particulate grafting has not much clinical documentation to support its capabilities.

Materials used for onlay grafting are similar to those of the particulates, and it is an undeniable fact that some potential drawbacks associated with the use of autogenous [7, 8], allograft, and xenograft [9, 10] materials have been indicated. Although autogenous bone grafting is still the “gold standard,” the procedure is invasive for secondary surgical sites. Moreover, there always exist potential infection risks from allograft and xenograft materials. Further, xenografts have been reported in some long-term clinical studies that they actually interfere with the bone metabolism, and what seems to be maintaining bone volume is just delaying the biological healing [11, 12].

Such issues have directed attention towards the development of synthetic bone substitutes, that is, alloplastic [13], which have experienced considerable advances and are anticipated to provide comparable results to those achieved with the autograft [14].

In order to achieve requirements in bone tissue engineering, biomaterials, irrespective of their inherent features, should display qualities including osteoconductive and osteoinductive potentials, biocompatible and compatible with native bone in terms of porous and mechanical behavior [15]. Although a large array of alloplastic-based bone substitutes with different chemical and physical features have emerged directed towards successful tissue engineering [9], the tissue response is expected to be different from each other due to inherent characteristics of each material [16, 17].

The physicochemical and topographical aspects of biomaterials play an important role in osteoinductive mechanism in a biomaterial graft [18, 19]. For instance, the release of calcium and phosphate by calcium phosphate-based biomaterial seems to act as the most important factor involved in its bioactivity [20, 21]. In fact, a series of research studies based on the referred material have widely shown its osteoinductive potential [22–27]. Topographically speaking, a synthesized calcium phosphate with a specific microstructure has been reported to enhance the bone metabolism significantly by stimulating the macrophage activities thereby stimulating osteogenesis [19, 28]. Although osteoinduction mechanisms are still essentially unknown [29], it is worth to note that the ultimate aim is developing bioactive bone-graft substitutes suitable to effectively send signals in order to raise levels of osteoprogenitor cells in a physiological manner [6, 30]. Another important aspect is the mechanical properties, since an ideal onlay grafting material should maintain its intended morphology and, however, at the same time be able to be altered to bone. Thus, a graft material that acts as a scaffold and at the same time possessing an excellent mechanical property could fully alter the autogenic bone grafting procedure.

The aim of this pilot study is to histologically and three dimensionally observe the bone-forming capability of a novel synthetic alloplastic graft material presenting nanoHA and collagen infusion at the nanometer scale aimed for onlay graft application implanted on the bone mandible of sheep and removed at 6 weeks *in vivo*.

## 2. Material and Methods

**2.1. Synthetic Bone Blocks.** This study utilized two synthetic composite blocks (Intra-Lock International Boca Raton, Florida USA) (Patent Pending) labeled as control and experimental (Figure 1). The two blocks were made of a bio-composite of polylactic acid (PLA)/polyglycolic acid (PGA) and hydroxylapatite particles (HA). The experimental material presented the PLA/PGA scaffold and nanometer scale hydroxylapatite (HA) particles and were infused with collagen (experimental group). The control group presented the PLA/PGA scaffold structure and micrometer scale HA particles. The macrogeometric structure of both bone blocks was similar. At low magnification, scanning electron micrographs the difference in HA particle size was easily depicted between control (Figure 1(a)) and experimental blocks (Figure 1(b)). High magnification field-emission scanning electron micrographs depicted the nanoHA particles within the PLA/PGA matrix (Figure 1(c)) and collagen infusion between nanoHA particles (Figure 1(d)) for the experimental group.

The method of the whole process including the collagen infusion is proprietary and patent pending. The blocks produced for this experiment were cubic,  $10 \times 10 \times 10$  mm, and supplied sterile by gamma radiation. The blocks were then shaped with a surgical number 22 blade to a size of 10 mm in height, 10 mm in length, and 5 mm in width to obtain standard sizes for placement.

**2.2. Animals and Surgery.** Four sheep (approximately 6 months of age) were used for the study. This study was approved by the bioethics committee of Ecole Nationale Vétérinaire Maisons-Alfort, Paris, France.

The central region of the mandibular body on the lateral aspect was chosen for the procedure. All the procedures were performed under general anesthesia. Preanesthesia was made by means of intravenous (IV) Thiopental (15 mg/Kg) followed by orotracheal intubation. The inhalatory general anesthesia was maintained with isoflurane (2.5%), intramuscular (IM) ketamine (0.2 mg/Kg), and meloxicam (IM, 0.5 mg/Kg). After shaving and exposing the skin, an antiseptic solution with iodine was applied to the surgical site, as well as the surrounding area. An incision of 5 cm was made parallel to the inferior border of mandible. The platysma was dissected and cut in order to reach the periosteum, which was subsequently incised and reflected with periosteal elevator, and, finally, the mandibular body was exposed using manual retractors. The sites were prepared with a straight hand-piece at 900 rpm with abundant saline irrigation, and for each block, 5 perforations of 1.3 mm in diameter were made through the cortical bone. In brief, 4 perforations were made creating an 8 mm square, and an additional perforation was placed in the center of the square for eventual block fixation. Both control and experimental blocks were thereafter placed and fixed with  $14 \times 1.6$  mm screw. After fixation, the stability of blocks as well as the intimate contact among all sides of the blocks to the mandibular body was checked (Figure 2) and appropriate fixation stability was easily achieved due to the block resiliency. After saline irrigation, the surgical sites were sutured layer by layer

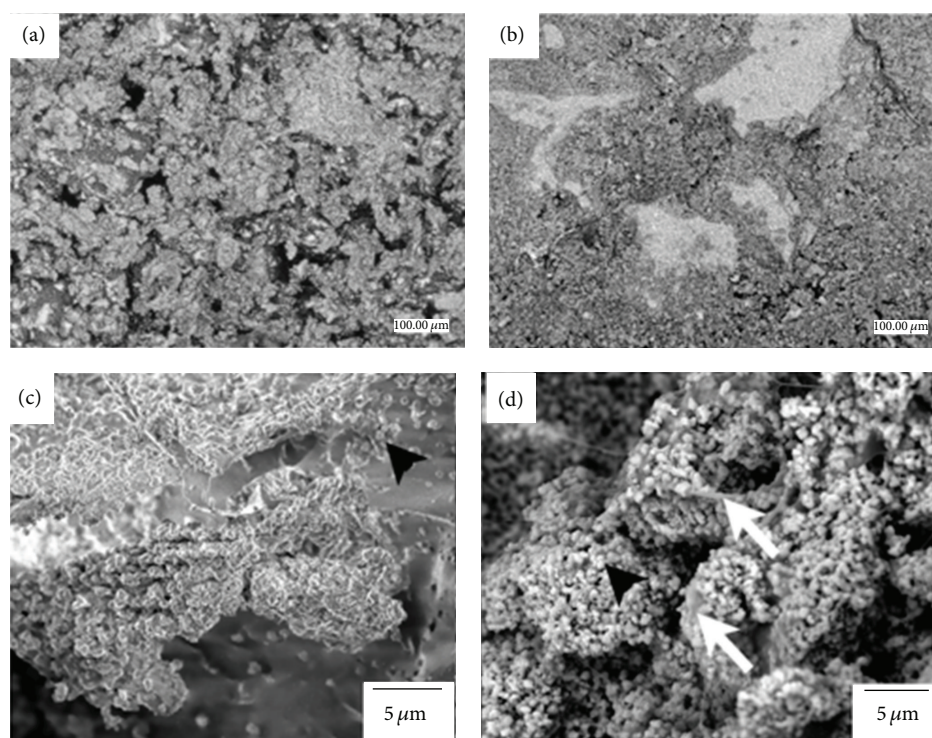


FIGURE 1: While the macrogeometric structure of both bone blocks were similar. At low magnification, scanning electron micrographs of the difference in HA particle size was easily depicted between (a) control and (b) experimental blocks. Field-emission scanning electron micrographs of the experimental group depicted the (c) nanoHA particles within the biopolymeric matrix (arrowheads) and that (d) collagen infusion took place at the nanometer scale (arrows).

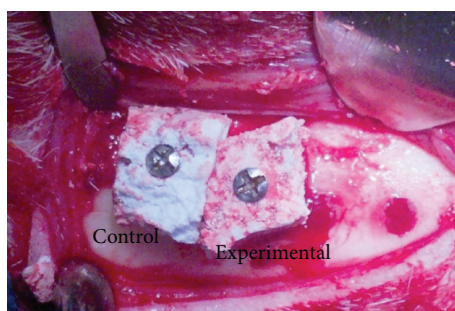


FIGURE 2: Clinical aspect of extraoral access utilized for the placement of control and experimental blocks. Blood wetting was observed throughout the volume of the experimental block material, whereas blood wetting was lower for the control block.

(internal layers: 3–0 vicryl, skin: 3–0 nylon). Postoperatively, all animals were given antibiotics (benzylpenicillin, 15 mg/Kg and dihydrostreptomycin 20 mg/Kg, IM) for 5 days, analgesics (patch of fentanyl, 3  $\mu$ g/h/kg, effect during 3 days) on the skin, and anti-inflammatory (meloxicam 0.5 mg/kg, IM) for two days. During the postoperative period, no signs of infection or other complications were observed. Euthanasia was performed after 6 weeks by anesthesia overdose, and the blocks/mandibular body was retrieved. After a careful removal of the surrounding soft tissue, the surgical site was exposed, and stability of blocks was checked. Thereafter, all samples were subjected to histological processing.

**2.3. Micro-CT Imaging and Histology.** The samples were fixed in 10% phosphate buffered formalin for 24 h and, thereafter, were gradually dehydrated in a series of ethanol concentrations. After dehydration, the samples were infiltrated and embedded in autopolymerizing methyl metacrylate resin. Upon the completion of the curing process, the embedded blocks were scanned by means of microcomputed tomography ( $\mu$ CT 40 Scanco Medical, Brüttisellen, Switzerland). The X-ray energy level was set at 70 kV, and a current of 114  $\mu$ A, with a slice resolution of 20  $\mu$ m. All data were exported in DICOM-format and imported in Amira software (Visage Imaging GmbH, Berlin, Germany) for evaluation. Manual

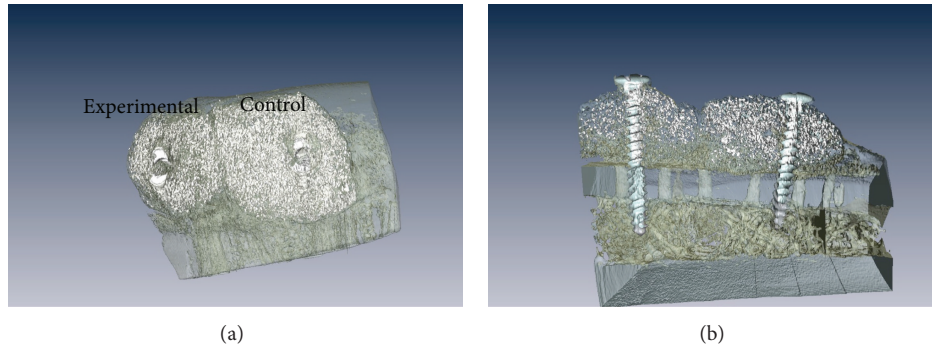


FIGURE 3: Three-dimensional reconstruction of the mandibular segment containing both experimental and control blocks. (a) Lateral view of the onlays depicted bone ongrowth on the lateral aspects of both blocks. (b) The cross-sectional reconstruction showed the perforations performed in the mandibular lateral aspect cortical (arrows). Bone ingrowth was observed at the region in immediate contact with the mandibular bone for both blocks; bone ingrowth throughout the volume of the block was only observed for the experimental group, which also presented lower amounts of synthetic material compared to the control group.

segmentation process employing semiautomatic or automatic segmenting tools was used to generate the 3D images.

After  $\mu$ CT imaging, all resin-embedded blocks were subjected to undecalcified ground sectioning. One central undecalcified cut and ground section was prepared from each sample with a slow speed precision diamond saw (Isomet 2000, Buehler Ltd., Lake Bluff, USA). The sections were ground to a final thickness of about  $90\ \mu\text{m}$  and stained with Stevenel's Blue and Van Giesons Picro-Fuchsin. A slide scanner ScanScope GL (Aperio Technologies, Inc., Vista, CA) was used for the histological observation.

### 3. Results

During surgery for block placement, blood wetting was observed throughout the volume of the experimental block material, while noticeable lower wetting was lower for the control block (Figure 2).

Postoperative clinical evaluation revealed that the augmented sites did not present any complication (absence of inflammation, infection, etc.) throughout the 6 weeks healing period. The sheep were allowed to eat as soon as fully recovered from general anesthesia and did not present substantial weight gain or loss thereafter.

Immediately following euthanasia, sharp dissection of the mandibular region did not reveal any clinical sign of inflammation or infection, and it was clinically evident that no substantial degradation of both biomaterial blocks existed, and those were in the placement position held by the titanium screw. New bone formation was evident in regions surrounding the biomaterial blocks.

The  $\mu$ CT reconstruction of the augmented regions showed bone growth around both control and experimental blocks (Figure 3). Bone ongrowth onto the biomaterial block surfaces was depicted for both groups. However, while bone ingrowth was observed at the region in immediate contact with the mandibular bone for both blocks, bone ingrowth throughout the volume of the block was only observed for the experimental group, which also presented lower amounts of synthetic material compared to the control group (Figure 3).

The histologic sections confirmed the difference in healing pattern observed through three-dimensional reconstruction (Figure 4), where bone ingrowth occurred throughout the volume of the experimental block material, and little ingrowth occurred for the control block material. Smaller amounts of synthetic material were also observed for the experimental block relative to the control block material.

### 4. Discussion

It has been a general consensus that the expected clinical outcome of ectopic onlay grafts intended for lateral or vertical augmentation is unstable regardless of the graft origin. This is due to the fact that initial vascularization (blood supply) occurs only from the bottom of the graft and may be insufficient for the graft to be successfully altered by newly formed bone before the graft collapses from the constant tension of the soft tissue or is resorbed by the active macrophages.

The histological and three-dimensional observation of the control sites depicted that the graft material lacked new bone ingrowth and for some locations, and soft tissue encapsulation could be observed. The control alloplast at 6 weeks presented some degree of soft tissue incorporation inside the block. On the other hand, active new bone ingrowth was notable within the experimental graft material. Of note is that compared to the control blocks where the block maintained its shape both externally and internally, the experimental blocks seemed to have degraded and/or resorbed, while newly formed bone filled the spaces originally occupied by the grafting material bulk. Further, remaining block material seemed to be in contact to the aligning newly formed bone. This is an indication that bone metabolism has been stimulated due to the graft material and is in accordance with the reports from Ono et al. (2011), where in their lateral augmentation model, they found more amount of newly formed bone for surface modified beta-tricalcium phosphate blocks than the control without modification [19]. By using enzyme histochemistry, they confirmed that vigorous osteoclastic activity accompanied new bone formation expressing alkaline phosphatase, presenting constant block material



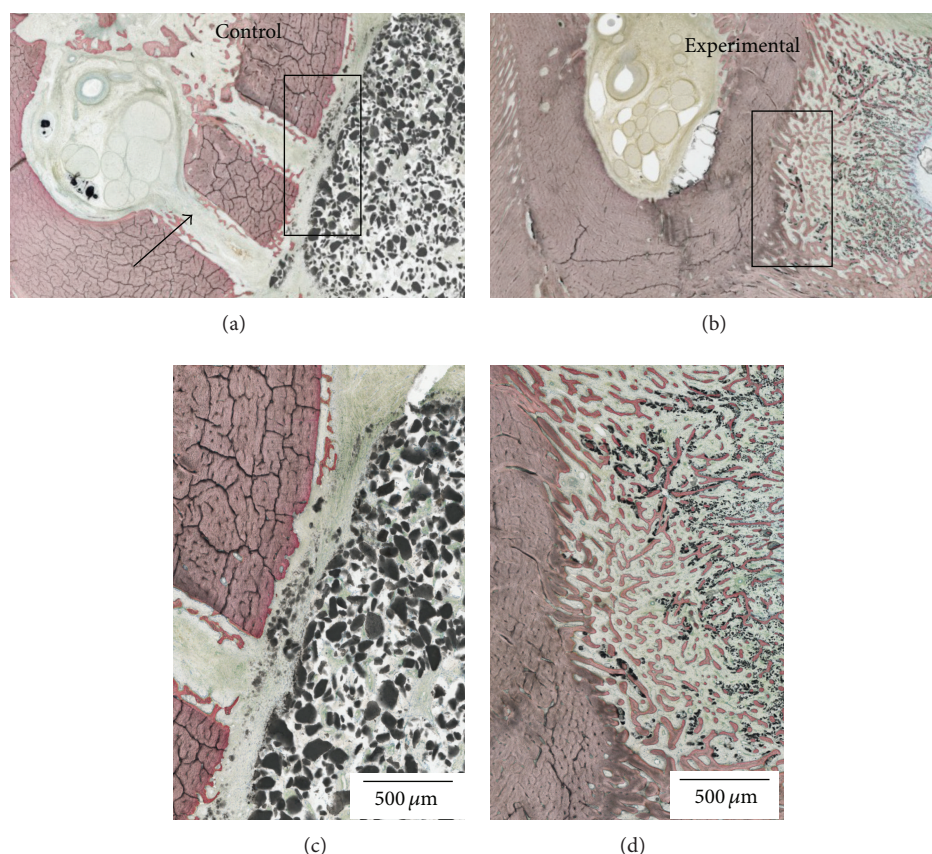


FIGURE 4: Histologic sections for the (a) control and (b) experimental block materials placed on the lateral aspect of the mandible. The histologic sections revealed the perforations performed in the mandibular lateral aspect cortical (arrows). Higher magnification of the (c) control and (d) experimental blocks showed that bone ingrowth occurred throughout the volume of the experimental block material, and little ingrowth occurred for the control block material. Smaller amounts of synthetic material were also observed for the experimental block relative to the control block material.

resorption and new bone apposition simultaneously. It was suggested that successful bone alteration could be dependent on the topography (including porosity) and chemistry of the synthesized blocks as in the case for the present pilot study. Since the major difference in the two synthesized blocks is the HA particle size and collagen infusion, such nanometer scale features may be separate or in tandem be accounted for the difference in bone healing kinetics.

He et al. (2012) have previously reported that the infiltration of collagen to porous hydroxyapatite improved mesenchymal stem cell adhesion, proliferation, and differentiation [31]. They suggested that the self-reconstruction property of the collagen enhanced fibrous network formation, and it can be a potential carrier for other proteins and cytokines. This effect has been clinically suggested to be effective as Simion et al. have shown that collagen matrix could be applied for an effective scaffold for tissue regeneration [32].

Another added feature by the thorough infiltration of collagen is increased hydrophilicity. Our surgical procedures showed that immediately after placement of the experimental blocks to the decortified surgical site, blood infiltrated the entire block indicating its extreme hydrophilicity compared to the control blocks. This has been reported to be one of the features when collagen is combined with biodegradable

materials that the collagen increases the material hydrophilicity [33]. As it has been well described that the hydrophilicity is important for osteogenic cell responses [34–37], it can be assumed that the physiological cascade of events further leads to the formation of new bone.

Finally, it can be speculated that the improved bone-forming properties seen with the experimental block were achieved due to the combination of multiple factors such as the structural biomechanical strength that maintained the original external geometry, the micrometer level and related nanometer scale structure of the composite created by the synthesis and infiltration of the collagen and its distribution, surface energy including hydrophilicity, and perhaps others. Multivariable experimental studies are under way to explore the potential of this promising novel grafting material.

## Conflict of Interests

The authors declare that they have no conflict of interests.

## Acknowledgments

This study was partially funded by Intra-Lock International, Boca Raton, Florida, USA, and by the division of Oral and

Maxillofacial Surgery at Federal University of Santa Catarina.

## References

- [1] S. Wallace and R. Gellin, "Clinical evaluation of freeze-dried cancellous block allografts for ridge augmentation and implant placement in the maxilla," *Implant Dentistry*, vol. 19, no. 4, pp. 272–279, 2010.
- [2] M. Hof, B. Pommer, G. D. Strbac, D. Sütö, G. Watzek, and W. Zechner, "Esthetic evaluation of single-tooth implants in the anterior maxilla following autologous bone augmentation," *Clinical Oral Implants Research*, vol. 24, supplement 100, pp. 88–93, 2011.
- [3] P. J. Henry, W. R. Laney, T. Jemt et al., "Osseointegrated implants for single-tooth replacement: a prospective 5-year multicenter study," *The International Journal of Oral & Maxillofacial Implants*, vol. 11, no. 4, pp. 450–455, 1996.
- [4] A. R. Sánchez, P. J. Sheridan, S. E. Eckert, and A. L. Weaver, "Influence of platelet-rich plasma added to xenogeneic bone grafts in periimplant defects: a vital fluorescence study in dogs," *Clinical Implant Dentistry and Related Research*, vol. 7, no. 2, pp. 61–69, 2005.
- [5] M. Simion, P. Trisi, and A. Piattelli, "GBR with an e-PTFE membrane associated with DFDBA: histologic and histochemical analysis in a human implant retrieved after 4 years of loading," *The International Journal of Periodontics & Restorative Dentistry*, vol. 16, no. 4, pp. 338–347, 1996.
- [6] W. F. Zambuzzi, P. G. Coelho, G. G. Alves, and J. M. Granjeiro, "Intracellular signal transduction as a factor in the development of "Smart" biomaterials for bone tissue engineering," *Biotechnology and Bioengineering*, vol. 108, no. 6, pp. 1246–1250, 2011.
- [7] O. Bahat and R. V. Fontanesi, "Complications of grafting in the atrophic edentulous or partially edentulous jaw," *The International Journal of Periodontics & Restorative Dentistry*, vol. 21, no. 5, pp. 487–495, 2001.
- [8] E. Nkenke, S. Schultze-Mosgau, M. Radespiel-Tiöger, F. Kloss, and F. W. Neukam, "Morbidity of harvesting of chin grafts: a prospective study," *Clinical Oral Implants Research*, vol. 12, no. 5, pp. 495–502, 2001.
- [9] W. R. Moore, S. E. Graves, and G. I. Bain, "Synthetic bone graft substitutes," *ANZ Journal of Surgery*, vol. 71, no. 6, pp. 354–361, 2001.
- [10] M. Mastrogiacomo, A. Muraglia, V. Komlev et al., "Tissue engineering of bone: search for a better scaffold," *Orthodontics & Craniofacial Research*, vol. 8, no. 4, pp. 277–284, 2005.
- [11] M. Araújo, E. Linder, and J. Lindhe, "Effect of a xenograft on early bone formation in extraction sockets: an experimental study in dog," *Clinical Oral Implants Research*, vol. 20, no. 1, pp. 1–6, 2009.
- [12] M. Araújo, E. Linder, J. Wennström, and J. Lindhe, "The influence of bio-oss collagen on healing of an extraction socket: an experimental study in the dog," *The International Journal of Periodontics & Restorative Dentistry*, vol. 28, no. 2, pp. 123–135, 2008.
- [13] R. V. da Silva, C. A. Bertran, E. Y. Kawachi, and J. A. Camilli, "Repair of cranial bone defects with calcium phosphate ceramic implant or autogenous bone graft," *Journal of Craniofacial Surgery*, vol. 18, no. 2, pp. 281–286, 2007.
- [14] K. J. Zouhary, "Bone graft harvesting from distant sites: concepts and techniques," *Oral and Maxillofacial Surgery Clinics of North America*, vol. 22, no. 3, pp. 301–316, 2010.
- [15] A. El-Ghannam, "Bone reconstruction: from bioceramics to tissue engineering," *Expert Review of Medical Devices*, vol. 2, no. 1, pp. 87–101, 2005.
- [16] H. Yuan, C. A. van Blitterswijk, K. de Groot, and J. D. de Bruijn, "A comparison of bone formation in biphasic calcium phosphate (BCP) and hydroxyapatite (HA) implanted in muscle and bone of dogs at different time periods," *Journal of Biomedical Materials Research A*, vol. 78, no. 1, pp. 139–147, 2006.
- [17] G. Daculsi, O. Laboux, O. Malarid, and P. Weiss, "Current state of the art of biphasic calcium phosphate bioceramics," *Journal of Materials Science*, vol. 14, no. 3, pp. 195–200, 2003.
- [18] P. Habibovic and K. de Groot, "Osteoinductive biomaterials—properties and relevance in bone repair," *Journal of Tissue Engineering and Regenerative Medicine*, vol. 1, no. 1, pp. 25–32, 2007.
- [19] D. Ono, R. Jimbo, G. Kawachi, K. Ioku, T. Ikeda, and T. Sawase, "Lateral bone augmentation with newly developed  $\beta$ -tricalcium phosphate block: an experimental study in the rabbit mandible," *Clinical Oral Implants Research*, vol. 22, no. 12, pp. 1366–1371, 2011.
- [20] R. G. T. Geesink, K. de Groot, and C. P. A. T. Klein, "Bonding of bone to apatite-coated implants," *Journal of Bone and Joint Surgery B*, vol. 70, no. 1, pp. 17–22, 1988.
- [21] A. Wennerberg, R. Jimbo, S. Allard et al., "In vivo stability of hydroxyapatite nanoparticles coated on titanium implant surfaces," *The International Journal of Oral & Maxillofacial Implants*, vol. 26, no. 6, pp. 1161–1166, 2011.
- [22] H. Yuan, Z. Yang, J. D. de Bruijn, K. de Groot, and X. Zhang, "Material-dependent bone induction by calcium phosphate ceramics: a 2.5-year study in dog," *Biomaterials*, vol. 22, no. 19, pp. 2617–2623, 2001.
- [23] H. Yamasaki, "Heterotopic bone formation around porous hydroxyapatite ceramics in the subcutis of dogs," *Japanese Journal of Oral Biology*, vol. 32, no. 2, pp. 190–192, 1990.
- [24] H. Yamasaki and H. Sakai, "Osteogenic response to porous hydroxyapatite ceramics under the skin of dogs," *Biomaterials*, vol. 13, no. 5, pp. 308–312, 1992.
- [25] U. Ripamonti, "Osteoinduction in porous hydroxyapatite implanted in heterotopic sites of different animal models," *Biomaterials*, vol. 17, no. 1, pp. 31–35, 1996.
- [26] H. Yuan, Z. Yang, Y. Li, X. Zhang, J. D. de Bruijn, and K. de Groot, "Osteoinduction by calcium phosphate biomaterials," *Journal of Materials Science*, vol. 9, no. 12, pp. 723–726, 1998.
- [27] R.-N. Yang, F. Ye, L.-J. Cheng et al., "Osteoinduction by Ca-P biomaterials implanted into the muscles of mice," *Journal of Zhejiang University B*, vol. 12, no. 7, pp. 582–590, 2011.
- [28] T. Okuda, K. Ioku, I. Yonezawa et al., "The slow resorption with replacement by bone of a hydrothermally synthesized pure calcium-deficient hydroxyapatite," *Biomaterials*, vol. 29, no. 18, pp. 2719–2728, 2008.
- [29] P. Habibovic, H. Yuan, C. M. van der Valk, G. Meijer, C. A. van Blitterswijk, and K. De Groot, "3D microenvironment as essential element for osteoinduction by biomaterials," *Biomaterials*, vol. 26, no. 17, pp. 3565–3575, 2005.
- [30] R. Z. LeGeros, "Properties of osteoconductive biomaterials: calcium phosphates," *Clinical Orthopaedics and Related Research*, no. 395, pp. 81–98, 2002.
- [31] J. He, T. Huang, L. Gan et al., "Collagen-infiltrated porous hydroxyapatite coating and its osteogenic properties: in vitro and in vivo study," *Journal of Biomedical Materials Research A*, vol. 100, no. 7, pp. 1706–1715, 2012.

- [32] M. Simion, I. Rocchietta, F. Fontana et al., "Evaluation of a resorbable collagen matrixinfused with rhPDGF-BB in peri-implant soft tissue augmentation: a preliminary report with 3.5 years of observation," *The International Journal of Periodontics & Restorative Dentistry*, vol. 32, no. 3, pp. 273–282, 2012.
- [33] G. Chen, T. Ushida, and T. Tateishi, "A biodegradable hybrid sponge nested with collagen microsponges," *Journal of Biomedical Materials Research*, vol. 51, no. 2, pp. 273–279, 2000.
- [34] M. Hayashi, R. Jimbo, L. Lindh et al., "In vitro characterization and osteoblast responses to nanostructured photocatalytic TiO<sub>2</sub> coated surfaces," *Acta Biomaterialia*, vol. 8, no. 6, pp. 2411–2416, 2012.
- [35] R. Jimbo, D. Ono, Y. Hirakawa, T. Odatsu, T. Tanaka, and T. Sawase, "Accelerated photo-induced hydrophilicity promotes osseointegration: an animal study," *Clinical Implant Dentistry and Related Research*, vol. 13, no. 1, pp. 79–85, 2011.
- [36] R. Jimbo, T. Sawase, K. Baba, T. Kurogi, Y. Shibata, and M. Atsuta, "Enhanced initial cell responses to chemically modified anodized titanium," *Clinical Implant Dentistry and Related Research*, vol. 10, no. 1, pp. 55–61, 2008.
- [37] T. Sawase, R. Jimbo, K. Baba, Y. Shibata, T. Ikeda, and M. Atsuta, "Photo-induced hydrophilicity enhances initial cell behavior and early bone apposition," *Clinical Oral Implants Research*, vol. 19, no. 5, pp. 491–496, 2008.

## Research Article

# Characteristics of 2 Different Commercially Available Implants with or without Nanotopography

Ali Alenezi,<sup>1</sup> Yoshihito Naito,<sup>1,2</sup> Martin Andersson,<sup>3</sup> Bruno R. Chrcanovic,<sup>1</sup>  
Ann Wennerberg,<sup>1</sup> and Ryo Jimbo<sup>1</sup>

<sup>1</sup> Department of Prosthodontics, Faculty of Odontology, Malmö University, 205 06 Malmö, Sweden

<sup>2</sup> Department of Oral and Maxillofacial Prosthodontics and Oral Implantology, Institute of Health Biosciences, The University of Tokushima Graduate School, 3-18-15 Kuramotocho, Tokushima 770-8504, Japan

<sup>3</sup> Department of Chemical and Biological Engineering, Applied Surface Chemistry, Chalmers University of Technology, 412 96 Gothenburg, Sweden

Correspondence should be addressed to Ali Alenezi; [ali.alenezi@mah.se](mailto:ali.alenezi@mah.se)

Received 12 June 2013; Accepted 21 July 2013

Academic Editor: Stefan Vandeweghe

Copyright © 2013 Ali Alenezi et al. This is an open access article distributed under the Creative Commons Attribution License, which permits unrestricted use, distribution, and reproduction in any medium, provided the original work is properly cited.

The aim of this study was to assess histologically and histomorphometrically the early bone forming properties after 3 weeks for 2 commercially available implants, one supposedly possessing nanotopography and one without, in a rabbit femur model. Twenty-four implants divided equally into 2 groups were utilized in this study. The first group (P-I MICRO+NANO) was a titanium oxide (TiO<sub>2</sub>) microblasted and noble gas ion bombarded surface while the second group (Ospol) was anodic oxidized surface with calcium and phosphate incorporation. The implants were placed in the rabbit femur uncortically and were allowed to heal for 3 weeks. After euthanasia, the samples were subjected to histologic sectioning and bone-implant contact and bone area were evaluated histomorphometrically under an optical microscope. The histomorphometric evaluation presented that the P-I MICRO+NANO implants demonstrated significantly higher new bone formation as compared to the Ospol implants. Within the limitations of this study, the results suggested that nanostructures presented significantly higher bone formation after 3 weeks *in vivo*, and the effect of chemistry was limited, which is indicative that nanotopography is effective at early healing periods.

## 1. Introduction

Replacing a missing tooth with endosseous implants has been recognized as a long-term successful treatment option [1, 2]. Recent research trends further focus on enhancing the bone in apposition to the implant to ensure rapid and firm osseointegration. The major factors influencing the bone response around implants are reported to be the implant macrodesign, surface topography, and surface chemistry, which have been investigated in numerous studies [3–5]. Surface topography in particular has drawn significant attention as an important factor since it has been suggested that moderately rough implant surfaces present the strongest bone responses [6–8]. Alteration of the surface topography can be conducted in various methods, which provide unique characteristics [9]. Roughening the surface with blasting particles along with different types of acid etching is a commonly utilized

technique to modify the surface topography [10, 11]. This method is unique in a way that the roughness can be altered in a controlled manner by changing the velocity, particle size, and particle properties [12]. Furthermore, the acid etching not only cleans off the remnants of the particles, but creates a unique surface topography, which has also been reported to alter the surface chemistry [13, 14]. It has been presented in numerous *in vivo* studies that this type of modification can enhance bone regeneration which is believed to be due increase in the surface area gained by surface roughness [10, 15–17]. With regards to the effect of chemistry, it has been reported that elements such as calcium and phosphate have significant influence on bone formation [18, 19]. It has also been reported that chemically modified surfaces provide a specific bonding between the implant and the surface, which has been described as biochemical bonding [20, 21]. One of the recognized methods to chemically modify the



surface is the anodic oxidation technique. It is a method to increase the thickness of the oxide layer with a possibility to incorporate elements such as magnesium and phosphates and also provide a unique porous topography [20–23]. It has been proven that this modification significantly improves both the rate and quality of osseointegration [20].

In order to further enhance osseointegration, recent research has focused on modifying the topography at the nanolevel, since cells and proteins are reportedly interacting at this level [24, 25]. Reports suggest that *in vitro* these features could modify cellular shape and influence the migration and differentiation of mesenchymal stem cells [24–30]. It has been reported in several studies that the application of nanostructures increases the bioactivity of the implant surface which leads to an enhanced bone apposition around implants [31–33].

Although both nanotopographical and chemical modifications have proven to be an enhancing factor for osseointegration, it is of great interest to observe the bone forming characteristics of commercially available implants possessing either one of the factors. In this study, two commercially available implants, one supposedly possessing intended nanostructures formed by a noble gas ion bombardment and another chemically modified implant with calcium incorporated anodic oxidation, were characterized by various methods. Thereafter, the two commercially available implants were placed in the rabbit femur to observe histologically and histomorphometrically the early bone forming properties of 3 weeks.

## 2. Materials and Methods

**2.1. Implant Surface Preparation and Characterization.** Twenty-four implants divided into 2 groups were used in this study. The first group ( $n = 12$ ) was a titanium oxide ( $\text{TiO}_2$ ) microblasted and noble gas ion bombarded surface (Functional hybrid implants, P-I MICRO+NANO, Zimmer Dental), with a diameter of 3.75 mm and length of 11.5 mm.

The second group ( $n = 12$ ) was an anodic oxidized surface with calcium and phosphate incorporation (Ospol surface, Ospol, Zimmer Dental), with a diameter of 3.9 mm and length of 8.0 mm.

**2.2. Interferometer.** Topographical analyses at microlevel were performed with interferometry (MicroXAM—PhaseShift, Tucson, AZ, USA). Following guidelines that were suggested by Wennerberg and Albrektsson [34], three implants from each group were examined in order to characterize the surface roughness. Each implant was examined at 9 different positions (3 top areas, 3 valley areas, and 3 flank areas). Parametric calculations were performed after errors of form and waviness were removed using a  $50 \times 50$  mm Gaussian filter. Data was collected from the following three-dimensional parameters: the arithmetic mean of the height variation from a mean plane,  $S_a$  ( $\mu\text{m}$ ); the density of summits,  $S_d$  ( $\mu\text{m}^{-2}$ ); and the developed surface area added by the roughness,  $S_{dr}$  (%). (Measurement area:  $200 \mu\text{m} \times 250 \mu\text{m}$ .)

The evaluation was performed with the Surfscan software, and the images were produced using MountainsMap universal 6.2 software.

**2.3. Atomic Force Microscopy.** The topographies of P-I MICRO+NANO and Ospol surfaces were characterized at nanolevel using atomic force microscopy (XE-100, Park systems). The analysis was performed in noncontact mode using silicon nitride probe with a nominal resonance frequency between 200 and 400 kHz (ACTA-10, APPNANO, USA). For this test, discs with the same implant surface treatment were used (3 discs for each group). Measurements areas of  $(10 \times 10)$  and  $(1 \times 1)$  in three random positions were selected for each disc. The measurements were performed at a scan rate of 0.50 Hz.

The raw data obtained from the topographical equipment were further processed to separate the form, waviness, and roughness from the original measurements. A Gaussian high-pass filter was used (25% of surface area). The Gaussian filter is suitable for smoothing surfaces with rich features. The parameters used to calculate surface roughness were the same ones used with interferometer which are:  $S_a$ ,  $S_d$ , and  $S_{dr}$ . Analysis and processing of the AFM images were performed with the MountainsMap Universal 6.2 software.

**2.4. Scanning Electron Microscopy.** The surface morphologies of 2 discs from each group were examined by scanning electron microscopy (SEM) using an LEO Ultra 55 FEG (Zeiss, Oberkochen, Germany) at an accelerating voltage of 5 kV. A secondary electron in-lens detector was used for visualization.

**2.5. X-Ray Photoelectron Spectroscopy.** The surface chemistry was investigated using X-ray photoelectron spectroscopy (XPS) utilizing a Kratos Axis Ultra XPS instrument equipped with a monochromatic  $\text{Al K}\alpha$  X-ray source. Binding energies between 0 and 1100 eV were monitored, 0.800 eV/step and 50 ms/step, at a pass energy of 187.85 eV (150 W). One implant from each group was examined.

**2.6. Animals and Surgery.** The study was approved by the Malmö/Lund, Sweden, Regional Animal Ethical Committee. Twelve rabbits were included of mixed sexes with an average weight of approximately 4 kg.

Before surgery, the animals were sedated by intramuscular injections of a mixture of 0.15 mL/kg of medetomidine (1 mg/mL Dormitor—Orion Pharma, Sollentuna, Sweden) and 0.35 mL/kg of ketamine hydrochloride (50 mg/mL Ketalar—Pfizer AB, Sollentuna, Sweden). The hind legs were shaved and disinfected with 70% ethanol and 70% chlorhexidine. Lidocaine hydrochloride (Xylocaine—AstraZeneca AB, Gothenburg, Sweden) was administrated as local anesthetic at each insertion site at a dose of 1 mL. After osteotomy preparation following the manufacturers instructions, the implants were inserted in both sides of the femur. After the operation, buprenorphine hydrochloride (0.5 mL Temgesic—Reckitt Benckiser, Slough, UK) was administered as an

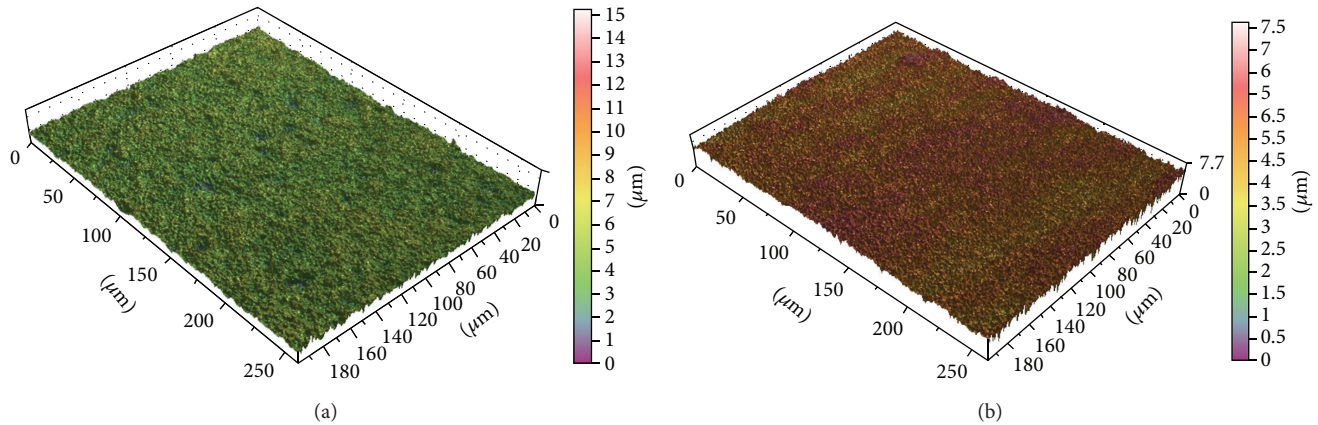


FIGURE 1: Representative interferometer images of 3D surface topography of the (a) P-I MICRO+NANO and (b) Ospol discs.

TABLE 1: Surface roughness measurements for implants of the two groups using interferometer (9 measurements/implant,  $n = 3$ ).

Sample	Sa $\mu\text{m}$ (SD)	Sds/ $\text{mm}^2$ (SD)	Sdr % (SD)
P-I MICRO+NANO	0.6070 $\mu\text{m}$ (0.075)	186758 $\text{mm}^2$ (20462)	30.39% (8.45)
OSPOL	0.3599 $\mu\text{m}$ (0.090)	244573 $\text{mm}^2$ (41090)	44.08% (32.25)

TABLE 2: Surface roughness measurement using the AFM (scan size  $10 \times 10$ ).

Scan size $10 \times 10$	Sa $\mu\text{m}$ (SD)	Sdr % (SD)	Sds $1/\mu\text{m}^2$ (SD)
P-I MICRO+NANO	0.051 (0.007)	8.49 (3.59)	9.59555 (5.20)
OSPOL	0.058 (0.005)	11.44 (1.27)	3.08 (0.30)

analgesic for 3 days. After 3 weeks, the rabbits were euthanized with an overdose (60 mg/mL) of pentobarbital sodium (Apoteksbolaget AB, Stockholm, Sweden).

**2.7. Histology and Histomorphometry.** After euthanasia, the samples were processed in series of dehydrations in ethanol and infiltrations in resin; they were embedded in light-curing resin (Technovit 7200 VLC—Heraeus Kulzer, Wehrheim, Germany). Thereafter, the resin-embedded samples were subjected to undecalcified ground sectioning. One central ground section was prepared from each block by using the Exakt sawing and grinding equipment [35]. The sections were ground to a final thickness of approximately  $20 \mu\text{m}$  and histologically stained with toluidine blue and pyronin G.

Histological evaluations were performed using a light microscope (Eclipse ME600—Nikon Co., Tokyo, Japan), and the histomorphometrical data were analyzed by image analysis software (Image J v. 1.43u—National Institutes of Health, Bethesda, MD, USA). The bone-implant contact (BIC) percentage and the bone area (BA) and the new bone area (new-BA) percentages along the implant for total bone and new bone were calculated. New bone formation surrounding the implants was used for evaluating the osteoconductivity.

**2.8. Statistical Analysis.** For the histological evaluation, the wilcoxon rank-sum test was used for statistical analysis. For interferometer and AFM measurements, the mean values of

surface roughness were compared with those of Independent-samples  $t$ -test using Statistical Package for the Social Sciences (SPSS) version 20 software (SPSS Inc., Chicago, USA). The degree of statistical significance was considered  $P < 0.05$ .

### 3. Results

**3.1. Topographical Characterization.** The results of the interferometer measurements are presented in Table 1. The average height deviation (Sa) was significantly different between the two groups ( $P = 0.000$ ). Both surfaces were smooth according to the definition by Albrektsson and Wennerberg [3].

Further, the number of summits per unit area (Sds) differed significantly among the surfaces, with the Ospol surface presenting higher values than the P-I MICRO+NANO surface ( $P = 0.000$ ).

The surface enlargement percentage (Sdr) showed that the Ospol surface had a significantly larger surface area than the P-I MICRO+NANO surface ( $P = 0.028$ ). Figure 1 shows Interferometer images of 3D surface topography of the P-I MICRO+NANO and Ospol discs.

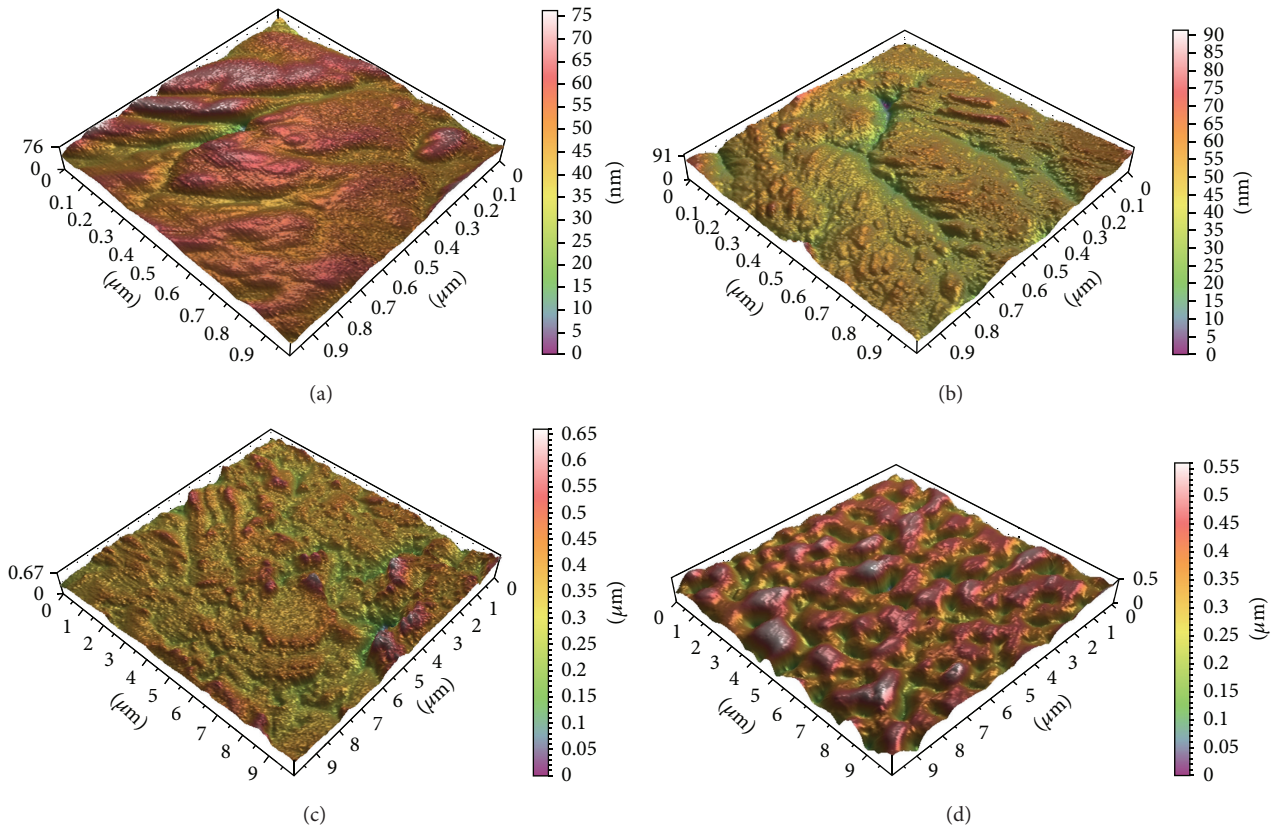
In contrast to the interferometer analysis, high-resolution topographical analysis with the AFM showed decreased surface roughness for the P-I MICRO+NANO compared to Ospol discs. The Sa, Sds, and Sdr parameters of the two groups at  $10 \times 10$  scan size are presented in Table 2. The statistical analysis showed significant differences in Sdr and Sds values ( $P = 0.027$  and  $0.002$ , resp.).

TABLE 3: Surface roughness measurement using the AFM (scan size  $1 \times 1$ ).

Scan size $1 \times 1$	Sa nm (SD)	Sdr % (SD)	Sds $1/\mu\text{m}^2$ (SD)
P-I MICRO+NANO	4.35 (1.36)	8.56 (7)	1533 (671)
OSPOL	5.18 (1.11)	8.9 (3.70)	2295.2 (734)

TABLE 4: Surface chemical composition (atomic %) using XPS.

Element	C1s	N1s	O1s	P2p	Ca2p	Ti2p
P-I MICRO+NANO	22.75	1.07	56.77		0.88	18.53
OSPOL	17.51	0.46	58.88	2.38	2.23	18.55

FIGURE 2: Representative AFM images of the 3D surface topography of (a) P-I MICRO+NANO, (b) Ospol discs at  $1 \times 1$  scan area, (c) P-I MICRO+NANO, and (d) Ospol discs at  $10 \times 10$  scan area.

For the  $1 \times 1$  scan size, the Sa, Sds, and Sdr parameters are presented in Table 3. The statistical analysis shows significant difference only in the Sds value ( $P = 0.035$ ). Representative AFM images of the 3D surface topography of the P-I MICRO+NANO and Ospol discs for both scan ranges are presented in Figure 2.

**3.2. Scanning Electron Microscopy.** Scanning electron microscopy images of the P-I MICRO+NANO and Ospol discs are presented in Figure 3. At high magnification, P-I MICRO+NANO surface showed distinct, distributed, nanosized bumps with nanoparticles less than 100 nm in size. Ospol surface on the other hand showed extremely smooth surface with porous structures distributed on the surface with a diameter of approximately 300–500 nm.

**3.3. X-Ray Photoelectron Spectroscopy.** XPS survey spectra for the P-I MICRO+NANO and Ospol implants are presented in Figure 4, and the surface chemical composition is presented in Table 4. As it can be seen in the table, the largest difference between the two surfaces is the presence of calcium and phosphate on the Ospol surface. However, a relatively small amount of calcium was observed also on the P-I MICRO+NANO surface. Carbon and small quantities of nitrogen were present on both implants, which most probably is due to contamination.

**3.4. Histology and Histomorphometry.** A descriptive histologic image for both groups is presented in Figure 5. In brief, deeply stained woven bone was formed along the implant,



TABLE 5: Summary of the histomorphometric measurements.

Group	BIC %	BIC %	BA %	BA %	New BA %	New BA %
	(All threads) (SD)	(Top 3 threads) (SD)	(All threads) (SD)	(Top 3 threads) (SD)	(All threads) (SD)	(Top 3 threads) (SD)
P-I MICRO+NANO	54.33 (14.7)	59.25 (12.9)	54.75 (8.4)	57.166 (10.1)	46.416 (9.4)	47.25 (10.15)
OSPOL	52.75 (15)	58.08 (14.7)	52.41 (13.8)	59.083 (13.9)	35.83 (10.6)	36.416 (11.3)

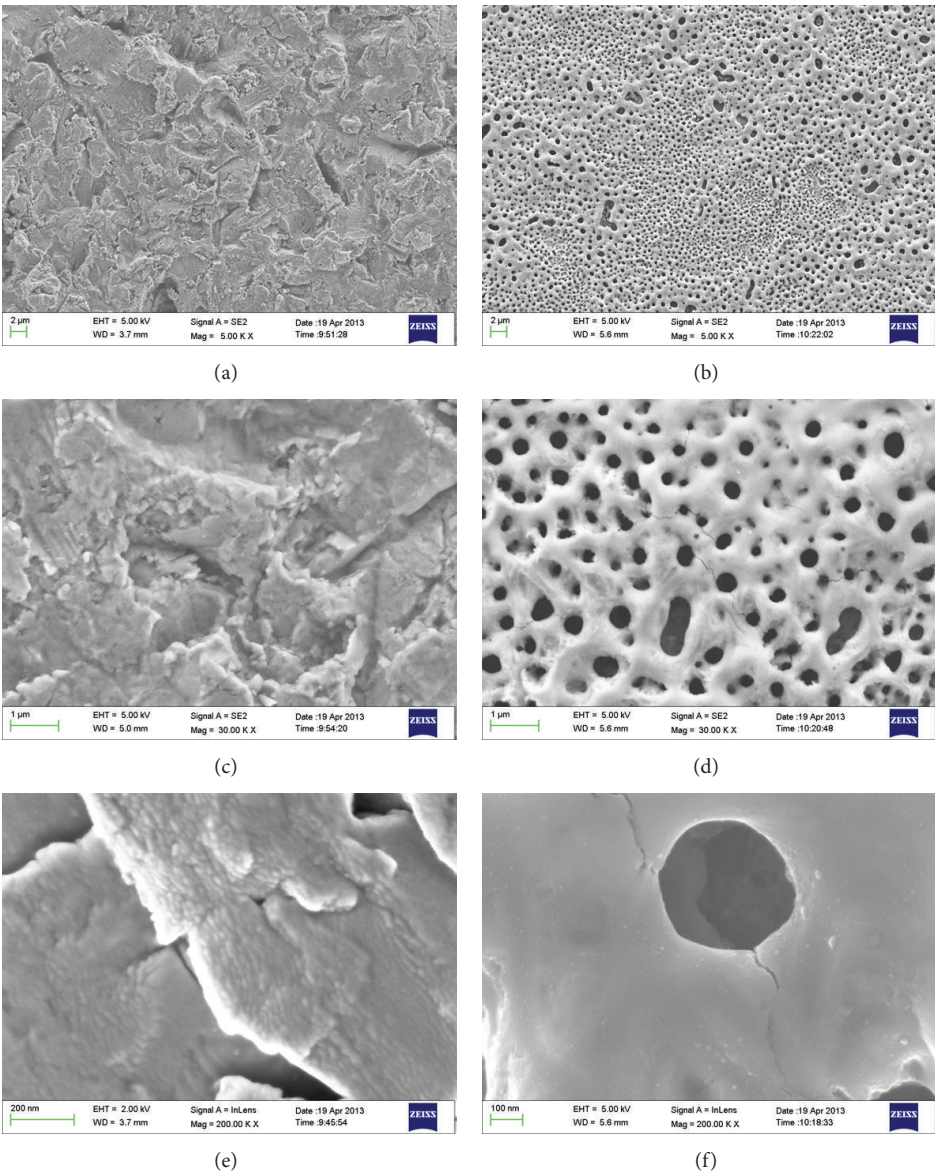


FIGURE 3: SEM images for the discs surfaces show (a) P-I MICRO+NANO and (b) Ospol at 5Kx magnification, (c) P-I MICRO+NANO and (d) Ospol at 30Kx magnification and (e) P-I MICRO+NANO and (f) Ospol at 200Kx magnification.

which was in close contact for both groups. No signs of inflammation or bone resorption were evident.

The mean BIC values for all implant threads and for the top 3 threads of P-I MICRO+NANO and Ospol implants demonstrated no significant differences ( $P = 0.906$ ,  $P = 0.87$ , resp.). When measuring the osteoconductivity of the surfaces,

the two groups did not differ in BA% for both all threads and top 3 threads ( $P = 0.624$ ,  $P = 0.583$ , resp.).

The new bone formation presented that the P-I MICRO+NANO implants which had significantly higher new bone are between all threads and the top 3 threads ( $P = 0.034$ ,  $P = 0.025$ , resp.). Table 5 summarizes all



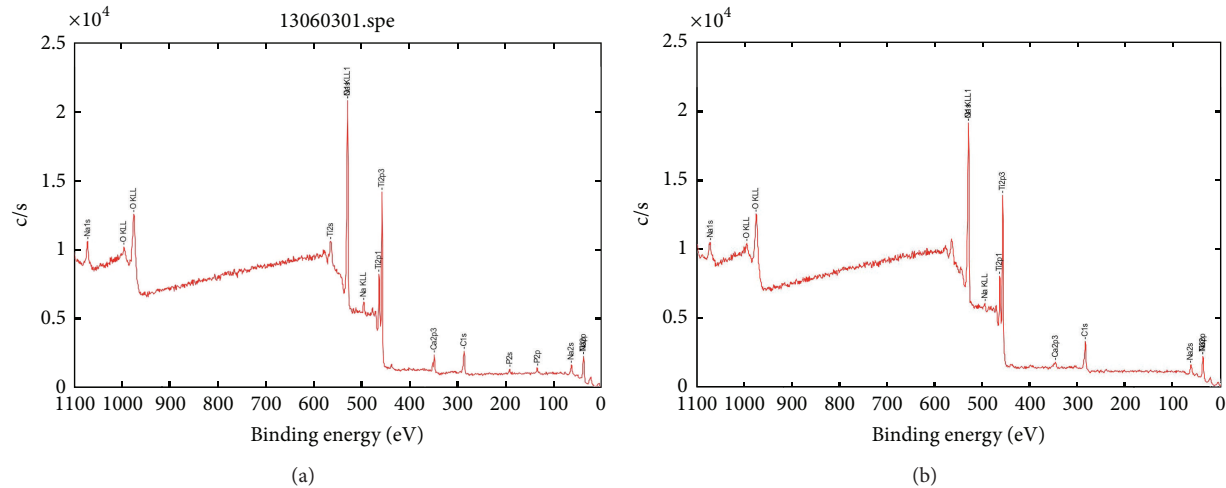


FIGURE 4: XPS survey spectra (a) Ospol and (b) P-I MICRO+NANO implants.

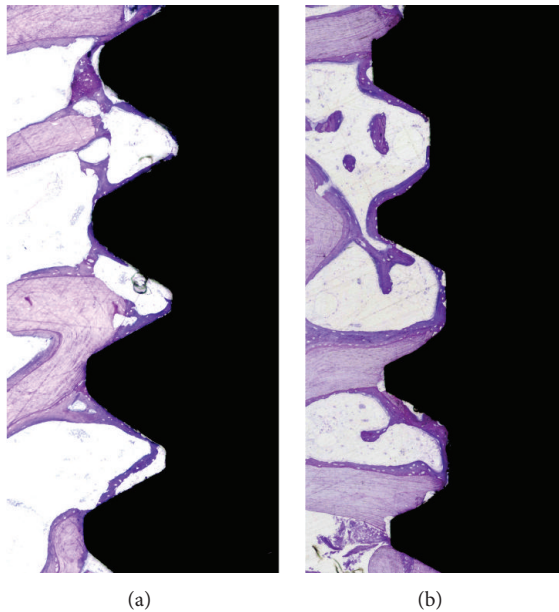


FIGURE 5: Histological observations of P-IMICRO+NANO implant (a) and Ospol implant (b) after 3 weeks (toluidine blue and pyronin staining, original magnification  $\times 10$ ). Cortical old bone is visualized in pale red while the New Bone is visualized in dark red.

histomorphometric measurements. Figure 6 shows a descriptive histological image for new bone formation in P-I MICRO+NANO implants after 3 weeks.

#### 4. Discussion

In the present study, 2 commercially available implants with and without nanostructures were chemically and topographically characterized, and the bone forming properties were evaluated after 3 weeks *in vivo* in a rabbit femur model.

From the SEM observations, the Ospol surface presented an extremely smooth morphology, and nanostructures in size

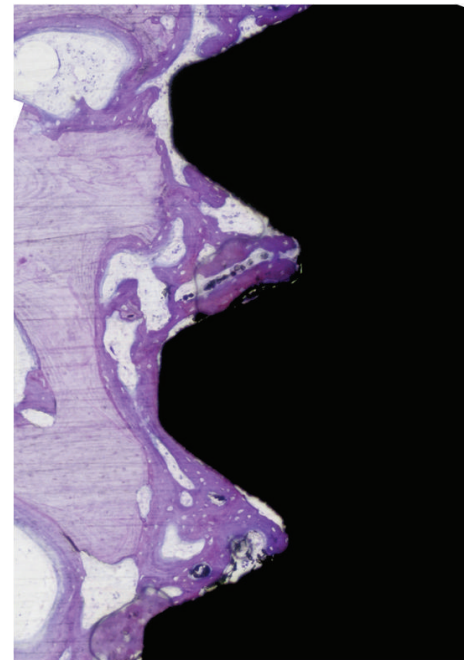


FIGURE 6: Histological observations of new bone formation among the threads of P-I MICRO+NANO implant after 3 weeks (toluidine blue and pyronin staining, original magnification  $\times 10$ ). Cortical old bone is visualized in pale red while the New Bone is visualized in dark red.

of 100 nm or less could not be seen. The anodic oxidation process of the surface showed a typical surface morphology with porous structures of 300–500 nm in size. On the other hand, the SEM images for the P-I MICRO+NANO surface presented a typical surface morphology as a result of the  $\text{TiO}_2$  particle blasting with homogeneous nanostructures of about 20 nm in diameter.

The surface topography in the microlevel confirmed by the interferometer presented unique differences for both surfaces. It was confirmed that both surfaces were smooth

according to the report from Wennerberg and Albrektsson [36]. The average height deviation (Sa) was significantly higher for the P-I MICRO+NANO surface, probably due to the topography created by the surface roughening procedure. However, the density of summits (Sds) and surface enlargement ratio (Sdr) were significantly higher for the Ospot, probably due to the existence of porous structures. The evaluation in the nanolevel confirmed by the AFM presented that the Sds was significantly higher for the P-I MICRO+NANO, which is an indication that the surface has been roughened in the nanoscale. The investigation of the chemical composition of the 2 different surfaces presented that the P-I MICRO+NANO surface presented a high amount of TiO<sub>2</sub> due to the surface blasting procedure and the Ospot surface had large amounts of Ca and P on its surface, probably due to the anodic oxidation procedure performed in baths with these elements.

The histomorphometric measurements presented no significant differences in BIC or in total BA. However, when analyzing the amount of new bone formation represented by deeply stained tissue, significantly higher percentage in favor of the P-I MICRO+NANO implant was shown. The results strongly suggest that both surfaces have abundant osseointegration properties. This was evident in the representative histologic micrographs, where newly formed bone extended from the trabecular bone almost encapsulated the implant surface. The fact that the P-I MICRO+NANO surface presented higher new bone formation within the implant chamber is an indication that the slightly, but significantly, higher microtopography and the presence of the homogeneous nanotopography had positive effects on the bone. Although the Ospot surface underwent a chemical modification incorporating Ca and P into the surface, the histomorphometric results indicated that the chemical modification did not seem to have a strong influence on bone regeneration and the effect of topography was more significant. It is difficult to draw conclusions whether the topography or the chemistry plays a decisive role on bone formation, since some studies suggest the effect of nanotopography to be an influential factor [37, 38] and some others suggest that the effect of chemistry is of most importance [39, 40]. However, in cases where the nanostructure itself is consisting from CaP, it seems that there is a synergistic effect, with the bone mineralization properties being significantly enhanced [32, 41, 42]. It can be said that both chemical and topographical modifications are of great importance for osseointegration; however, their biologic effects may be dependent on numerous factors. More studies are necessary to determine the optimal surface that would present the strongest bone responses, and longer time points are warranted to observe the effect during longer healing periods.

## 5. Conclusion

The results suggested that the effect of homogenous nanostructures presented significantly higher bone formation after 3 weeks *in vivo*, which suggests the effect of nanotopography at early healing periods.

## Conflict of Interests

The authors report no conflicts of interests.

## References

- [1] R. Adell, U. Lekholm, B. Rockler, and P. I. Branemark, "A 15-year study of osseointegrated implants in the treatment of the edentulous jaw," *International Journal of Oral Surgery*, vol. 10, no. 6, pp. 387–416, 1981.
- [2] M. Esposito, J.-M. Hirsch, U. Lekholm, and P. Thomsen, "Biological factors contributing to failures of osseointegrated oral implants. (I). Success criteria and epidemiology," *European Journal of Oral Sciences*, vol. 106, no. 1, pp. 527–551, 1998.
- [3] T. Albrektsson and A. Wennerberg, "Oral implant surfaces: part 1-review focusing on topographic and chemical properties of different surfaces and *in vivo* responses to them," *International Journal of Prosthodontics*, vol. 17, no. 5, pp. 536–543, 2004.
- [4] A. A. Balshe, D. A. Assad, S. E. Eckert, S. Koka, and A. L. Weaver, "A retrospective study of the survival of smooth- and rough-surface dental implants," *The International Journal of Oral & Maxillofacial Implants*, vol. 24, no. 6, pp. 1113–1118, 2009.
- [5] A. Rocci, M. Martignoni, and J. Gottlow, "Immediate loading of Branemark System TiUnite and machined-surface implants in the posterior mandible: a randomized open-ended clinical trial," *Clinical Implant Dentistry and Related Research*, vol. 5, supplement 1, pp. 57–63, 2003.
- [6] A. Wennerberg, T. Albrektsson, B. Andersson, and J. J. Krol, "A histomorphometric and removal torque study of screw-shaped titanium implants with three different surface topographies," *Clinical Oral Implants Research*, vol. 6, no. 1, pp. 24–30, 1995.
- [7] A. Wennerberg, T. Albrektsson, and B. Andersson, "Bone tissue response to commercially pure titanium implants blasted with fine and coarse particles of aluminum oxide," *International Journal of Oral and Maxillofacial Implants*, vol. 11, no. 1, pp. 38–45, 1996.
- [8] A. Wennerberg, T. Albrektsson, and J. Lausmaa, "Torque and histomorphometric evaluation of c.p. titanium screws blasted with 25- and 75-microns-sized particles of Al<sub>2</sub>O<sub>3</sub>," *Journal of Biomedical Materials Research*, vol. 30, no. 2, pp. 251–260, 1996.
- [9] L. Le Guéhennec, A. Soueidan, P. Layrolle, and Y. Amouriq, "Surface treatments of titanium dental implants for rapid osseointegration," *Dental Materials*, vol. 23, no. 7, pp. 844–854, 2007.
- [10] D. Buser, N. Broggini, M. Wieland et al., "Enhanced bone apposition to a chemically modified SLA titanium surface," *Journal of Dental Research*, vol. 83, no. 7, pp. 529–533, 2004.
- [11] D. Buser, T. Nydegger, T. Oxland et al., "Interface shear strength of titanium implants with a sandblasted and acid-etched surface: a biomechanical study in the maxilla of miniature pigs," *Journal of Biomedical Materials Research*, vol. 45, no. 2, pp. 75–83, 1999.
- [12] G. B. Valverde, R. Jimbo, H. S. Teixeira, E. A. Bonfante, M. N. Janal, and P. G. Coelho, "Evaluation of surface roughness as a function of multiple blasting processing variables," *Clinical Oral Implants Research*, vol. 24, no. 2, pp. 238–242, 2013.
- [13] B.-S. Kang, Y.-T. Sul, S.-J. Oh, H.-J. Lee, and T. Albrektsson, "XPS, AES and SEM analysis of recent dental implants," *Acta Biomaterialia*, vol. 5, no. 6, pp. 2222–2229, 2009.
- [14] S. Valencia, C. Gretzer, and L. R. Cooper, "Surface nanofeature effects on titanium-adherent human mesenchymal stem cells,"

- International Journal of Oral and Maxillofacial Implants*, vol. 24, no. 1, pp. 38–46, 2009.
- [15] K. Gotfredsen, A. Wennerberg, C. Johansson, L. T. Skovgaard, and E. Hjorting-Hansen, "Anchorage of TiO<sub>2</sub>-blasted, HA-coated, and machined implants: an experimental study with rabbits," *Journal of Biomedical Materials Research*, vol. 29, no. 10, pp. 1223–1231, 1995.
  - [16] Y. Germanier, S. Tosatti, N. Brogini, M. Textor, and D. Buser, "Enhanced bone apposition around biofunctionalized sandblasted and acid-etched titanium implant surfaces: a histomorphometric study in miniature pigs," *Clinical Oral Implants Research*, vol. 17, no. 3, pp. 251–257, 2006.
  - [17] C. Marin, R. Granato, M. Suzuki, J. N. Gil, A. Piattelli, and P. G. Coelho, "Removal torque and histomorphometric evaluation of bioceramic grit-blasted/acid-etched and dual acid-etched implant surfaces: an experimental study in dogs," *Journal of Periodontology*, vol. 79, no. 10, pp. 1942–1949, 2008.
  - [18] V. C. Mendes, R. Moineddin, and J. E. Davies, "Discrete calcium phosphate nanocrystalline deposition enhances osteoconduction on titanium-based implant surfaces," *Journal of Biomedical Materials Research A*, vol. 90, no. 2, pp. 577–585, 2009.
  - [19] R. Jimbo, T. Sawase, Y. Shibata et al., "Enhanced osseointegration by the chemotactic activity of plasma fibronectin for cellular fibronectin positive cells," *Biomaterials*, vol. 28, no. 24, pp. 3469–3477, 2007.
  - [20] Y.-T. Sul, E.-S. Byon, and Y. Jeong, "Biomechanical measurements of calcium-incorporated oxidized implants in rabbit bone: effect of calcium surface chemistry of a novel implant," *Clinical Implant Dentistry and Related Research*, vol. 6, no. 2, pp. 101–110, 2004.
  - [21] Y.-T. Sul, C. Johansson, A. Wennerberg, L.-R. Cho, B.-S. Chang, and T. Albrektsson, "Optimum surface properties of oxidized implants for reinforcement of osseointegration: surface chemistry, oxide thickness, porosity, roughness, and crystal structure," *International Journal of Oral and Maxillofacial Implants*, vol. 20, no. 3, pp. 349–359, 2005.
  - [22] Y.-T. Sul, J. Jönsson, G.-S. Yoon, and C. Johansson, "Resonance frequency measurements *in vivo* and related surface properties of magnesium-incorporated, micropatterned and magnesium-incorporated TiUnite, Osseotite, SLA and TiObast implants," *Clinical Oral Implants Research*, vol. 20, no. 10, pp. 1146–1155, 2009.
  - [23] Y. T. Sul et al., "Oxidized implants and their influence on the bone response," *Journal of Materials Science*, vol. 12, no. 10–12, pp. 1025–1031, 2001.
  - [24] L. Ferreira, J. M. Karp, L. Nobre, and R. Langer, "New opportunities: the use of nanotechnologies to manipulate and track stem cells," *Cell Stem Cell*, vol. 3, no. 2, pp. 136–146, 2008.
  - [25] T. J. Webster and J. U. Ejiofor, "Increased osteoblast adhesion on nanophase metals: Ti, Ti6Al4V, and CoCrMo," *Biomaterials*, vol. 25, no. 19, pp. 4731–4739, 2004.
  - [26] S. Lavenus, G. Louarn, and P. Layrolle, "Nanotechnology and dental implants," *International Journal of Biomaterials*, vol. 2010, Article ID 915327, 9 pages, 2010.
  - [27] F. Variola, J.-H. Yi, L. Richert, J. D. Wuest, F. Rosei, and A. Nanci, "Tailoring the surface properties of Ti6Al4V by controlled chemical oxidation," *Biomaterials*, vol. 29, no. 10, pp. 1285–1298, 2008.
  - [28] T. J. Webster, R. W. Siegel, and R. Bizios, "Osteoblast adhesion on nanophase ceramics," *Biomaterials*, vol. 20, no. 13, pp. 1221–1227, 1999.
  - [29] T. J. Webster, C. Ergun, R. H. Doremus, R. W. Siegel, and R. Bizios, "Enhanced functions of osteoblasts on nanophase ceramics," *Biomaterials*, vol. 21, no. 17, pp. 1803–1810, 2000.
  - [30] M. J. Dalby, A. Andar, A. Nag et al., "Genomic expression of mesenchymal stem cells to altered nanoscale topographies," *Journal of the Royal Society Interface*, vol. 5, no. 26, pp. 1055–1065, 2008.
  - [31] D. M. D. Ehrenfest, P. G. Coelho, B.-S. Kang, Y.-T. Sul, and T. Albrektsson, "Classification of osseointegrated implant surfaces: materials, chemistry and topography," *Trends in Biotechnology*, vol. 28, no. 4, pp. 198–206, 2010.
  - [32] R. Jimbo, J. Sotres, C. Johansson, K. Breeding, F. Currie, and A. Wennerberg, "The biological response to three different nanostructures applied on smooth implant surfaces," *Clinical Oral Implants Research*, vol. 23, no. 6, pp. 706–712, 2012.
  - [33] L. M. Bjursten, L. Rasmusson, S. Oh, G. C. Smith, K. S. Brammer, and S. Jin, "Titanium dioxide nanotubes enhance bone bonding *in vivo*," *Journal of Biomedical Materials Research A*, vol. 92, no. 3, pp. 1218–1224, 2010.
  - [34] A. Wennerberg and T. Albrektsson, "Suggested guidelines for the topographic evaluation of implant surfaces," *International Journal of Oral and Maxillofacial Implants*, vol. 15, no. 3, pp. 331–344, 2000.
  - [35] K. Donath and G. Breuner, "A method for the study of undecalcified bones and teeth with attached soft tissues. The Sage-Schliff (sawing and grinding) technique," *Journal of Oral Pathology*, vol. 11, no. 4, pp. 318–326, 1982.
  - [36] A. Wennerberg and T. Albrektsson, "On implant surfaces: a review of current knowledge and opinions," *The International Journal of Oral & Maxillofacial Implants*, vol. 25, no. 1, pp. 63–74, 2010.
  - [37] L. Meirelles, A. Arvidsson, T. Albrektsson, and A. Wennerberg, "Increased bone formation to unstable nano rough titanium implants," *Clinical Oral Implants Research*, vol. 18, no. 3, pp. 326–332, 2007.
  - [38] J. Karlsson, R. Jimbo, H. M. Fathali et al., "In vivo biomechanical stability of osseointegrating mesoporous TiO<sub>2</sub> implants," *Acta Biomater*, vol. 8, no. 12, pp. 4438–4446, 2012.
  - [39] Y.-T. Sul, D. H. Kwon, B.-S. Kang, S.-J. Oh, and C. Johansson, "Experimental evidence for interfacial biochemical bonding in osseointegrated titanium implants," *Clinical Oral Implants Research*, vol. 24, supplement A100, pp. 8–19, 2011.
  - [40] Y.-T. Sul, C. Johansson, and T. Albrektsson, "A novel *in vivo* method for quantifying the interfacial biochemical bond strength of bone implants," *Journal of the Royal Society Interface*, vol. 7, no. 42, pp. 81–90, 2009.
  - [41] R. Jimbo, P. G. Coelho, M. Bryington et al., "Nano hydroxyapatite-coated implants improve bone nanomechanical properties," *Journal of Dental Research*, vol. 91, no. 12, pp. 1172–1177, 2012.
  - [42] R. Jimbo, P. G. Coelho, S. Vandeweghe et al., "Histological and three-dimensional evaluation of osseointegration to nanostructured calcium phosphate-coated implants," *Acta Biomaterialia*, vol. 7, no. 12, pp. 4229–4234, 2011.

## Research Article

# Silver Nanoparticles and Mitochondrial Interaction

**Erierto Bressan,<sup>1</sup> Letizia Ferroni,<sup>2</sup> Chiara Gardin,<sup>2</sup> Chiara Rigo,<sup>3</sup> Michele Stocchero,<sup>1</sup> Vincenzo Vindigni,<sup>1</sup> Warren Cairns,<sup>3</sup> and Barbara Zavan<sup>2</sup>**

<sup>1</sup> Department of Biomedical Sciences, University of Padova, Via G. Colombo 3, 35100 Padova, Italy

<sup>2</sup> Department of Neurosciences, University of Padova, Via Venezia 90, 35100 Padova, Italy

<sup>3</sup> CNR-IDPA c/o Department of Environmental Sciences Informatics and Statistics, Università Ca' Foscari, Dorsoduro 2137, 30123 Venezia, Italy

Correspondence should be addressed to Barbara Zavan; [barbara.zavan@unipd.it](mailto:barbara.zavan@unipd.it)

Received 14 May 2013; Revised 10 July 2013; Accepted 31 July 2013

Academic Editor: Ryo Jimbo

Copyright © 2013 Erierto Bressan et al. This is an open access article distributed under the Creative Commons Attribution License, which permits unrestricted use, distribution, and reproduction in any medium, provided the original work is properly cited.

Nanotechnology has gone through a period of rapid growth, thus leading to the constant increase in the application of engineered nanomaterials in daily life. Several different types of nanoparticles have been engineered to be employed in a wide array of applications due to their high surface to volume ratio that leads to unique physical and chemical properties. So far, silver nanoparticles (AgNps) have been used in many more different medical devices than any other nanomaterial, mainly due to their antimicrobial properties. Despite the promising advantages posed by using AgNps in medical applications, the possible health effects associated with the inevitable human exposure to AgNps have raised concerns as to their use since a clear understanding of their specific interaction with biological systems has not been attained yet. In light of such consideration, aim of the present work is the morphological analysis of the intracellular behavior of AgNps with a diameter of 10 nm, with a special attention to their interaction with mitochondria.

## 1. Introduction

Antibacterial properties of silver ions are well known. Indeed, silver has been used since time immemorial in different chemical forms to treat burns, wounds, and several different infections caused by pathogenic bacteria. Interestingly, for thousands of years, silver and silver ions have been used for their bactericidal properties [1, 2], which include

- (1) multilevel antibacterial effects that considerably reduce the chances of developing resistance since this effect of silver is thought to be due to blockage of respiratory enzyme pathways and alteration of microbial DNA and the cell wall [3, 4];
- (2) effectiveness against multidrug-resistant organisms [5, 6];
- (3) low systemic toxicity [7, 8].

Over the past decade, a variety of advanced silver-based medical devices have been developed with considerable variations in the structure, composition, and silver content. In recent years, nanotechnology has provided the means of producing pure silver nanoparticles, markedly increasing the rate of silver ion release and its antimicrobial activity as well.

The use of oral implants in the rehabilitation of partially and fully edentulous patients is widely accepted even though failures do occur [9]. The chance for implants to integrate can for example be jeopardised by the intraoral presence of bacteria and concomitant inflammatory reactions. The longevity of osseointegrated implants can be compromised by occlusal overload and/or plaque-induced peri-implantitis, depending on the implant geometry and surface characteristics. Animal studies, cross-sectional and longitudinal observations in man, and association studies indicate that peri-implantitis is characterised by a microbiota comparable to that of periodontitis (high proportion of anaerobic



Gram-negative rods, motile organisms, and spirochetes), but this does not necessarily prove a causal relationship [10]. However, in order to prevent such a bacterial shift, the following measures can be considered: periodontal health in the remaining dentition (to prevent bacterial translocation), the avoidance of deepened peri-implant pockets, and the use of a relatively smooth abutment and implant surface. Finally, periodontitis enhancing factors such as smoking and poor oral hygiene also increase the risk for peri-implantitis [11].

The oral cavity is populated by a variety of microorganisms. The microbial communities in the oral cavity are polymicrobial and exist primarily as biofilms [12]. These biofilms can be responsible for several local diseases, including periodontal and peri-implant diseases, which can lead to the loss of teeth or implants, respectively. The potential of silver nanoparticles (AgNPs) to reduce bacterial adhesion to dental implant surfaces and to prevent biofilm formation has been investigated by many authors [13, 14] with a view to reducing the risk of peri-implant infections. Another interesting application of Ag NPs in dentistry pertains the structural and surface modification of bone grafts and membranes with a view to preventing the risk of contamination and associated infection that are common when bone augmentation techniques such as guided bone regeneration (GBR) and guided tissue regeneration (GTR) are used [15–19].

Despite the widespread use of Ag NPs, a lack of information on their biological effects on human cells and environments still exists. Some authors have investigated the potential toxicity of Ag NPs in different cell systems, including bacteria and mammalian cells. Such studies have attributed the cytotoxicity of Ag NPs to several possible mechanisms, including the dissolving or release of Ag ions from the nanoparticles, the disruption of cell membrane integrity, oxidative stress, protein or DNA binding and damage, the generation of reactive oxygen species, and apoptotic cell death. The toxic mechanism seems likely to depend on the nanoparticles' properties too, for example surface area, size and shape, capping agent, surface charge, particle purity, structural distortion, and the bioavailability of the individual particles. To this view, in previous works, our group compared the silver structure and content of several Ag dressing based products, focusing main attention on Acticoat [20, 21].

Acticoat is a nanocrystalline silver dressing composed of two layers of silver-coated high-density polyethylene, enclosing a rayon/polyester core of apertured nonwoven fabric. The elements that compose Acticoat are welded together ultrasonically. When moistened with water, microscopic nanocrystals of metallic silver are released from the dressing onto the wound bed. The silver has an antimicrobial action which destroys a range of bacteria, including both Gram-positive and Gram-negative bacteria [22].

SEM images of this product showed that the polyethylene fibers are coated with Ag. The coating appears homogeneous and uniform. The size of the Ag nanocrystals was determined at a magnification of 50,000; the images show that the particle size ranges from 200 to 450 nm.

Moreover, its cytotoxicity was tested *in vitro* and *in vivo* on human. In the present work the studies are carried on

focusing on the intracellular behavior of Ag nanoparticles released from acticoat during a wound dressing.

## 2. Material and Methods

**2.1. Human Skin Samples.** Patients were eligible for the study if recruited <24 h postburn injury and were affected by partial-thickness burns. Patients were excluded if they were affected by full thickness burns or had a compromised immune system or were known to be hypersensitive to silver and its compounds.

Patients were also excluded in case of comorbidity (e.g., diabetes and cardiac or renal disease), chemical or electrical burns, multiple trauma, or were aged <5 or >60. Skin biopsies were obtained from a set of eligible patients who gave consent for taking biopsy materials for scientific purposes, and the study was performed in compliance with the Declaration of Helsinki ethical guidelines.

Biopsies were collected by using punches of 4 mm inner diameter 7 mm depth. After seven days of treatment at dressing removal, two more duplicates were taken, one from the healed area and another from an unhealed zone. After 10 more days of treatment with a new dressing, another duplicate sample was taken from the newly healed area.

**2.2. TEM.** The samples were preserved in a 2.5% glutaraldehyde/0.1 M sodium cacodylate buffer overnight at 4°C. The samples were then treated with 1% OsO<sub>4</sub>/0.1 M sodium cacodylate buffer and dehydrated using ethanol solutions of increasing concentrations before embedding in EPON epoxy resins. Ultrathin sections (ultramicrotome, LKB, Stockholm, Sweden) were obtained and treated with 1% uranyl acetate and 1% lead citrate. The samples were analyzed by TEM (Electronic Microscopy Service, Department of Biology, University of Padova, Padua, Italy) using a Tecnai G12 electron microscope (FEI, acceleration voltage 100 kV). The image acquisition system consisted of a video camera, TIETZ (Tietz Video and Image Processing Systems GmbH, Gauting, Germany), and the TIA FEI Imaging Software (FEI Company, Hillsboro, OR, USA).

**2.3. Cell Cultures.** Human dermal fibroblasts were prepared according to a modified version of the Rheinwald and Green protocol. After epithelial sheet dispass removal, the dermis was cut into small pieces (2–3 mm<sup>2</sup>), and fibroblasts were isolated by sequential digestion with 0.25% w/v trypsin for 20 min and 0.25% w/v collagenase for 4 h. These cells were then cultured with Dulbecco's Modified Eagle Medium (DMEM), (Lonza S.r.l., Milano, Italy) supplemented with 10% fetal bovine serum (FBS) (Bidachem S.p.A., Milano, Italy) and 100 units/mL penicillin and 100 µg/mL streptomycin to form complete DMEM (cDMEM). The medium was changed twice a week, and the cells were harvested by trypsin treatment. After detachment from culture plates, fibroblasts were cultured in 3D collagen-based scaffolds (MatriDerm, Dr. Suwelack Skin and Health Care AG, Billerbeck, Germany) at a density of 10<sup>5</sup> cells/cm<sup>2</sup>, obtaining a reconstructed dermal-like tissue *in vitro*. Cells were grown in the 3D scaffold for 10



days in 800  $\mu\text{L}$  of cDMEM. The Ag NP-based dressing was applied above the 3D cell cultures.

**2.4. MTT Assay.** To determine the kinetics of cell growth with or without Ag NPs, the MTT-based (methyl-thiazolyl-tetrazolium) cytotoxicity assay was performed according to the method of Denizot and Lang with minor modifications. This colorimetric assay is an indirect method for assessing cell growth and proliferation. MTT gives a yellowish aqueous solution, which, on reduction with dehydrogenases or reducing agents present in metabolically active cells, yields a violet-blue water insoluble dye compound, formazan. The lipid soluble formazan is extracted with organic solvents and quantified spectrophotometrically. The amount of MTT formazan produced is directly proportional to the metabolic activity of cells. After harvesting the culture medium, the cells were incubated for 3 h at  $37^{\circ}\text{C}$  in 1 mL of 0.5 mg/mL MTT solution prepared in phosphate buffer saline solution (PBS). After removal of the MTT solution by pipette, 0.5 mL of 10% dimethyl sulfoxide in isopropanol (iDMSO) was added to extract the formazan in the samples for 30 min at  $37^{\circ}\text{C}$ . For each sample, absorbance values at 570 nm were recorded in duplicate on 200  $\mu\text{L}$  aliquots deposited in microwell plates using a multilabel plate reader (Victor 3 Perkin Elmer, Milano, Italy). The mitochondrial functionality in the Ag NP-treated cells is calculated as the ratio between the absorbance at 570 nm of the treated sample and the absorbance of a control sample expressed as a percentage.

**2.5. Morphological Analysis.** Concurrently with the MTT assay, morphological analyses were carried out on the duplicate samples. After removing the Ag NP-based dressing and the culture medium, the remaining dermal-like tissue was embedded in Optimal Cutting Temperature (OCT) compound, frozen in liquid nitrogen and preserved at  $-80^{\circ}\text{C}$  until cutting. Tissue sections ( $>7\ \mu\text{m}$  thickness) were obtained using a cryostat (CM1950, Leica, Milano, Italy) and deposited onto gelatin-coated glass slides. They were fixed with absolute acetone for 10 min at room temperature and cryopreserved at  $-20^{\circ}\text{C}$  until use. In order to visualize the cell distribution inside the scaffold and to investigate the possibility of nuclear fragmentation, the fibroblasts nuclei were stained with H33342 fluorochrome (Sigma Aldrich, Milano, Italy, final concentration of 2  $\mu\text{g}/\text{mL}$ ). The samples were observed using a Zeiss Axioplan fluorescence microscope equipped with a digital camera (DC500, Leica, Milano, Italy).

In order to quantify the number of live cells and highlight the presence of apoptotic cells, a parallel set of *in vitro* experiments were carried out. Hoechst H33342 dye was added to the 3D dermal-like cell culture simultaneously with YO-PRO-1 iodide dye (excitation wavelength 491 nm/emission wavelength 509 nm, Molecular Probes). Hoechst H33342 dye stains the nuclei in the whole population of cells, while YO-PRO-1 stains specifically the apoptotic cells. YO-PRO-1 is a green fluorescent probe, which can enter cells once their plasma membrane has reached a certain degree of permeability.

The cell membrane during apoptosis becomes slightly permeable and YO-PRO-1 can freely enter the cell and bind

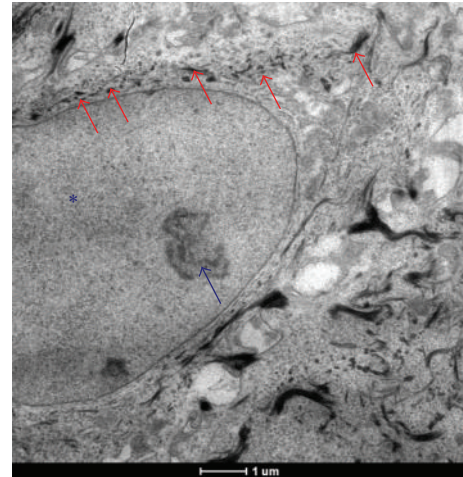


FIGURE 1: TEM images of a fibroblast present in a healed skin sample treated with AgNP based medical devices. The cells are healthy as the right morphological features show: integrity of plasma membrane, nuclear integrity (blue\*), and active nucleolus (blue arrow).

to its nucleic acids, enhancing its fluorescence intensity. The number of different cells was counted, and live cells are calculated as the difference between the number of cells stained with Hoechst H33342 and the number of apoptotic cells stained with YO-PRO-1. Immediately after the removal of the Ag NP-based dressing from the 3D cell cultures, Hoechst 33342 and YO-PRO-1 were added to the cell cultures. The cells were incubated at  $37^{\circ}\text{C}$  for one hour, and then, the culture multiwell plate containing the cells was transferred to a confocal laser scanning microscope to monitor YO-PRO-1 and Hoechst fluorescence.

A fluorescence confocal laser scanning microscope (Axiovert 100M, Zeiss, Germany) with a  $10^{\circ}$  magnification objective was used for the detection of Hoechst H33342 and YO-PRO-1 stained cells. The fluorescent dye, YO-PRO-1, was excited with a 25 mW Argon laser at 488 nm. Emission was recorded above 510 nm. The Hoechst H33342 fluorescence was detected at 460 nm after excitation at 346 nm. The microscope was equipped with a motorized stage, and the LSM 510 (Zeiss) software enabled memorization of stage positions. For each sample, images were taken at the preset stage positions at various depths.

**2.6. ROS Measurements.** The OxiSelect ROS Assay Kit is a cell-based assay for measuring hydroxyl, peroxyl, and other reactive oxygen species activity within a cell. The assay employs the cell-permeable fluorogenic probe DCFH-DA, which diffuses into cells and is deacetylated by cellular esterases into the nonfluorescent DCFH (Figure 1). In the presence of ROS, DCFH is rapidly oxidized to highly fluorescent DCF. Fluorescence is read on a standard fluorometric plate reader.

### 3. Results and Discussion

fibroblast present in the deeper layer of burned skin are able to uptake AgNps (Figure 1, red arrows). The cells are

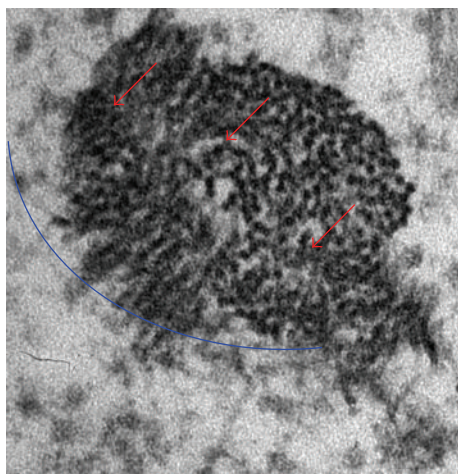


FIGURE 2: TEM images of a fibroblast present in a healed skin sample treated with AgNP based medical devices. Nanoparticles taking up by endocytosis. AgNPs in normal human dermal fibroblasts take up AgNPs (red arrows) by endocytosis (blue arc).

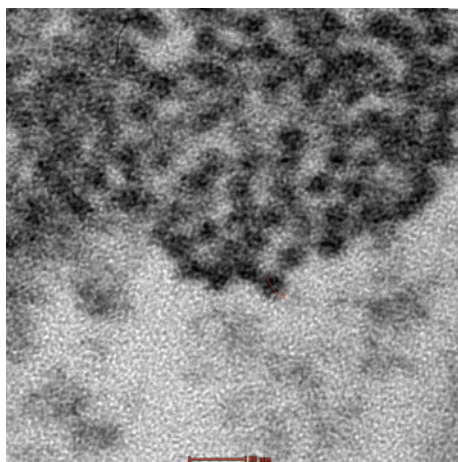


FIGURE 3: TEM images of AgNPs (red arrows) in cytoplasmic space of fibroblast present in a healed skin sample treated with AgNP based medical devices. The diameter of particles released from the medical devices are of 20 nm, indicating that their aggregates are able to enter the cells by endocytosis.

healthy as the right morphological features show: integrity of plasma membrane, nuclear integrity (blue\*), and active nucleolus (blue arrow). All nanoparticles are taken up by mammalian cells by such mechanisms as pinocytosis, endocytosis dependent on caveolae and lipid raft composition, clathrin-dependent endocytosis and phagocytosis [10], endocytosis {Endo (within) cytosol (cell)}, is a process in which a substance gains entry into a cell without passing through the cell membrane. This process is subdivided into three different types: pinocytosis, phagocytosis, receptor mediated endocytosis. Receptor mediated endocytosis is an endocytotic mechanism in which specific molecules are ingested into the cell. The specificity results from a receptor-ligand interaction. Receptors on the plasma membrane of the target tissue will

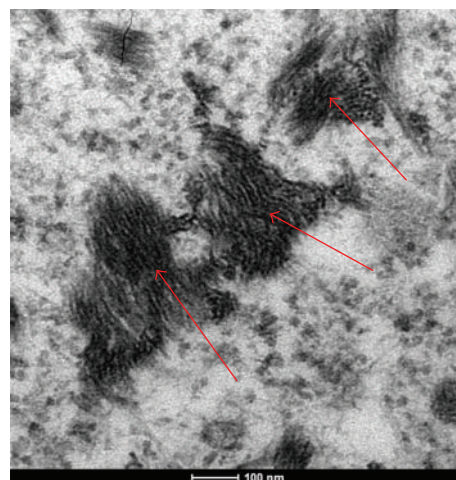


FIGURE 4: TEM images of AgNPs (red arrows) in cytoplasmic space of fibroblast present in a healed skin sample treated with AgNP based medical devices.

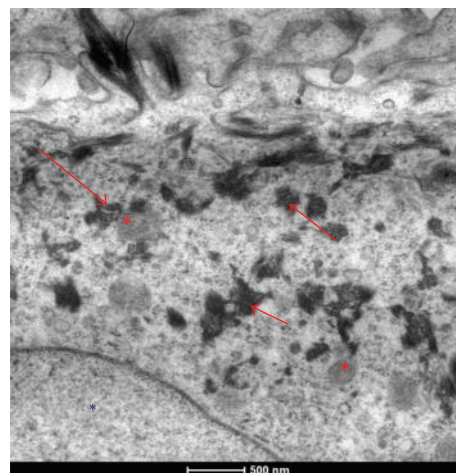


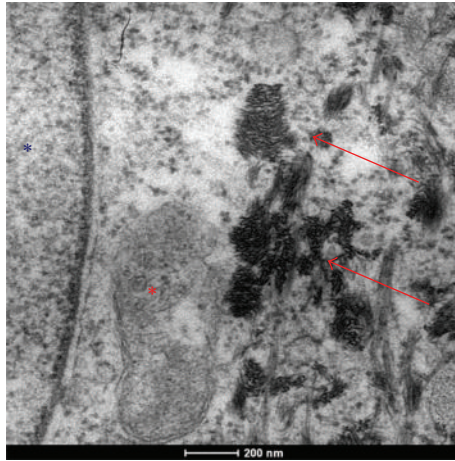
FIGURE 5: TEM images of AgNPs (red arrows) in cytoplasmic space of fibroblast present in a healed skin sample treated with AgNP based medical devices. AgNP are closed to the mitochondria (red\*); nuclei is indicated by blue\*.

specifically bind to ligands on the outside of the cell. An endocytotic process occurs, and the ligand is ingested. In each case, endocytosis results in the formation of an intracellular vesicle by virtue of the invagination of the plasma membrane and membrane fusion.

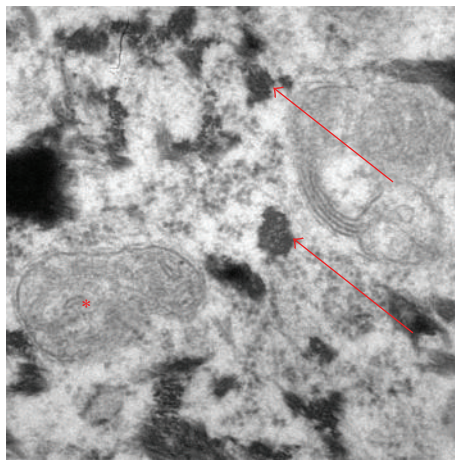
AgNPs are no exception in this respect; as shown in Figure 2, indeed, normal human dermal fibroblasts take up AgNPs (red arrows) by endocytosis (blue arc). As well reported in Figure 3 the diameter of particles released from the medical devices is of 20 nm, (note: a fibroblast size is about 100  $\mu$ m) indicating that their aggregates are able to enter into the cells by endocytosis.

As regards intracellular localization of AgNPs, their ability to form aggregates of about 200 nm (Figure 4, red arrows) was confirmed. They are absent from the cell nucleus, endoplasmic reticulum, or Golgi complex (Figure 5). They





(a)



(b)

FIGURE 6: TEM images of AgNps (red arrows) in cytoplasmic space of fibroblast present in a healed skin sample treated with AgNps based Medical devices. AgNP are closed to the mitochondria (red\*); and not inside the mitochondria and inside the nuclei (indicated by blue\*).

also formed agglomerates in the perinuclear region (Figure 5, red arrows). The transmission electron microscopy (TEM) analysis indicated the absence of AgNps (Figures 5 and 6 red arrows) inside the mitochondria (Figures 5 and 6 red\*) and nucleus (Figure 5 blue\*). AgNps are closed to the outer membrane of the mitochondria as it is well shown in Figure 7 red arrows (mitochondria red\*). Mitochondria are organized in the perinuclear zone of the cytoplasm (Figure 8, square barked red), recruiting the larger quantity of AgNps (Figure 8 red arrows) present in the cytoplasm.

In these conditions, mitochondria are small (Figure 8 red\*), round and in high number.

To investigate if Ag NPs could negatively affect cell survival, we evaluated their toxicity on fibroblasts *in vitro*. A collagen-based scaffold was employed as a support for a 3D cell culture of fibroblasts to obtain a dermal-like tissue. Morphological analyses were carried out to investigate nuclei morphology and cellular distribution within the scaffold. As

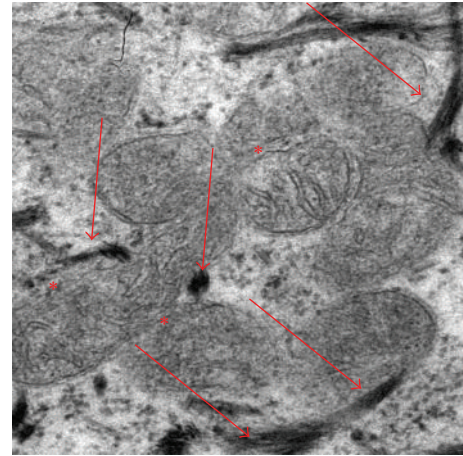


FIGURE 7: TEM images of AgNps (red arrows) in cytoplasmic space of fibroblast present in a healed skin sample treated with AgNP based Medical devices. AgNP (red arrows) are closed to the mitochondria (red\*).

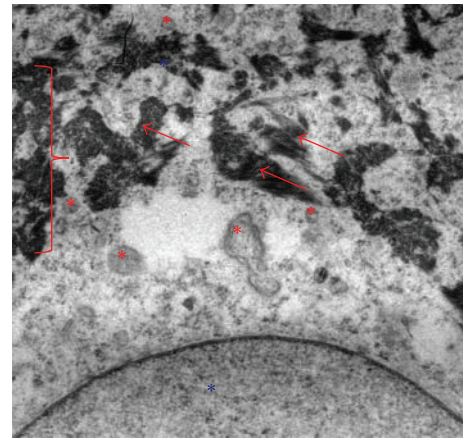


FIGURE 8: TEM images of AgNps (red arrows) in cytoplasmic space of fibroblast present in a healed skin sample treated with AgNP based Medical devices. AgNps are closed to the outer membrane of the mitochondria that are organized in the perinuclear zone of the cytoplasm (square barked red), recruiting the larger quantity of AgNps present in the cytoplasm.

reported in Figure 9(a) the dermal-like tissue appears as a multilayer of cells, where the fibroblasts are able to proliferate and fill the scaffolds during the course of the experiments. No signs of apoptosis were detected. The similar distribution of cells was seen in the Ag NP-treated samples (Figure 9(b)). Interestingly, despite the reduced mitochondrial functionality observed, the nuclei are still present and appear to be undamaged. There was no observable presence of apoptotic bodies or nuclear fragmentation.

A quantitative comparison of the number of live cells in the treated and untreated 3D cell cultures is reported in Figure 10(a). The results show that the number of live cells increased with time at the same rate in both samples. The YO-PRO-1 assay showed that there were no apoptotic cells visible in the sample treated with Ag NPs.

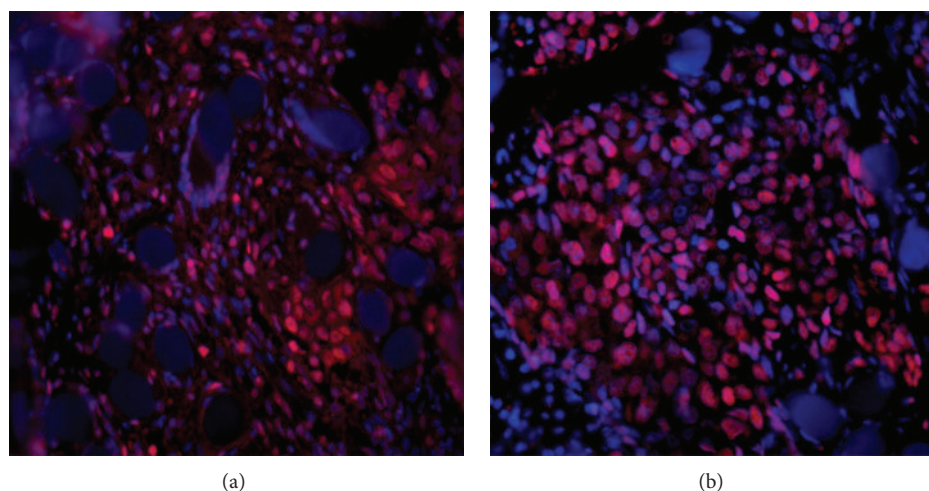


FIGURE 9: Dermal-like tissue reconstructed *in vitro*. Cells, visible thanks to the red staining of the nuclei, can be seen inside the collagen-based scaffold and appear to be organized in layers. (a) Un-treated control after 9 days from the beginning of the experiments; (b) treated control at nine days.

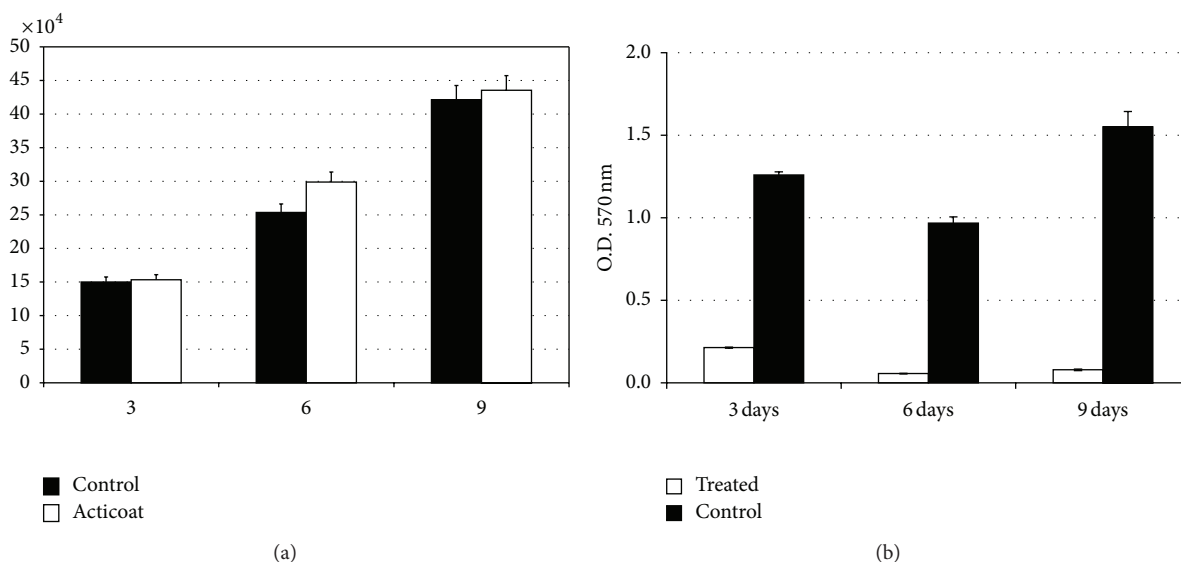


FIGURE 10: (a) Progression of cell growth in time in a 3D dermal-like tissue after Ag NP treatment (white) and in the control sample (black), mean value  $\pm$  SD samples versus time. The count of the live cells in the sample is obtained as the sum of the live cells at various depths at each position. (b) MTT test for mitochondrial activity in a 3D dermal-like tissue after Ag NPs treatment (white) and in the control sample (black) mean value  $\pm$  SD samples versus time. As it is well evident, when silver nanoparticles are present, no mitochondrial activity is detectable.

At three, six, and nine days, MTT assays were carried out to assess the mitochondrial function in cells treated with Ag NPs. Cytotoxicity *in vitro* is usually estimated with the use of colorimetric tests; their principle is the reduction of tetrazolium salts, MTT (3-(4,5-dimethylthiazol-2-yl)-2,5-diphenyltetrazolium bromide) to formazan. The reduction is carried out by a mitochondrial reductase and is an indirect measure of cell population viability.

As reported in Figure 10(b), a time-dependent decrease in metabolic activity was observed in the cells treated with the Ag NP-based dressing. This confirms the ability of AgNPs to impair mitochondrial function. Examples of MTT test application for AgNPs cytotoxicity (ROS) are present in every

cell, being produced by the mitochondrial and cytoplasmic oxidation processes. Under environmental stress, the cell reacts by increased ROS generation, and this leads to imbalance between ROS generation and their neutralization by antioxidative enzymes and low molecular weight antioxidants, among others by glutathione. This disturbance of the redox equilibrium is defined as oxidative stress. Under conditions of oxidative stress the cell accumulates ROS, and the antioxidative response that follows involves modifications in signaling pathways.

In order to test if this damage could be correlated to a ROS production we tested ROS generations. As reported in Figure 11 there is a ROS production in presence of AgNPs.

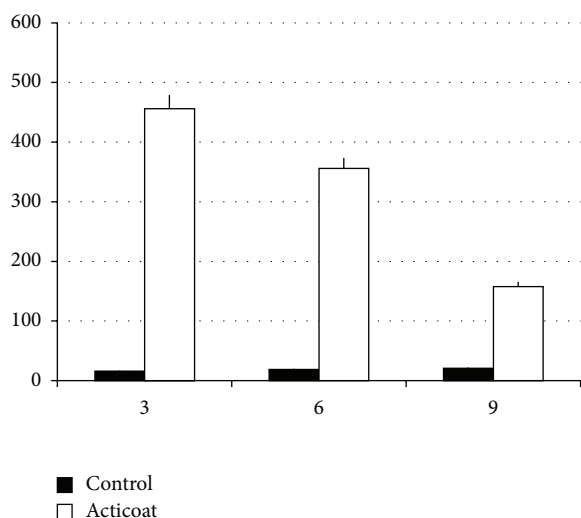


FIGURE 11: The ROS measurement in dermal-like tissue reconstructed *in vitro* with (white) and without AgNPs (black) treatment. As it is well evident, when silver nanoparticles are present, ROS activity is detectable.

This production decreases in time, according to the ability of the mitochondria to capture AgNPs.

#### 4. Conclusions

ROS increase due to nanoparticle treatment has been shown to be the key factor in the biological effects *in vivo* and *in vitro* [23–25]. From our TEM microphotographs it can be judged that AgNPs accumulate outside the mitochondria. It is possible that this is the direct cause of mitochondrial damage and the disturbed function of the respiratory chain resulting in ROS generation and oxidative stress. No AgNPs were detected inside the nucleus, and no fragmented nuclei were observed. Despite the presence of AgNPs inside the cytoplasm, the nuclear membrane is intact and is round in shape. The nucleolus visible confirms that the chromatin is not condensed, but that it has a structure that allows transcription to proceed. We hypothesize that once the AgNPs have been released into the cytoplasm, they generate ROS.

We speculate, then, that mitochondria are moved around the nucleus to act as a physical-chemical barrier to prevent ROS and AgNPs from reaching the nuclear membrane. If the mitochondrial membrane breaks down due to the action of ROS, antioxidative enzymes, such as mitochondrial superoxide dismutase (mtSOD), catalase, glutathione peroxidase, and thioredoxin peroxidase [26, 27], are released from the mitochondria into the cytoplasm to quench the ROS.

#### Conflict of Interests

The authors declare that there is no conflict of interests.

#### References

- [1] S. Sivoilella, E. Stellini, G. Brunello et al., “Silver nanoparticles in alveolar bone surgery devices and toxicity of silver nanoparticles in alveolar bone surgery devices,” *Journal of Nanomaterials*, vol. 2012, Article ID 975842, 12 pages, 2012.
- [2] R. Cortivo, V. Vindigni, L. Iacobellis, G. Abatangelo, P. Pinton, and B. Zavan, “Nanoscale particle therapies for wounds and ulcers,” *Nanomedicine*, vol. 5, no. 4, pp. 641–656, 2010.
- [3] N. Silvestry-Rodriguez, E. E. Sicairos-Ruelas, C. P. Gerba, and K. R. Bright, “Silver as a disinfectant,” *Reviews of Environmental Contamination and Toxicology*, vol. 191, pp. 23–45, 2007.
- [4] A. Melaiye and W. J. Youngs, “Silver and its application as an antimicrobial agent,” *Expert Opinion on Therapeutic Patents*, vol. 15, no. 2, pp. 125–130, 2005.
- [5] B. S. Atiyeh, M. Costagliola, S. N. Hayek, and S. A. Dibo, “Effect of silver on burn wound infection control and healing: review of the literature,” *Burns*, vol. 33, no. 2, pp. 139–148, 2007.
- [6] J. Jain, S. Arora, J. M. Rajwade, P. Omray, S. Khandelwal, and K. M. Paknikar, “Silver nanoparticles in therapeutics: development of an antimicrobial gel formulation for topical use,” *Molecular Pharmaceutics*, vol. 6, no. 5, pp. 1388–1401, 2009.
- [7] L. B. Rice, “The clinical consequences of antimicrobial resistance,” *Current Opinion in Microbiology*, vol. 12, no. 5, pp. 476–481, 2009.
- [8] I. Tocco, B. Zavan, F. Bassetto, and V. Vindigni, “Nanotechnology-based therapies for skin wound regeneration,” *Journal of Nanomaterials*, vol. 2012, Article ID 714134, 11 pages, 2012.
- [9] M. Quirynen, M. de Soete, and D. van Steenberghe, “Infectious risks for oral implants: a review of the literature,” *Clinical Oral Implants Research*, vol. 13, no. 1, pp. 1–19, 2002.
- [10] M. Esposito, H. V. Worthington, V. Loli, P. Coulthard, and M. G. Grusovin, “Interventions for replacing missing teeth: antibiotics at dental implant placement to prevent complications,” *Cochrane Database of Systematic Reviews*, vol. 7, Article ID CD004152, 2010.
- [11] D. Kinane and P. Bouchard, “Periodontal diseases and health: consensus Report of the Sixth European Workshop on Periodontology,” *Journal of Clinical Periodontology*, vol. 35, no. 8, pp. 333–337, 2008.
- [12] G. Chiara, F. Letizia, F. Lorenzo et al., “Nanostructured biomaterials for tissue engineered bone tissue reconstruction,” *International Journal of Molecular Sciences*, vol. 13, no. 1, pp. 737–757, 2012.
- [13] R. P. Allaker, “Critical review in oral biology & medicine: the use of nanoparticles to control oral biofilm formation,” *Journal of Dental Research*, vol. 89, no. 11, pp. 1175–1186, 2010.
- [14] D. R. Monteiro, L. F. Gorup, A. S. Takamiya, A. C. Ruvollo-Filho, E. R. D. Camargo, and D. B. Barbosa, “The growing importance of materials that prevent microbial adhesion: antimicrobial effect of medical devices containing silver,” *International Journal of Antimicrobial Agents*, vol. 34, no. 2, pp. 103–110, 2009.
- [15] X. Wu, J. Li, L. Wang, D. Huang, Y. Zuo, and Y. Li, “The release properties of silver ions from Ag-nHA/TiO<sub>2</sub>/PA66 antimicrobial composite scaffolds,” *Biomedical Materials*, vol. 5, no. 4, Article ID 044105, 2010.
- [16] J. Li, Y. Zuo, Y. Man et al., “Fabrication and biocompatibility of an antimicrobial composite membrane with an asymmetric porous structure,” *Journal of Biomaterials Science, Polymer Edition*, vol. 23, no. 1–4, pp. 81–96, 2012.
- [17] O. D. Schneider, D. Mohn, and R. Fuhrer, “Biocompatibility and bone formation of flexible, cotton wool-like PLGA/calcium



- phosphate nanocomposites in sheep,” *The Open Orthopaedics Journal*, vol. 5, pp. 63–71, 2011.
- [18] J. Ye, Q. Yao, A. Mo et al., “Effects of an antibacterial membrane on osteoblast-like cells in vitro,” *International Journal of Nanomedicine*, vol. 6, pp. 1853–1861, 2011.
  - [19] M. Chiapasco and M. Zaniboni, “Clinical outcomes of GBR procedures to correct peri-implant dehiscences and fenestrations: a systematic review,” *Clinical Oral Implants Research*, vol. 20, no. 4, pp. 113–123, 2009.
  - [20] C. Rigo, L. Ferroni, I. Tocco et al., “Active silver nanoparticles for wound healing,” *International Journal of Molecular Sciences*, vol. 14, no. 3, pp. 4817–4840, 2013.
  - [21] C. Rigo, M. Roman, I. Munivrana et al., “Characterization and evaluation of silver release from four different dressings used in burns care,” *Burns*, vol. 38, no. 8, pp. 1131–1142, 2012.
  - [22] H. Q. Yin, R. Langford, and R. E. Burrell, “Comparative evaluation of the antimicrobial activity of ACTICOAT® Antimicrobial Barrier Dressing,” *Journal of Burn Care and Rehabilitation*, vol. 20, no. 3, pp. 195–200, 1999.
  - [23] S. Kim, J. E. Choi, J. Choi et al., “Oxidative stress-dependent toxicity of silver nanoparticles in human hepatoma cells,” *Toxicology In Vitro*, vol. 23, no. 6, pp. 1076–1084, 2009.
  - [24] C. Greulich, J. Diendorf, T. Simon, G. Eggeler, M. Epple, and M. Köller, “Uptake and intracellular distribution of silver nanoparticles in human mesenchymal stem cells,” *Acta Biomaterialia*, vol. 7, no. 1, pp. 347–354, 2011.
  - [25] P. Aguiari, S. Leo, B. Zavan et al., “High glucose induces adipogenic differentiation of muscle-derived stem cells,” *Proceedings of the National Academy of Sciences of the United States of America*, vol. 105, no. 4, pp. 1226–1231, 2008.
  - [26] H. C. Lee, P. H. Yin, C. Y. Lu, C. W. Chi, and Y. H. Wei, “Increase of mitochondria and mitochondrial DNA in response to oxidative stress in human cells,” *Biochemical Journal*, vol. 348, no. 2, pp. 425–432, 2000.
  - [27] S. Marchi, C. Giorgi, J. M. Suski et al., “Mitochondria-ros crosstalk in the control of cell death and aging,” *Journal of Signal Transduction*, vol. 2012, Article ID 329635, 17 pages, 2012.

## Research Article

# Electronic Properties of TiO<sub>2</sub> Nanoparticles Films and the Effect on Apatite-Forming Ability

Johanna Löberg,<sup>1,2</sup> Jenny Perez Holmberg,<sup>2</sup> Ingela Mattisson,<sup>1</sup>  
Anna Arvidsson,<sup>1</sup> and Elisabet Ahlberg<sup>2</sup>

<sup>1</sup> DENTSPLY Implants, Box 14, 431 21 Mölndal, Sweden

<sup>2</sup> Department of Chemistry and Molecular Biology, University of Gothenburg, 412 96 Gothenburg, Sweden

Correspondence should be addressed to Elisabet Ahlberg; [ela@chem.gu.se](mailto:ela@chem.gu.se)

Received 23 January 2013; Revised 24 March 2013; Accepted 7 April 2013

Academic Editor: Ryo Jimbo

Copyright © 2013 Johanna Löberg et al. This is an open access article distributed under the Creative Commons Attribution License, which permits unrestricted use, distribution, and reproduction in any medium, provided the original work is properly cited.

Nanoparticle-covered electrodes have altered properties as compared to conventional electrodes with same chemical composition. The changes originate from the large surface area and enhanced conduction. To test the mineralization capacity of such materials, TiO<sub>2</sub> nanoparticles were deposited on titanium and gold substrates. The electrochemical properties were investigated using cyclic voltammetry and impedance spectroscopy while the mineralization was tested by immersion in simulated body fluid. Two types of nucleation and growth behaviours were observed. For smooth nanoparticle surfaces, the initial nucleation is fast with the formation of few small nuclei of hydroxyapatite. With time, an amorphous 2D film develops with a Ca/P ratio close to 1.5. For the rougher surfaces, the nucleation is delayed but once it starts, thick layers are formed. Also the electronic properties of the oxides were shown to be important. Both density of states (DOS) in the bandgap of TiO<sub>2</sub> and the active area were determined. The maximum in DOS was found to correlate with the donor density ( $N_d$ ) and the active surface area. The results clearly show that a rough surface with high conductivity is beneficial for formation of thick apatite layers, while the nanoparticle covered electrodes show early nucleation but limited apatite formation.

## 1. Introduction

Nanocrystalline films composed of sintered nanoparticles of TiO<sub>2</sub> have interesting properties and have been studied for potential use in photoelectrochemical solar cells, electrochromic windows, and batteries with Li-intercalation [1–7]. The advantages compared with conventional materials are the much larger internal surface accessible due to electrolyte penetration of the porous framework, efficient charge separation, and ion conduction since the transport distance for charge carriers to travel becomes short in the nanocrystallites [8, 9]. A disadvantage noted for these applications is the large density of states. These states take part in electron-hole recombination processes and electron transfer reaction at the oxide-electrolyte interface, if located in the bandgap. However, the latter property can be regarded as an advantage for adsorption of redox-active compounds and is therefore

of special interest for dental implant applications, which the present study is focused on. It has, for example, been shown that serum proteins such as fibrinogen adsorb on the titanium surface through a chemisorptions process, that is, involving electron transfer [10]. The ability of a material to attract biomolecules, specific proteins, and blood platelets and thus trigger the blood coagulation are key factors to induce bone formation directly on an implant surface [11, 12]. The electronic behaviour of TiO<sub>2</sub> has also been shown to affect the thrombogenicity of the material [13–15], and one explanation could be the semiconducting behaviour of fibrinogen which is important in the blood coagulation pathway. Fibrinogen has a band structure that fits into the bandgap of TiO<sub>2</sub> and by altering the gap size and/or the  $E_F$  placement of TiO<sub>2</sub>, the protein adsorption and following decomposition of the fibrinogen could be changed [13–15]. It is therefore important to study the electronic properties of different titanium oxide

TABLE 1: Sample description.

Sample name	Underlying surface	Surface modification
TS	Turned titanium	None
TS + 8 nm	Turned titanium	Spin coated with 8 nm TiO <sub>2</sub> particles
TS + 22 nm	Turned titanium	Spin coated with 22 nm TiO <sub>2</sub> particles
TS + P25	Turned titanium	Spin coated with P25 particles
TS + AT-I	Turned titanium	Treated sequentially in oxalic and hydrofluoric acid [16]
Au	Mechanically polished gold	None
Au + 22 nm	Mechanically polished gold	Spin coated with 22 nm TiO <sub>2</sub> particles

layers and in particular to estimate the density of states in the bandgap of TiO<sub>2</sub>.

The aim of the present study is to investigate the effect of surface roughness, morphology, and electronic properties on the apatite-forming ability of surfaces with different nanostructures. For this purpose, surfaces with well-characterized nanoparticles were formed using spin coating. Three different suspensions of nanoparticles were used with 8 and 22 nm clean TiO<sub>2</sub> particles individually dispersed and commercial P25 particles with an individual size of ~30 nm. The P25 dispersion contained also larger aggregates that were transferred to the surface. A turned Ti surface was used as reference, and a nanostructured surface formed by etching in acid solution was used for comparison. Surface roughness, morphology, and composition were determined using AFM, SEM, EDX, and XRD, respectively. The electronic properties were determined using cyclic voltammetry and impedance spectroscopy and correlated with the bioactivity measured by immersion in simulated body fluid for different times.

## 2. Materials and Methods

**2.1. Sample Preparation.** Titanium dioxide (TiO<sub>2</sub>) nanoparticles were synthesized by controlled hydrolysis of TiCl<sub>4</sub> to obtain clean surfaces. TiO<sub>2</sub> particles of different sizes were obtained by synthesis at 0°C but with dialysis and storage of the colloidal dispersions done at 0°C for 8 nm and 20°C for 22 nm sized particles. The dialysis step is important to avoid agglomeration, and the resulting suspensions consist mainly of single nanoparticles. Details about the synthetic procedure and properties of the suspensions are given elsewhere [18, 19]. The two particle sizes were chosen based on previous work where fundamental properties have been addressed and shown to be size dependent [19, 20]. Commercial TiO<sub>2</sub> (Degussa P25), with an individual particle size in the range of 30–80 nm and 4 : 1 ratio of anatase and rutile [21], was carefully washed to remove organic surface species and treated in ultrasonic bath to get a dispersed solution. However, dynamic light scattering showed the existence of larger aggregates, and it was not possible to fully disperse the system. The particles were spin coated onto Ti (grade 4 discs with a turned surface, diameter 1.1 cm) or Au disks (polished with SiC paper (4000), diameter 1.1 cm). Typically, 100 µL of particle suspension (~12.5 g/L for the 8 and 22 nm particles and 10 g/L for P25) was deposited on the electrode surface. The rotation rate was initially 1500 rpm (30 s) and was increased to 3000 rpm (60 s) and then back to 1500 rpm before it was turned off. This

procedure was repeated once. After spin coating, the samples were rinsed with deionized water and left to dry before use. As a complement to the nanoparticle-coated surfaces, the nanostructured TS + AT-I (turned surface treated with oxalic acid and hydrofluoric acid) surface was included in this study. Details for the AT-I treatment have been published elsewhere [16]. Table 1 shows a description of the samples used.

**2.2. Surface Chemistry.** A Siemens D5000 powder diffractometer which utilizes CuKα radiation ( $\lambda = 1.54056 \text{ \AA}$ ) was used for identification of crystalline phases. X-ray diffraction was measured at different incidence angles in order to obtain information from different depths of the samples. For XPS analysis a Quantum 2000 ESCA Scanning Microscope (Physical Electronics, USA) with an X-ray source of monochromatic AlKα was used.

**2.3. Surface Topography.** High resolution SEM images were recorded using Leo Ultra 55 FEG SEM operated at 1 kV. Surface roughness analysis was performed by using atomic force microscopy (AFM) (Nanoscope Multimode IIIa, Digital Instruments). Tapping mode AFM measurements were performed at three points per sample and at three different scan sizes,  $10 \times 10$ ,  $5 \times 5$ , and  $3 \times 3 \mu\text{m}$  (scan frequency 0.8 Hz, 512 lines). The AFM data were imported into MeX [22] (Alicona Imaging GmbH) software where roughness analysis and calculation of 3D-surface roughness parameters were performed. By using multiple scan sizes and by applying a Gaussian filter of different sizes in the MeX software, information about topographical features ranging from 10 µm to 150 nm are received, for details see [23].

**2.4. Electrochemical Characterisation.** Cyclic voltammetry and impedance measurements were performed by using a Gamry Reference 600 Potentiostat/Galvanostat/ZRA. The electrochemical measurements were done in a specially designed three-electrode cell used for stationary conditions. The sample is placed at the bottom of the cell with the turned surface towards the electrolyte. A large Pt counter electrode is concentrically placed around the sample to assure optimal current distribution, and the reference electrode is placed in the middle of the cell. This cell configuration is useful for all types of planar samples and shows good characteristics in impedance measurements. All potentials are referred to the Ag/AgCl (sat KCl,  $E = 0.197 \text{ V}$  versus SHE) reference electrode.

**2.4.1. Cyclic Voltammetry (CV).** Cyclic voltammetry was performed in 0.1 M KOH in a broad potential range. The sweep rate was kept constant at 50 mVs<sup>-1</sup>.

**2.4.2. Electrochemical Impedance Spectroscopy (EIS).** Electrochemical impedance measurements were performed in de-aerated 0.5 M H<sub>2</sub>SO<sub>4</sub>, and a continuous low purge with N<sub>2</sub> gas was maintained during the impedance measurements. Impedance spectra were recorded at a constant potential in the frequency range 1 kHz to 10 mHz with 9 point/decade and an amplitude of 10 mV rms. The potential was stepped by 50 mV from +1 to -0.5 V with a waiting time of 300 s before the next spectra were recorded. The impedance data were fitted by using equivalent circuits consisting of one or two time constants in series with the solution resistance ( $R_{sol}$ ). Each time constant consists of a constant phase element (CPE) in parallel with a resistance related to the oxide. Different models have been used to calculate the effective capacitance depending on the system studied [24, 25]. It has been demonstrated that for lateral distribution of time constants, the solution resistance is included in the calculations, while for a distribution of time constant perpendicular to the surface, it can be omitted. For the system studied here, where a porous oxide is formed and electrolyte can penetrate most of the layer, distribution of time constants occurs laterally due to the porosity of the surface, and the effective capacitance has therefore been calculated using

$$C = \left[ Q \cdot \left( \frac{1}{R_{sol}} + \frac{1}{R_{film}} \right)^{\alpha-1} \right]^{1/\alpha}, \quad (1)$$

where  $R_{sol}$  is the solution resistance,  $R_{film}$  is related to the oxide film resistance, and  $\alpha$  is the dispersion factor for the CPE element. The effective capacitance was used to estimate the electric properties of the semiconducting titanium dioxide layer using the well-known Mott-Schottky relationship (2):

$$\frac{1}{C_{sc}^2} = \left( \frac{2}{\epsilon_r \epsilon_0 e N_d} \right) \left( E - E_{fb} - \frac{kT}{e} \right), \quad (2)$$

where  $C_{sc}$  is the space charge capacitance,  $\epsilon_r$  the dielectric constant of TiO<sub>2</sub>,  $\epsilon_0$  the dielectric constant of vacuum,  $N_d$  the number of charge carriers,  $e$  the charge of the electron,  $E$  the applied potential, and  $E_{fb}$  the flat band potential. Here it is assumed that the double-layer capacitance is much higher than the space charge capacitance. According to (2), a linear dependence is expected from which the number of charge carriers can be obtained from the slope and the flat band potential from the intercept.

**2.5. Immersion in Simulated Body Fluid (SBF).** The SBF solution was prepared at 37°C according to the revised SBF recipe described in [26]. The pH of the solution was set to 7.00 ± 0.05 using 1 M NaOH, and the prepared SBF solution was used fresh. Samples were individually immersed and mounted with the treated surface upside down in 40 mL SBF solution. 9 Samples per category were immersed at 37.0°C, and 3 samples per category were evaluated after 12 h, 72 h,

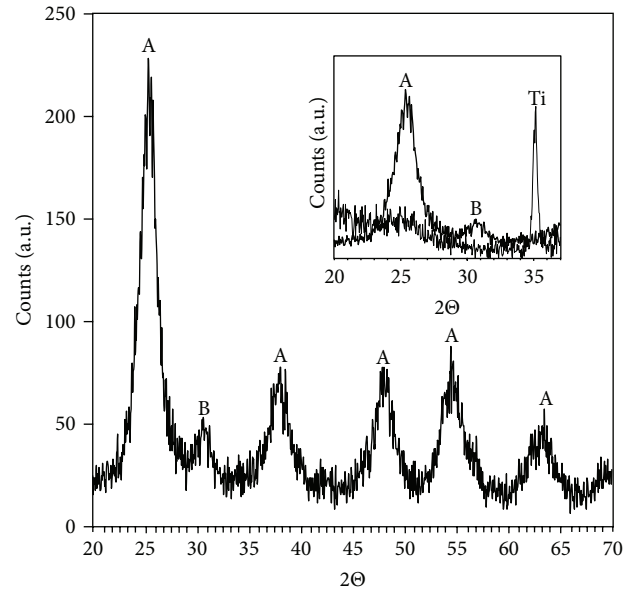


FIGURE 1: X-ray diffraction of TiO<sub>2</sub>-synthesised nanoparticles with 8 or 22 nm size. The particles were dried at 120°C for 16 h prior to the analysis. Diffraction peaks marked with A correspond to anatase while B stands for brookite. The inset shows enlargement of the diffraction pattern for the particles dispersed on Ti (thin line). The film was washed and allowed to dry at room temperature overnight.

and 1 week of immersion. XRD analysis was performed at one sample per category and immersion time to investigate the chemical composition of the sample. SEM (ESEM XL30, FEI Company) and EDX (Apollo 14, EDAX) analyses were performed at 3 points per sample for all sample types to evaluate the amount and morphology of the formed apatite. SEM settings used were 10 kV, working distance 10 mm, and analysis area 126 × 102 μm.

### 3. Results and Discussion

**3.1. Surface Chemistry.** Figure 1 shows X-ray diffraction of the nanoparticles in powder form obtained from suspensions containing 8 or 22 nm particles. The main phase is anatase but with a small contribution from brookite as shown by the reflection at  $2\theta = 30.8^\circ$ . The broad diffraction peaks indicate that the particles consist of smaller crystallites (~4 nm), and growth studies have shown that the particles are formed by slow aggregation of initially formed precipitates of this size [18]. In the inset of Figure 1, the diffraction pattern for the particles attached to titanium is shown. Since the nanoparticle layer is thin, the signal is very weak but the main anatase peak can be observed. This shows that the phase of the particles remains after deposition and drying. The P25 particles attached to titanium show typical diffraction pattern with a ratio between anatase and rutile of ~4/1 [22]. For the TS + AT-I modification, no diffraction peaks from the oxide can be observed, which indicates that the precipitated layer is amorphous or too thin to be detected [16].

XPS on the nanoparticle films shows pure TiO<sub>2</sub> with traces of chloride. No signal for Ti metal was observed, which indicates that the films fully cover the surface. Lower valent



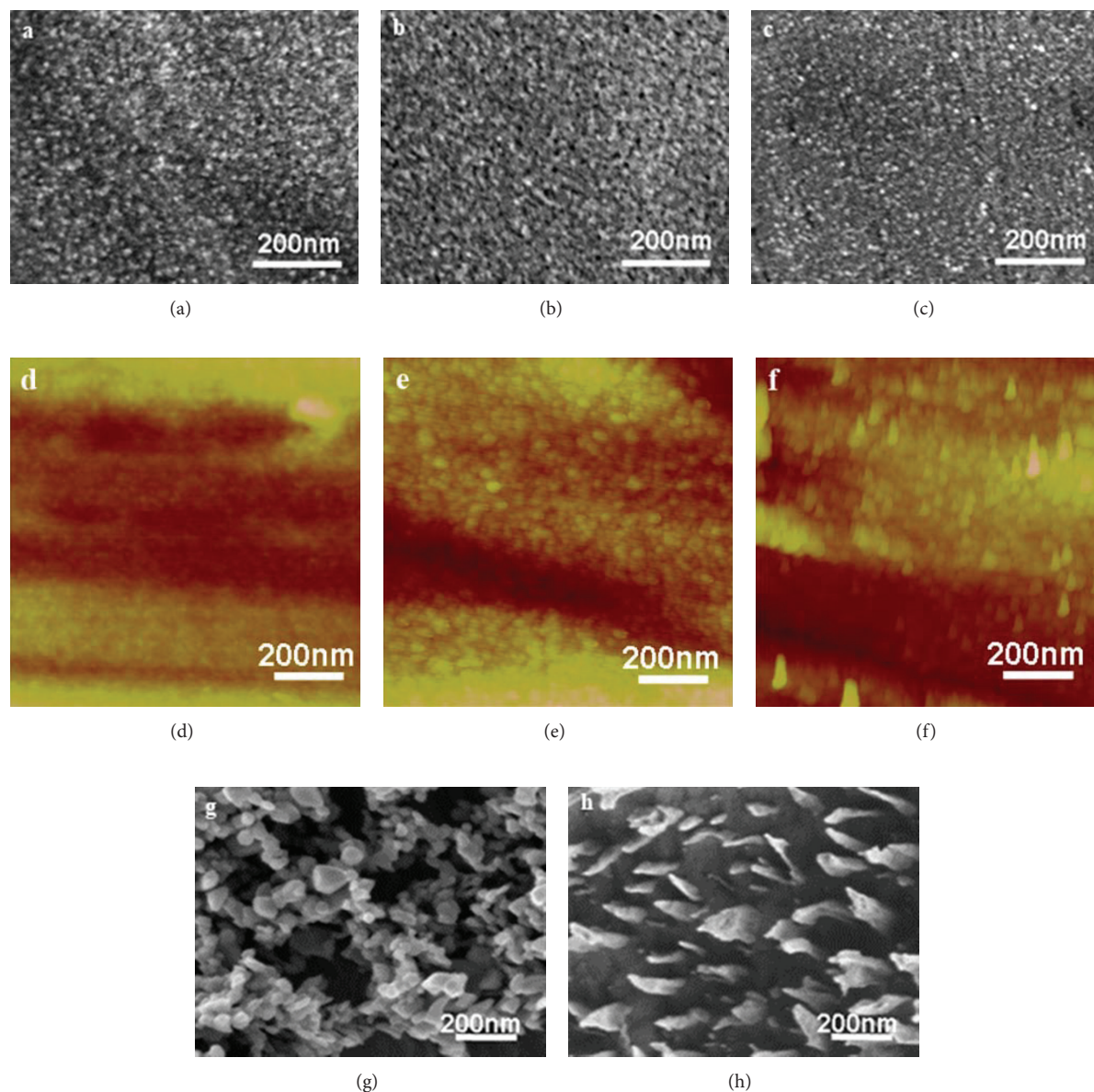


FIGURE 2: SEM images for the (a) TS + 8 nm, (b) TS + 22 nm, (c) Au + 22 nm, (g) TS + P25, and (h) TS + AT-I surfaces. AFM images for the (d) TS + 8 nm, (e) TS + 22 nm, and (f) Au + 22 nm surfaces.

titanium ions were not observed in contrast to other studies showing Ti(III) at the surface of nanoparticles formed by other synthetic routes [27]. The carbon signal is similar for all samples and is related to surface contamination. XPS for the AT-I modification has been studied in detail elsewhere and shows that the oxide film may contain oxalate from the formation process [16]. In this case, a small Ti metal signal is observed illustrating that some parts of the surface have a thin oxide film.

**3.2. Surface Topography.** Figure 2 shows high-resolution SEM images of surfaces coated with 8 nm (TS + 8 nm) and 22 nm (TS + 22 nm) and (Au + 22 nm)  $\text{TiO}_2$  particles. All three surfaces look fairly smooth and in order to further investigate the surface roughness also AFM images were

recorded, middle row of Figure 2. In AFM, the TS + 8 nm surface looks smoother than the TS + 22 nm and Au + 22 nm surfaces, which is also quantified by surface roughness measurements, see Figure 2. From the SEM and AFM images of these surfaces it seems like the underlying substrate is fully covered. This is not the case for the two other modifications used in the present work. The suspension of P25 contained agglomerates of particles, and these were transferred to the Ti surface during the spin coating procedure. As a result, the surface roughness is high but in between the turned surface is visible, Figure 2(g). For the TS + AT-I surface etched in oxalic acid and hydrofluoric acid sequentially, rather large precipitates form with a very thin oxide layer in between, Figure 2(h). In contrast to the spherical nanoparticles, the precipitates on the TS + AT-I surface can be regarded as rods



TABLE 2: 3D surface roughness parameters determined by AFM.

Sample	$S_a$ (nm)		$S_{dq}$		$S_{dr}$ (%)	
	Average	Stdev	Average	Stdev	Average	Stdev
TS	11.6	0.67	0.26	0.09	3.51	2.06
TS + 8 nm	8.34	—	0.14	—	1.05	—
TS + 22 nm	10.6	1.4	0.16	0.01	1.32	0.20
TS + P25	63.3	9.2	1.73	0.26	109.3	24.5
TS + AT-I	41.8	6.2	0.89	0.23	38.3	19.2
Au	13.9	—	0.24	—	2.68	—
Au + 22 nm	9.02	1.8	0.14	0.02	1.00	0.70

$S_a$ : average height of surface,  $S_{dr}$ : developed interfacial area,  $S_{dq}$ : root mean square of surface slope. Data from  $10 \times 10 \mu\text{m}$  scan size a Gaussian filter of 20% of the horizontal width ( $1.996 \mu\text{m}$ ).

with a height of  $0.45 \mu\text{m}$  (determined from the average of maximum height of 5 peaks and valleys,  $S_{10z}$ ).

Topographical analysis of the coated and nanostructured surfaces was performed by AFM analysis using overlapping scan sizes and a Gaussian filter of different sizes to obtain information of surface features in the range of 10 to  $0.150 \mu\text{m}$  as described earlier [23]. The 3D surface roughness parameters were calculated using the MeX software [22], and values for three different parameters are listed in Table 2.

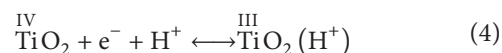
The  $S_a$  value (average height) is significantly larger for the surfaces TS + P25 and TS + AT-I than for the nanoparticles-coated surfaces and the turned surface. Both surface treatments induced additional surface structures on top of the turned surface without fully covering it, Figure 2. The coatings containing 8 and 22 nm particles completely covered the turned surface with particles, which in turn caused a decrease in surface roughness since the turning tracks are covered, Figure 2 and Table 2. The same trend is observed for the gold substrate, where the  $S_a$  value decreases after coating with 22 nm particles. There is only a slight difference between the  $S_a$  values for the TS + 8 nm and TS + 22 nm surfaces, but the lower value obtained for the smaller particles indicates that the curvature of the particles are reflected in the surface roughness. The root mean square of the slope ( $S_{dq}$ ) has been shown to correlate with the interface shear strength and is thus an important parameter to investigate for dental implant applications [28, 29]. From a biomechanical point of view, a large  $S_{dq}$  value is desired giving the TS + P25 surface an advantage. The trend in  $S_{dr}$  (developed interfacial area) values follows the same trend as the  $S_a$  and  $S_{dq}$  values with the smallest values obtained for the surfaces coated with nanoparticles. Analysis of roughness parameters calculated from  $5 \times 5 \mu\text{m}$  and  $3 \times 3 \mu\text{m}$  scan sizes shows lower absolute numbers but the trends for the different surfaces are the same as shown in Table 2.

### 3.3. Electrochemical Characterisation

**3.3.1. Cyclic Voltammetry.** Cyclic voltammetry was used to characterise the electronic properties of the coated films. In Figure 3, examples of voltammograms are shown to illustrate the influence of scan range and number of scans for one type of electrodes (Figure 3(a)), different particle sizes

(Figure 3(b)), partially coated electrodes (Figure 3(c)), and different substrates (Figure 3(d)).

The general features of the voltammograms obtained with Ti as substrate are the same with a symmetrical process at the most negative potentials and a peak at less negative potentials. The two different processes have been discussed in the literature in relation to films made of sintered  $\text{TiO}_2$  nanoparticles, where the electrolyte can penetrate the layer [1, 30–34]. The process observed at the most negative potentials has been attributed to charge accumulation in the conduction band (3) or filling traps just below the conduction band (4). In both cases, adsorption of protons takes place to obtain charge balance in acid solution [32]:



In alkaline solutions, the electrolyte cation is probably the charge balancing species, that is, adsorption of  $\text{K}^+$  in the present case. The peak at less negative potentials has been attributed to filling of surface states below the conduction band, that is, reduction of Ti(IV) to Ti(III) according to (4). For reaction (4), the formation of  $\text{TiO}(\text{OH})$  is also possible in alkaline solution. Alternatively, the peak at less negative potentials can be attributed to trap states at the grain boundaries in the film [1, 32]. Usually, the current at the most negative potentials increases exponentially, and eventually, hydrogen evolution takes place by reduction of water. The symmetry between cathodic and anodic charge observed for the nanoparticle-covered electrodes, TS + 8 nm and TS + 22 nm, indicates that faradaic processes are not involved if the potential is limited to  $-1.8 \text{ V}$ . Polarising to more negative potentials results in further increase in the current due to hydrogen evolution (not shown). In contrast to other studies on nanoparticle-covered electrodes, the current goes through a maximum on the negative going scan, before hydrogen evolution sets in. The reason for this is not known but may be related to complete filling of energy levels just below the conduction band. The peak at less negative potentials has been attributed to filling of surface states or trap states at the grain boundaries in the film as mentioned above. In the present study, the films are not sintered, and the amount of

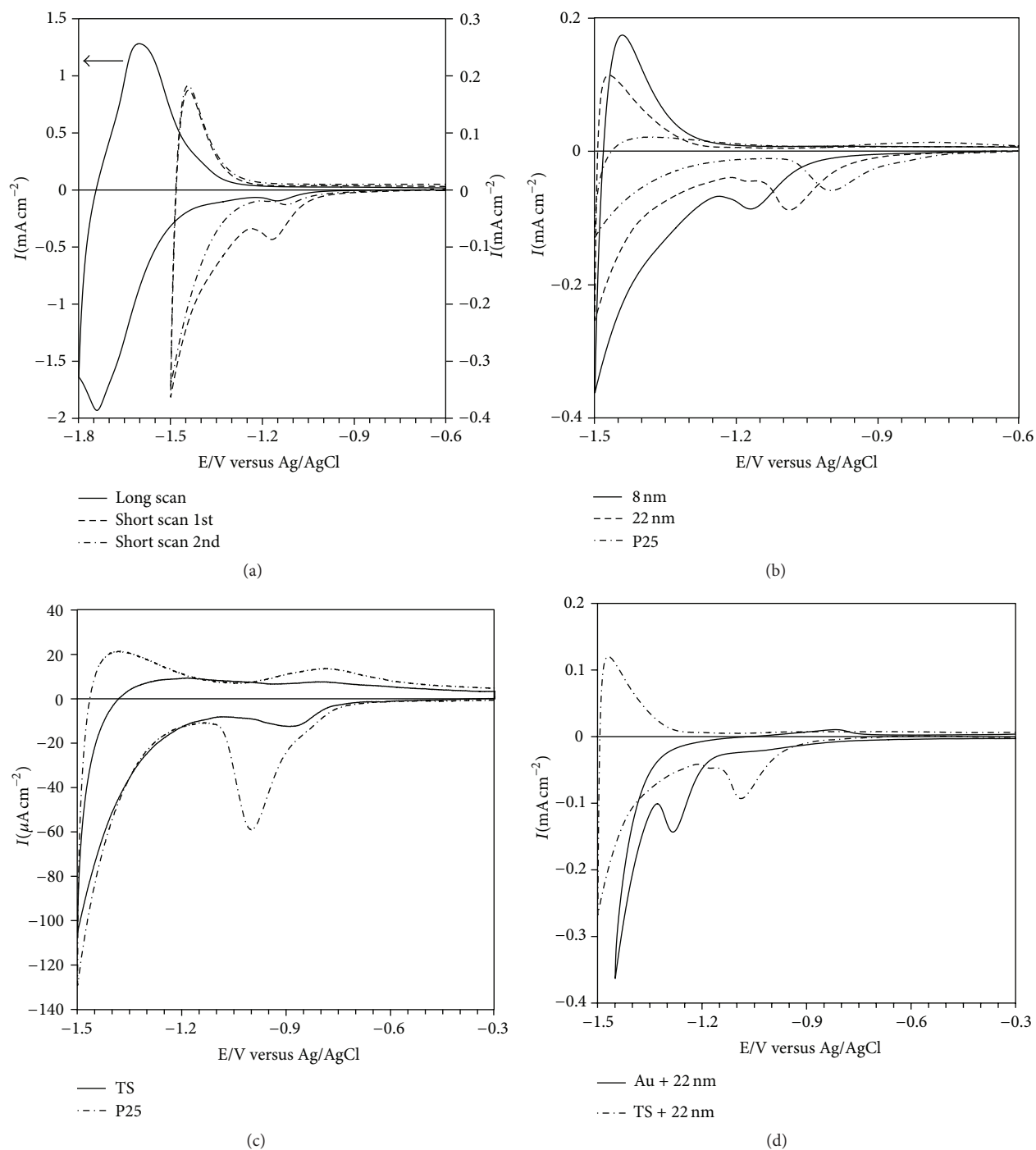


FIGURE 3: Cyclic voltammetry on different surfaces in deaerated 0.1 M KOH. (a) Surface coated with 22 nm  $TiO_2$  particles. The short and long scans are made on different samples. Note that the scale to the left refers to the long scan. For the short scan, both the 1st and the 2nd cycles are shown. Comparison between surfaces (b) coated with different nanoparticle sizes, (c) uncoated turned surface and coating with P25, and (d) different substrates. Sweep rate is at  $50\ mVs^{-1}$ .

grain boundaries is expected to be low and therefore the peak is most likely due to surface states. The positive potential limit was 0 V but this was not sufficient to completely emptying the surface bands filled during the negative going scan. This is evident from the much smaller peak observed on subsequent sweeps, Figure 3(a). The peak potential shifts depending on

the coating with the most negative peak potential for the TS + 8 nm electrode followed by the TS + 22 nm and TS + P25 surfaces, Figure 3(b) and Table 2. Also the current for the process at more negative potentials depends on the type of particles, Figure 3(b), and has been related to the active surface area of nanoparticle films, indicating that the active

TABLE 3: Peak potentials determined from CV,  $E_{fb}$ , and  $N_d$  determined from EIS.

Sample	<sup>a</sup> $E_p/V$	<sup>b</sup> Rel. active area ( $A_{aa}$ )	<sup>c</sup> $E_{fb}/V$	<sup>c</sup> $N_d \times 10^{-19}/\text{cm}^{-3}$	<sup>d</sup> $N_d \times 10^{-19}/A_{aa}$
TS	-0.89	1	-0.35 <sup>d</sup>	84 <sup>d</sup>	84
TS + 8 nm	-1.16	2.65	-0.30	47	17.7
TS + 22 nm	-1.09	1.77	-0.30	47	26.6
TS + P25	-1.00	1.30	-0.35	50	38.5
TS + AT-I	-0.93	1.88	-0.41	119	63.3
Au + 22 nm	-1.27	—	-0.33	0.13	—

<sup>a</sup> $E_p$  is determined in 0.1 M KOH. <sup>b</sup>Calculated on the exponential term for  $E = 0 - (-1.5)$  V. <sup>c</sup> $E_{fb}$  and  $N_d$  are determined in 0.5 M  $\text{H}_2\text{SO}_4$ . <sup>d</sup>From [17], recalculating the value for  $E_{fb}$  to the pH is used in this study.

surface area increases with decreasing particle size. For the native oxide always present on titanium metal, the reduction peak appears at less negative potentials (-0.89 V) compared with the particle-covered electrodes, and the redox process shows some reversibility with an oxidation peak at -0.81 V. Some reversibility in the redox process at these potentials is also observed for the TS + P25 electrode, Figure 3(c). The total charge for the naturally formed oxide is lower than for TS + P25, which is expected since the available surface area will be larger for the nanoparticle film of P25. A close look at the voltammogram for TS + P25 indicates that there is a contribution from the uncovered surface with naturally formed oxide (shown as a shoulder of the peak).

This is in agreement with the SEM image in Figure 2, where the uncovered surface is visible in the porous structure. The process at more negative potential is however the same and differs only in the reversibility with higher anodic charge for the TS + P25 electrode. The reversibility of this process is higher for the TS + 8 nm and TS + 22 nm electrodes compared to TS + P25 and the turned surfaces and is probably related to the smaller particle sizes and well defined surfaces. The lack of reversibility can be due to Faradaic processes and that is probably the case for the gold electrode covered with 22 nm  $\text{TiO}_2$  particles, Au + 22 nm. The reduction peak is closer to the conduction band, and hydrogen evolution is probably taking place at more negative potentials since no oxidation peak is observed, Figure 3(d). However, a small oxidation peak is observed at -0.82 V in close agreement with the peak observed for the Ti-coated electrodes. This peak is associated with emptying of energy states on the surface of the  $\text{TiO}_2$  particles.

Based on the voltammetric response and assuming that no Faradaic processes occur, the density of states (DOS) in the bandgap and the electron density can be determined using (5) [31, 33].

Let

$$g_0(-eE) = -\left(\frac{I}{eLA\nu}\right)(eV), \quad (5)$$

where  $g_0(-eE)$  is the first estimate of the DOS in the bandgap valid at zero Kelvin,  $E$  is the electrode potential,  $L$  the thickness of the layer,  $e$  the elemental charge,  $A$  the surface area, and  $\nu$  the sweep rate. More elaborate equations are available to account for elevated temperature [35] but as a first approximation (6) will be used. The experimental data show two types of states, one associated with the exponential

tail of the conduction band,  $g_{\text{tail}}(-eE)$ , at the most negative potentials, and states in the bandgap with a Gaussian-like distribution,  $g_{\text{gauss}}(-eE)$ , see (6) and (7).

Let

$$g_{\text{tail}}(-eE) = g_{\text{tail},BE} \exp\left[\frac{-\alpha FE}{RT}\right], \quad (6)$$

where  $g_{\text{tail},BE}$  is the DOS at the edge of the conduction band and  $\alpha$  is related to extension of the tail into the bandgap [31, 33]. The Gaussian distribution is given in (7).

Let

$$g_{\text{gauss}}(-eE) = g_{\text{gauss},\text{sat}} \cdot \frac{\exp\left[-(E - E_p)^2/2\sigma^2\right]}{\sigma\sqrt{2\pi}}, \quad (7)$$

where  $g_{\text{tail},BE}$  corresponds to the complete filling of the states in the bandgap,  $E_p$  is the peak potential, and  $\sigma$  is the standard deviation about the peak potential. An attempt was made to fit experimental data to these equations but the states in the bandgap deviates from a Gaussian distribution, and reliable values could not be obtained. A more detailed analysis of the experimental data will be presented elsewhere.

For porous nanostructured films, the charge associated with the exponential increase has been shown to be proportional to the interfacial area [31]. Since the thicknesses of the coated layers are not known, the values extracted from the exponential term can only be used to calculate the interfacial area normalised with the area of the uncoated surface, Table 3. Comparing these values with the developed interfacial area,  $S_{dr}$ , shows that even though P25 has the largest  $S_{dr}$  value the active area is only slightly higher than for the turned surface. In contrast, the smooth appearance of the TS + 8 nm and TS + 22 nm surfaces yields higher interfacial area with the largest area obtained for the smallest nanoparticles. The lack of agreement originates from the fact that  $S_{dr}$  represents the physical (passive) area while the interfacial (active) area is created in contact with the electrolyte.

**3.3.2. Electrochemical Impedance Spectroscopy.** In Figure 4, the Mott-Schottky plots for the different surfaces are shown. For Ti surfaces coated with 8 and 22 nm, the Mott-Schottky behaviour is the same, and only one curve is shown in the graph. For these surfaces, a linear Mott-Schottky relationship is found except close to the flat band potential, where a non-linear behaviour is observed for all surfaces. For the TS + P25

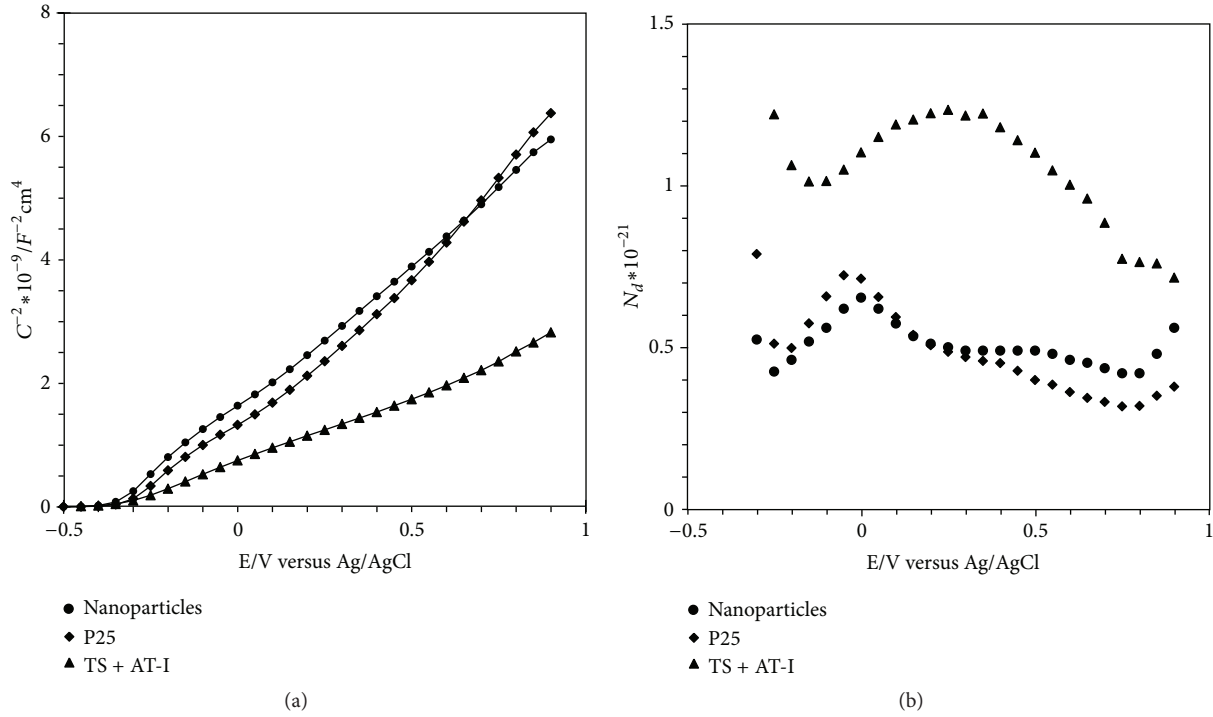


FIGURE 4: (a) The Mott-Schottky plots for different surfaces. The response for the TS + 8 nm and TS + 22 nm surfaces is the same and is shown as one graph. (b) The number of charge carriers.

and TS + AT-I surfaces, a change in the slope is observed at the most positive potentials. The number of charge carriers was calculated at each potential from the slope of the Mott-Schottky plot and is given in the inset to Figure 4. Despite changes in the slope of the Mott-Schottky curves, the number of charge carriers is fairly constant and the value for the most linear region is given in Table 3 together with the flat band potential. The flat band potentials were similar for the different surfaces, and the potentials are in good agreement with previously reported values [2, 36].

The potential drop over the oxide can be divided into two parts: one takes place over the less conducting outer part of the oxide and the other over the more conducting part closer to the metal/oxide interface [37–39]. Close to the flat band potential, most of the potential drop takes place over the insulating part, and it is possible to calculate the part of the potential, that is, used to establish the space charge region in the semiconducting part of the oxide [38]. It has been argued that for insulating films the sharp decrease of the  $C^{-2}$  versus  $E$  curve close to the flat band potential is due to the capacitance of the oxide [38]. This is clearly the case for nanoparticle-covered gold electrodes and will be discussed further below.

For the surface covered with P25, the slope increases significantly at potentials higher than 0.4 V, giving a lower donor density by a factor of 1.6. This line can be extrapolated to yield an apparent flat band potential close to 0 V. Since the flat band potential is expected to be close to -0.35 V at the pH used in the present work, the apparent flat band potential is probably affected by surface states.

The Mott-Schottky plot for the Au + 22 nm electrode looks different compared with the other electrodes, Figure 5.

In this case the capacitance was calculated from impedance values obtained at a constant frequency of 100 Hz.

For comparison, the Mott-Schottky curve for the TS + 22 nm electrode is also shown, with capacitance values calculated in the same way. Starting at positive potentials, the capacitance is constant for the Au + 22 nm surface, that is, independent of potential. This capacitance is therefore related to the capacitance of the insulating oxide film. Close to the flat band potential the curve changes rapidly. By correcting for the oxide capacitance, the donor density and the flat band potential can be estimated, Table 3. From the oxide capacitance value, the average oxide thickness can be calculated using (8). A value of 28 nm was obtained, which indicates that only a monolayer of particles is attached to the surface in case of gold.

Let

$$d = \frac{\epsilon_0 \epsilon_r A}{C}, \quad (8)$$

where  $\epsilon_0$  is the dielectric permittivity of vacuum,  $\epsilon_r$  is the dielectric constant of  $\text{TiO}_2$  ( $\epsilon_r = 60$ ),  $A$  is the electrode area, and  $C$  is the capacitance.

The number of charge carriers is much lower for the nanoparticles film on gold than for the same film on titanium. This indicates that the  $\text{TiO}_2$  nanoparticles are interacting more closely with the thin oxide film on titanium than with the gold metal. As a consequence, it is tempting to conclude that the surface states observed in cyclic voltammetry originate not only from the particles but also from the interface between the particles and the native oxide film on Ti. For the TS + AT-I surface, the number of charge carriers is higher



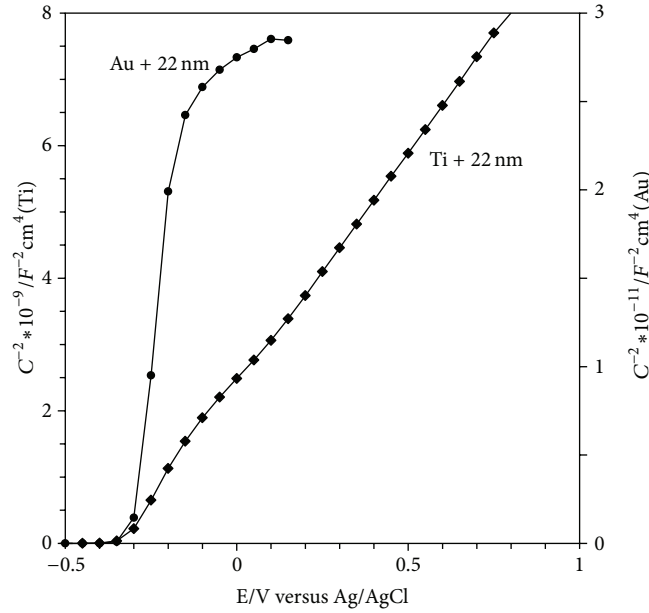


FIGURE 5: The Mott-Schottky plots obtained at 100 Hz. Note that the scale to the right is related to the Au + 22 nm electrode.

than for the nanoparticle films and also higher than for the native oxide (TS), Table 3. One reason for the slightly higher conductivity could be the presence of titanium hydride in the metal phase. However, for blasted samples, the conductivity for surface with the AT-I treatment was found to be lower than for the blasted sample [16].

The voltammetric measurements were made in alkaline solution and by using the experimentally determined flat band potentials obtained in acid solution and assuming a Nernstian pH shift, the flat band potential was calculated for pH 13,  $E_{fb} = -1.1 \pm 0.1$  V. In Figure 6, the density of states is plotted as a function of potential with reference to the flat band potential.

For the surface with 8 nm particles, the maximum in DOS occurs at higher energies than the flat band potential, while for the other surfaces the maximum is close to  $E_{fb}$  (TS + 22 nm) and at positive potentials with respect to  $E_{fb}$  (TS + P25 and TS). The location of the energy bands may be important for adsorption of bioactive compounds and in turn for the surface ability to function *in-vivo*. This will be further discussed below in relation to the result obtained after immersion in simulated body fluid.

**3.4. Immersion in Simulated Body Fluid (SBF).** The ability of the surfaces to induce apatite nucleation was evaluated by immersion samples in SBF solution for 12 h, 72 h, and 1 week. The SBF solution contains ions with similar concentration as the human blood plasma and the recipe for SBF solutions can vary. In the present paper, the revised SBF recipe presented by Oyane et al. [26] was used. The samples were mounted with the treated surface hanging upside down to prevent gravitational precipitation.

The amount of apatite formed was measured by EDX. The apatite coverage ( $\Theta$ ) was calculated from the ratio of the

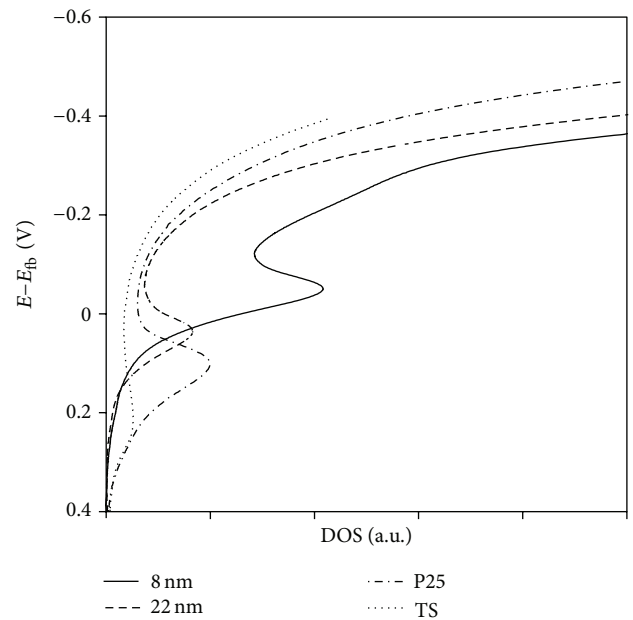


FIGURE 6: Density of states calculated using (6) with the layer thickness constant equal to 3 nm, which is the thickness of the naturally formed film. The relative DOS values are affected by the thickness of the layer.

titanium signal after and before immersion in SBF solution using (9). It is assumed that apatite is the only precipitate formed during immersion.

Consider

$$\Theta = 1 - \left( \frac{Ti_{SBF}}{Ti} \right). \quad (9)$$

When analyzing data for all surface groups immersed in SBF for 12 h with one-way ANOVA analysis (SPSS Inc,

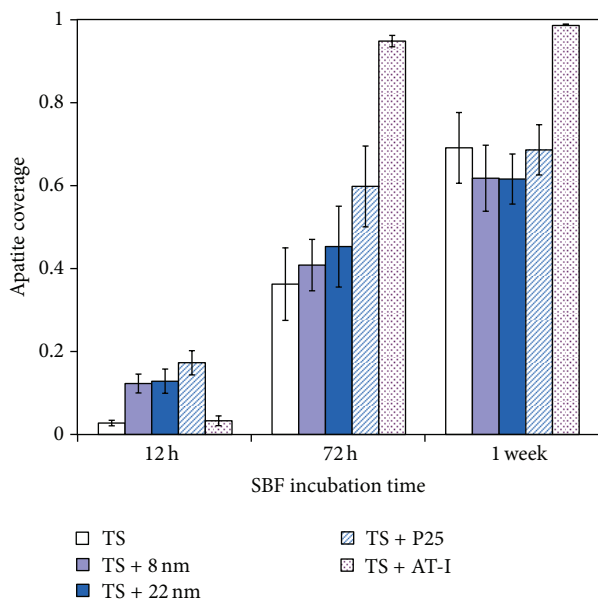


FIGURE 7: Apatite coverage on different surfaces after immersion in SBF solution for 12 h, 72 h, and 1 week.

Chicago, USA), there was a statistically significant difference ( $P < 0.001$ ) between surface groups. The results are shown in Figure 7, and it is interesting to note that the early nucleation of apatite is higher for surfaces coated with  $\text{TiO}_2$  nanoparticles compared to the reference (TS) and the TS + AT-I surface. Early nucleation of apatite crystals has been reported for surfaces with anatase structure as compared to an amorphous or rutile structure [40–42]. This could be one explanation for the early nucleation rate observed for the coated surfaces, since the surface particles are predominantly of anatase phase [18, 43]. The experimental data also show that the active surface area increases with decreasing particle size, Table 3. A higher surface area provides more nucleation sites and may facilitate the deposition of apatite. Also the form of the nanosized deposits seems to have an influence on the early nucleation since the AT-I surface, with rod like deposits, has similar active area as the TS + 22 nm surface but different nucleation rate. It is also worth mentioning that the electric properties, that is, number of charge carriers, seem to correlate with the early nucleation. Both TS and TS + AT-I have higher  $N_d$  than the nanoparticle-covered surfaces. After 72 h immersion in SBF, the difference between the reference and the coated surfaces (TS + 8 nm and TS + 22 nm) has disappeared ( $P = 0.30$  when compared with one-way ANOVA). Instead, the TS + AT-I surface shows the highest apatite coverage ( $P < 0.001$  when compared to TS + P25 in a Student's *t*-test). This trend is maintained after 1 week (Figure 7), when the TS + AT-I surface shows the highest coverage degree ( $P < 0.001$ ) compared to the reference and coated surfaces, among which no differences are found ( $P = 0.082$  when the groups are compared with a one-way ANOVA analysis).

The morphology of the different surfaces was investigated by SEM, and clear differences were obtained, Figure 8. After 1 week immersion in SBF, thin apatite layers were formed

on the reference and coated surfaces leaving the underlying surface still visible. For the TS + AT-I surface, the underlying surface was completely covered by a thick apatite layer, and this is also confirmed by the EDX measurements, Figure 7. The influence of surface roughness on apatite formation has been previously investigated and with surface roughness corresponding to an  $R_a$  value between 0.2 and 0.6  $\mu\text{m}$  a continuous and adherent apatite layer has been shown to form on various materials [40, 44, 45]. It is difficult to compare absolute values of roughness parameters due to differences in measuring techniques and analysis. However, relative values can be used, and the results after 1 week of immersion support the previous findings that rougher surfaces favour formation of thick and adherent apatite layers compared to smoother surfaces, Table 3 and Figure 8.

Fractured apatite layers with different characteristics were observed for all surfaces except for the TS + P25 surface. Fractures formed on TS + AT-I (Figure 8(e)) after one week of immersion resembled fractured apatite layers formed on  $\text{TiO}_2$  coatings [46],  $\alpha\text{-CaSiO}_3$  ceramics [47], chemically treated titanium [48], and alkali- and heat-treated titanium [49]. The apatite layer formed on the TS + 8 nm and TS + 22 nm surfaces (Figures 8(b) and 8(c)) exhibited another type of fractures similar to those on apatite layers formed on titanium, first incubated in a fibronectin solution and thereafter in Hank's Buffer Saline Solution (HBSS) for one week [50]. The cracks or fractures have been suggested to be caused by drying shrinkage [40, 51] and have been observed to be larger and deeper with increasing immersion time [40, 51]. An alternative explanation is related to the 3D growth mechanism for thick apatite layers, where nucleus on the surface grows and eventually forms a fully covering film. When the different nuclei start to interact, stresses are imposed and the apatite layer cracks [41, 52]. This mechanism seems to be valid for the TS + AT-I surface with no precipitates after 12 h but a fully covering film after 72 h. The mechanism of nucleation seems to be different for the surfaces with nanoparticles. The fast precipitation of hydroxyapatite at certain sites on the surface is followed by 2D growth, where the layer has weak interaction with the underlying substrate. The formation of a 2D layer seems to prevent the formation of bigger agglomerates commonly observed and as a consequence the layer remains thin. The early nucleation observed on surfaces covered with nanoparticles is illustrated for the TS + 22 nm surface in Figure 9. After 12 h, distinct precipitates are observed (marked with arrows in Figure 9(a)) but the surface is not fully covered by precipitates. The Ca/P ratio of the precipitates at this stage is close to 1.7, and no Ca and P signals were obtained in between the precipitates. This indicates, formation of hydroxyapatite ( $\text{Ca}_5(\text{PO}_4)_3(\text{OH})$ ), which is the thermodynamically most stable phase [53]. However, the rate of formation for hydroxyapatite has been reported to be much slower than for other apatite compounds [54]. Hydroxyapatite is the main mineral in bone and is crucial to obtain high mechanical strength [55]. After 72 h of immersion, the surface is covered with a thin apatite layer and cracks start to form, Figure 9(b). It seems like the crack propagates from the initial precipitates due to stresses induced by the mismatch between the precipitates and the layer. After one week

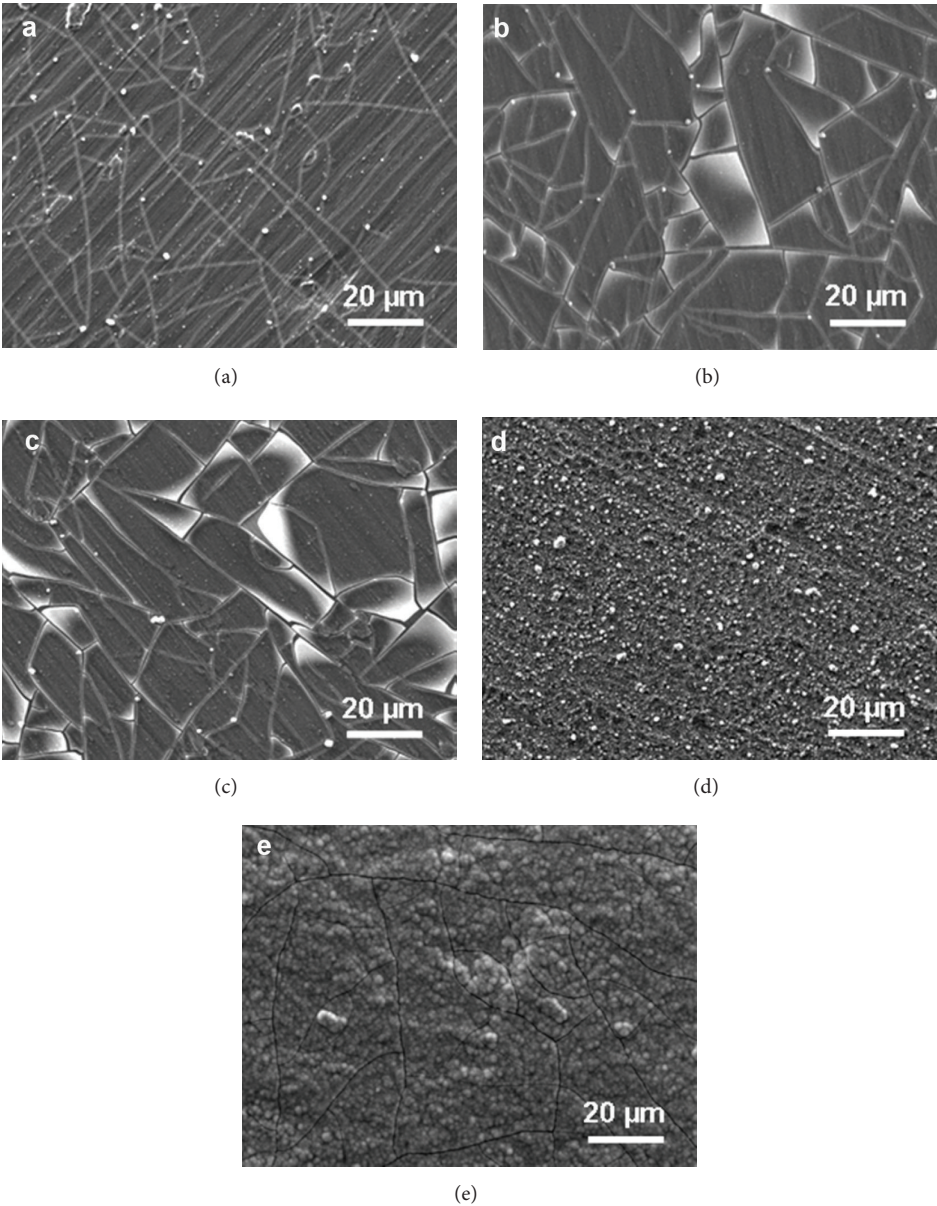


FIGURE 8: SEM images after immersion in SBF solution for 1 week. Titanium discs with (a) turned surface (TS) and (b)–(d) coated surfaces with 8 nm (TS + 8 nm), 22 nm (TS + 22 nm), and P25 (TS + P25) particles. (e) Shows turned surface treated with oxalic acid and diluted hydrofluoric acid (TS + AT-I).

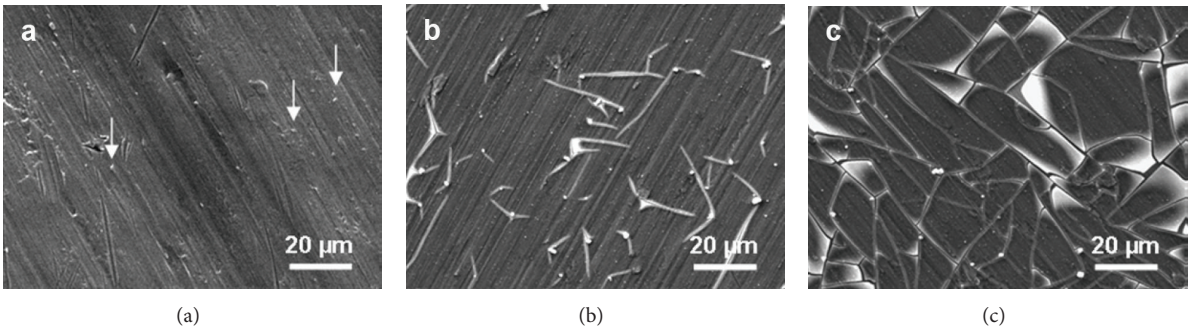


FIGURE 9: SEM images of the TS + 22 nm surface after immersion in SBF solution for (a) 12 h, (b) 72 h, and (c) 1 week. Distinct precipitates were observed after 12 h (marked with arrows).



of immersion, the apatite layer is fully developed but still thin, Figure 9(c). In the present study, all surfaces (except TS + P25) had fractures irrespective of the surface roughness, Table 3 and Figure 8. However, the apatite layers of the TS + 8 nm and TS + 22 nm surfaces seem to be detaching from the underlying surface. EDX measurements performed within a crack in the apatite layer show no or only traces of Ca and P. Detachment of apatite layers has been reported elsewhere [44, 56] and are believed to be caused by weak interactions with the underlying substrate and the absence of surface roughness. Also in the study by Leitão et al. [45], detachment of apatite layers was more pronounced on smooth surfaces than on rough surfaces.

The Ca/P ratio of the formed apatite films was calculated from the EDX measurements and was found to range between 1.42 and 1.56 for all surfaces after 72 h and 1 week immersions. This could indicate the formation of tricalcium phosphate ( $\text{Ca}_3(\text{PO}_4)_2$ ) with Ca/P ratio = 1.5. However, a Ca/P ratio of ~1.5 has also been reported for amorphous layers [57], and it has been shown that the Ca/P ratio depends on the synthesis conditions with values ranging from 1.3 to 1.8 [53].

The chemical composition of the formed apatite layers was analysed by grazing angle-X-ray diffraction (GI-XRD). Although the EDX measurements show rather high apatite coverage for the TS, TS + 8 nm, TS + 22 nm, and TS + P25 surfaces after 1 week, only weak and broad diffraction signals were obtained. This indicates that the layers formed are amorphous, which is also supported by the Ca/P ratio 1.5. Homogeneous growth from an SBF solution has been shown to start with the formation of an amorphous phase with subsequent formation of small apatite crystals [53]. For the TS + AT-I surface, where thicker apatite layers were obtained, clear diffraction peaks for hydroxyapatite [58] are observed after 72 h and 1 week of immersion in SBF, Figure 10.

The long term results show that on a rougher surface the development of thick apatite layers is facilitated. However, the smoother surfaces containing nanoparticles show faster nucleation and formation of thin 2D layers of amorphous apatite. The correlation between a surface ability to nucleate hydroxyapatite and *in-vivo* response has been recently reviewed [59] and challenged [60]. Surfaces with poor ability to nucleate apatite are shown to work well *in-vivo* and vice versa [60]. It can be argued that some of the inconsistency originates from different apatite formation mechanisms.

#### 4. Conclusions

The electronic properties of  $\text{TiO}_2$  nanoparticle films on titanium and gold differ significantly with lower conductivity for the film on gold. The reason for this is probably a stronger interaction between the native oxide on titanium and the nanoparticles as compared with the gold nanoparticle interaction. Differences in the electronic structure of the different nanoparticle films are also visible in cyclic voltammetry. The peak related to surface states with energy bands in the bandgap of  $\text{TiO}_2$  moves closer to the conduction band as the donor density in the film decreases. The donor density is calculated from the impedance measurements and related to the active surface area determined from cyclic voltammetry.

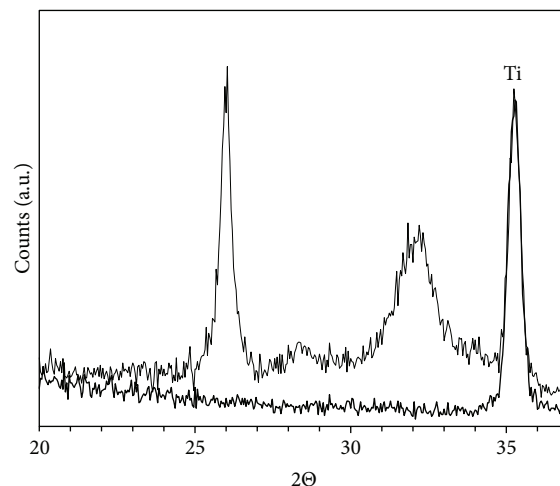


FIGURE 10: X-ray diffraction on TS + AT-I before (thick line) and after (thin line) immersion in SBF solution. The diffraction peaks at  $2\theta$  values 26, 28, and  $32^\circ$  correspond to crystalline hydroxyapatite. The diffraction spectra are normalised to the titanium peak at  $2\theta = 35$ .

The trend in the active surface area is different from the trend observed for the developed interfacial area,  $S_{dr}$ , which illustrates the differences between the physical area and the area related to the semiconducting properties of the oxide.

Immersion in SBF solution can be a measure of the bioactivity of different surfaces. In the present study, two types of nucleation and growth behaviours were observed. For the rougher surfaces, the nucleation is initially delayed but once it starts, thick layers are formed. These layers have cracks induced by stresses in the film formed when different growing nuclei coalesce. For the smoother surfaces with small anatase nanoparticles, the initial precipitation is fast but only few small nuclei of hydroxyapatite are formed leaving the rest of the surface uncovered. On these surfaces, an amorphous 2D film develops with a Ca/P ratio close to 1.5. The growth of this layer is slow and after one week of immersion the underlying surface structure is still visible through the apatite layer. The influence of different nucleation mechanisms on the biocompatibility is not known but would be of great interest to explore.

For surface films formed from small well dispersed nanoparticles, a porous layer is created on the surface. This results in both a larger donor density as determined from the impedance measurements and a larger active area compared with the turned surface and the surface containing agglomerates of P25. For surfaces with similar roughness, the ability to nucleate apatite is lower for less conducting oxide layers as shown here where for the more conducting surface film TS + AT-I a thick apatite layer is formed. This surface film also has a large developed surface area. The physical surface roughness seems to have an important role in the apatite formation since for the reference surface (TS), with rather high conductivity, apatite formation is limited. For the early nucleation, the nanoparticle-covered surfaces seems to be preferred.

The high number of energy states in the bandgap found for the nanoparticles surfaces may be beneficial for



adsorption of redox active proteins such as fibrinogen and will be investigated in a forthcoming study.

## Conflict of Interests

The authors of the paper have no financial relationship with the commercial enterprises Nanoscope (Digital Instruments), MeX (Alicona Imaging GmbH), or FEI Company.

## Acknowledgments

Financial support from the Swedish Research Council (2005-21028-35344-27) is gratefully acknowledged. Traveling scholarships have been obtained from the faculties of arts and science at Gothenburg University.

## References

- [1] T. Berger, T. Lana-Villarreal, D. Monllor-Satoca, and R. Gómez, "Charge transfer reductive doping of nanostructured  $\text{TiO}_2$  thin films as a way to improve their photoelectrocatalytic performance," *Electrochemistry Communications*, vol. 8, no. 11, pp. 1713–1718, 2006.
- [2] G. Boschloo and D. Fitzmaurice, "Electron accumulation in nanostructured  $\text{TiO}_2$  (anatase) electrodes," *Journal of Physical Chemistry B*, vol. 103, no. 37, pp. 7860–7868, 1999.
- [3] M. Grätzel, "Photovoltaic performance and long-term stability of dye-sensitized mesoscopic solar cells," *Comptes Rendus Chimie*, vol. 9, no. 5-6, pp. 578–583, 2006.
- [4] A. Hagfeldt, U. Björkstén, and S. E. Lindkvist, "Photoelectrochemical studies of colloidal  $\text{TiO}_2$ -films: the charge separation process studied by means of action spectra in the UV region," *Solar Energy Materials and Solar Cells*, vol. 27, no. 4, pp. 293–304, 1992.
- [5] A. Hagfeldt, N. Vlachopoulos, and M. Grätzel, "Fast electrochromic switching with nanocrystalline oxide semiconductor films," *Journal of the Electrochemical Society*, vol. 141, no. 7, pp. L82–L84, 1994.
- [6] T. Tatsuma, T. Sotomura, T. Sato, D. A. Buttry, and N. Oyama, "Dimercaptan-polyaniline cathodes for lithium batteries: addition of a polypyrrole derivative for rapid charging," *Journal of the Electrochemical Society*, vol. 142, no. 10, pp. L182–L184, 1995.
- [7] B. O'Regan and M. Grätzel, "A low-cost, high-efficiency solar cell based on dye-sensitized colloidal  $\text{TiO}_2$  films," *Nature*, vol. 353, pp. 737–740, 1991.
- [8] A. J. Bard, M. Stratman, and S. Licht, Eds., *Encyclopedia of Electrochemistry, Semiconductor Electrodes and Photochemistry*, vol. 6, 2002.
- [9] A. Hagfeldt and M. Grätzel, "Light-induced redox reactions in nanocrystalline systems," *Chemical Reviews*, vol. 95, no. 1, pp. 49–68, 1995.
- [10] D. R. Jackson, S. Omanovic, and S. G. Roscoe, "Electrochemical studies of the adsorption behavior of serum proteins on titanium," *Langmuir*, vol. 16, no. 12, pp. 5449–5457, 2000.
- [11] J. E. Davies, "Understanding peri-implant endosseous healing," *Journal of dental education*, vol. 67, no. 8, pp. 932–949, 2003.
- [12] J. Y. Park and J. E. Davies, "Red blood cell and platelet interactions with titanium implant surfaces," *Clinical Oral Implants Research*, vol. 11, no. 6, pp. 530–539, 2000.
- [13] J. Y. Chen, Y. X. Leng, X. B. Tian et al., "Antithrombogenic investigation of surface energy and optical bandgap and hemocompatibility mechanism of  $\text{Ti}(\text{Ta}+5)\text{O}_2$  thin films," *Biomaterials*, vol. 23, no. 12, pp. 2545–2552, 2002.
- [14] H. Nan, Y. Ping, C. Xuan et al., "Blood compatibility of amorphous titanium oxide films synthesized by ion beam enhanced deposition," *Biomaterials*, vol. 19, no. 7–9, pp. 771–776, 1998.
- [15] N. Huang, P. Yang, Y. X. Leng et al., "Hemocompatibility of titanium oxide films," *Biomaterials*, vol. 24, no. 13, pp. 2177–2187, 2003.
- [16] I. Mattisson, C. Gretzer, and E. Ahlberg, "Surface characterization, electrochemical properties and *in vitro* testing of hierarchically structured titanium surfaces," *Materials Research Bulletin*, vol. 48, no. 2, pp. 389–398, 2013.
- [17] I. U. Petersson, J. E. L. Löberg, A. S. Fredriksson, and E. K. Ahlberg, "Semi-conducting properties of titanium dioxide surfaces on titanium implants," *Biomaterials*, vol. 30, no. 27, pp. 4471–4479, 2009.
- [18] Z. Abbas, J. P. Holmberg, A. K. Hellström et al., "Synthesis, characterization and particle size distribution of  $\text{TiO}_2$  colloidal nanoparticles," *Colloids and Surfaces A*, vol. 384, no. 1–3, pp. 254–261, 2011.
- [19] J. Perez Holmberg, Z. Abbas, E. Ahlberg, M. Hassellöv, and J. Bergenholtz, "Nonlinear concentration dependence of the collective diffusion coefficient of  $\text{TiO}_2$  nanoparticle dispersions," *Journal of Physical Chemistry C*, vol. 115, no. 28, pp. 13609–13616, 2011.
- [20] J. Perez Holmberg, A. C. Johnson, J. Bergenholtz, Z. Abbas, and E. Ahlberg, "Near room temperature synthesis of monodisperse  $\text{TiO}_2$  nanoparticles: growth mechanism," *Journal of Physical Chemistry C*, vol. 117, no. 10, pp. 5453–5461, 2013.
- [21] G. Martra, "Lewis acid and base sites at the surface of microcrystalline  $\text{TiO}_2$  anatase: relationships between surface morphology and chemical behaviour," *Applied Catalysis A*, vol. 200, no. 1, pp. 275–285, 2000.
- [22] MeX, Alicona Imaging GmbH, Graz, Austria, 2007.
- [23] J. Löberg, I. Mattisson, S. Hansson, and E. Ahlberg, "Characterisation of titanium dental implants I: critical assessment of surface roughness parameters," *The Open Biomaterials Journal*, vol. 2, pp. 18–35, 2010.
- [24] G. J. Brug, A. L. G. van den Eeden, M. Sluyters-Rehbach, and J. H. Sluyters, "The analysis of electrode impedances complicated by the presence of a constant phase element," *Journal of Electroanalytical Chemistry*, vol. 176, no. 1-2, pp. 275–295, 1984.
- [25] B. Hirschorn, M. E. Orazem, B. Tribollet, V. Vivier, I. Frateur, and M. Musiani, "Determination of effective capacitance and film thickness from constant-phase-element parameters," *Electrochimica Acta*, vol. 55, no. 21, pp. 6218–6227, 2010.
- [26] A. Oyane, H. M. Kim, T. Furuya, T. Kokubo, T. Miyazaki, and T. Nakamura, "Preparation and assessment of revised simulated body fluids," *Journal of Biomedical Materials Research A*, vol. 65, no. 2, pp. 188–195, 2003.
- [27] P. M. Kumar, S. Badrinarayanan, and M. Sastry, "Nanocrystalline  $\text{TiO}_2$  studied by optical, FTIR and X-ray photoelectron spectroscopy: correlation to presence of surface states," *Thin Solid Films*, vol. 358, no. 1, pp. 122–130, 2000.
- [28] S. Hansson, J. Löberg, I. Mattisson, and E. Ahlberg, "Characterisation of titanium dental implants II: local biomechanical model," *The Open Biomaterials Journal*, vol. 2, pp. 36–52, 2010.
- [29] S. Hansson, J. Löberg, I. Mattisson, and E. Ahlberg, "Global biomechanical model for dental implants," *Journal of Biomechanics*, vol. 44, no. 6, pp. 1059–1065, 2011.

- [30] I. Abayev, A. Zaban, V. G. Kytin, A. A. Danilin, G. Garcia-Belmonte, and J. Bisquert, "Properties of the electronic density of states in  $\text{TiO}_2$  nanoparticles surrounded with aqueous electrolyte," *Journal of Solid State Electrochemistry*, vol. 11, no. 5, pp. 647–653, 2007.
- [31] S. Ardizzone, G. Cappelletti, A. Minguzzi, S. Rondinini, and A. Vertova, " $\text{TiO}_2$  nanocrystal particles and electrodes. The combined role of pH and metal substrate," *Journal of Electroanalytical Chemistry*, vol. 621, no. 2, pp. 185–197, 2008.
- [32] T. Berger, T. Lana-Villarreal, D. Monllor-Satoca, and R. Gómez, "An electrochemical study on the nature of trap states in nanocrystalline rutile thin films," *Journal of Physical Chemistry C*, vol. 111, no. 27, pp. 9936–9942, 2007.
- [33] F. Fabregat-Santiago, I. Mora-Seró, G. Garcia-Belmonte, and J. Bisquert, "Cyclic voltammetry studies of nanoporous semiconductors. Capacitive and reactive properties of nanocrystalline  $\text{TiO}_2$  electrodes in aqueous electrolyte," *Journal of Physical Chemistry B*, vol. 107, no. 3, pp. 758–768, 2003.
- [34] T. Lana-Villarreal, Y. Mao, S. S. Wong, and R. Gómez, "Photoelectrochemical behaviour of anatase nanoporous films: effect of the nanoparticle organization," *Nanoscale*, vol. 2, no. 9, pp. 1690–1698, 2010.
- [35] V. G. Kytin, J. Bisquert, I. Abayev, and A. Zaban, "Determination of density of electronic states using the potential dependence of electron density measured at nonzero temperatures," *Physical Review B*, vol. 70, no. 19, Article ID 193304, 4 pages, 2004.
- [36] G. Rothenberger, D. Fitzmaurice, and M. Grätzel, "Spectroscopy of conduction band electrons in transparent metal oxide semiconductor films: optical determination of the flatband potential of colloidal titanium dioxide films," *Journal of Physical Chemistry*, vol. 96, no. 14, pp. 5983–5986, 1992.
- [37] D. B. Bonham and M. E. Orazem, "Mathematical model for the influence of deep-level electronic states on photoelectrochemical impedance spectroscopy. II. Assessment of characterization methods based on Mott-Schottky theory," *Journal of the Electrochemical Society*, vol. 139, no. 1, pp. 127–131, 1992.
- [38] J. Sikora, E. Sikora, and D. D. MacDonald, "Electronic structure of the passive film on tungsten," *Electrochimica Acta*, vol. 45, no. 12, pp. 1875–1883, 2000.
- [39] M. Tomkiewicz, "The potential distribution at the titanium dioxide aqueous electrolyte interface," *Journal of the Electrochemical Society*, vol. 126, no. 9, pp. 1505–1510, 1979.
- [40] X. Chen, A. Nouri, Y. Li, J. Lin, P. D. Hodgson, and C. Wen, "Effect of surface roughness of Ti, Zr, and TiZr on apatite precipitation from simulated body fluid," *Biotechnology and Bioengineering*, vol. 101, no. 2, pp. 378–387, 2008.
- [41] M. Uchida, H. M. Kim, T. Kokubo, S. Fujibayashi, and T. Nakamura, "Effect of water treatment on the apatite-forming ability of NaOH-treated titanium metal," *Journal of Biomedical Materials Research*, vol. 63, no. 5, pp. 522–530, 2002.
- [42] M. Uchida, H. M. Kim, T. Kokubo, S. Fujibayashi, and T. Nakamura, "Structural dependence of apatite formation on titania gels in a simulated body fluid," *Journal of Biomedical Materials Research A*, vol. 64, no. 1, pp. 164–170, 2003.
- [43] T. Ohno, K. Sarukawa, K. Tokieda, and M. Matsumura, "Morphology of a  $\text{TiO}_2$  photocatalyst (Degussa, P-25) consisting of anatase and rutile crystalline phases," *Journal of Catalysis*, vol. 203, no. 1, pp. 82–86, 2001.
- [44] F. Barrere, M. M. E. Snel, C. A. van Blitterswijk, K. de Groot, and P. Layrolle, "Nano-scale study of the nucleation and growth of calcium phosphate coating on titanium implants," *Biomaterials*, vol. 25, no. 14, pp. 2901–2910, 2004.
- [45] E. Leitão, M. A. Barbosa, and K. de Groot, "Influence of substrate material and surface finishing on the morphology of the calcium-phosphate coating," *Journal of Biomedical Materials Research*, vol. 36, no. 1, pp. 85–90, 1997.
- [46] T. Peltola, M. Päätsi, H. Rahiala, I. Kangasniemi, and A. Yli-Urpo, "Calcium phosphate induction by sol-gel-derived titania coatings on titanium substrates *in vitro*," *Journal of Biomedical Materials Research*, vol. 41, no. 3, pp. 504–510, 1998.
- [47] P. Siriphannon, Y. Kameshima, A. Yasumori, K. Okada, and S. Hayashi, "Comparative study of the formation of hydroxyapatite in simulated body fluid under static and flowing systems," *Journal of Biomedical Materials Research*, vol. 60, no. 1, pp. 175–185, 2002.
- [48] L. Jonášová, F. A. Müller, A. Helebrant, J. Strnad, and P. Greil, "Biomimetic apatite formation on chemically treated titanium," *Biomaterials*, vol. 25, no. 7-8, pp. 1187–1194, 2004.
- [49] X. Lu and Y. Leng, "TEM study of calcium phosphate precipitation on bioactive titanium surfaces," *Biomaterials*, vol. 25, no. 10, pp. 1779–1786, 2004.
- [50] A. P. Do Serro, A. C. Fernandes, and V. S. B. de Jesus, "Calcium phosphate deposition on titanium surface in the presence of fibronectin," *Journal of Biomedical Materials Research*, vol. 49, no. 3, pp. 345–352, 2000.
- [51] C. Q. Ning and Y. Zhou, "*In vitro* bioactivity of a biocomposite fabricated from HA and Ti powders by powder metallurgy method," *Biomaterials*, vol. 23, no. 14, pp. 2909–2915, 2002.
- [52] R. L. Reis, A. M. Cunha, M. H. Fernandes, and R. N. Correia, "Treatments to induce the nucleation and growth of apatite-like layers on polymeric surfaces and foams," *Journal of Materials Science: Materials in Medicine*, vol. 8, no. 12, pp. 897–905, 1997.
- [53] Z. Z. Zyman, D. V. Rokhmistrov, and V. I. Glushko, "Structural and compositional features of amorphous calcium phosphate at the early stage of precipitation," *Journal of Materials Science: Materials in Medicine*, vol. 21, no. 1, pp. 123–130, 2010.
- [54] X. Lu and Y. Leng, "Theoretical analysis of calcium phosphate precipitation in simulated body fluid," *Biomaterials*, vol. 26, no. 10, pp. 1097–1108, 2005.
- [55] P. Fratzl and S. G. Himadri, "Nanoscale mechanisms of bone deformation and fracture," in *Handbook of Biomineralization: Biological Aspects and Structure Formation*, E. Bäuerlein, Ed., pp. 397–414, Wiley-VCH, Weinheim, Germany, 2007.
- [56] T. Sohmura, H. Tamasaki, T. Ohara, and J. Takahashi, "Calcium-phosphate surface coating by casting to improve bioactivity of titanium," *Journal of Biomedical Materials Research*, vol. 58, no. 5, pp. 478–485, 2001.
- [57] E. D. Eanes, I. H. Gillessen, and A. S. Posner, "Intermediate states in the precipitation of hydroxyapatite," *Nature*, vol. 208, no. 5008, pp. 365–367, 1965.
- [58] F. A. Müller, L. Müller, D. Caillard, and E. Conforto, "Preferred growth orientation of biomimetic apatite crystals," *Journal of Crystal Growth*, vol. 304, no. 2, pp. 464–471, 2007.
- [59] T. Kokubo and H. Takadama, "How useful is SBF in predicting *in vivo* bone bioactivity?" *Biomaterials*, vol. 27, no. 15, pp. 2907–2915, 2006.
- [60] M. Bohner and J. Lemaitre, "Can bioactivity be tested *in vitro* with SBF solution?" *Biomaterials*, vol. 30, no. 12, pp. 2175–2179, 2009.